People's Democratic Republic of Algeria
Ministry of Higher Education and Scientific Research

Higher Normal School of Technological Education of Skikda



Department of : Physics and Chemistry

THESIS

Submitted in fulfillment of the requirements for the degree of

Doctorate

Domain:	Materials Sciences
Field of study :	Physics
Speciality:	Materials Physics

Presented by :

Ms. KINOUCHA Khalida

Title:

Synthesis and Characterization of Oxyfluoride Glasses Doped with Rare-Earth Ions

---

Publicly defended on: 20/05/2026

before the Jury composed of:

Full name	Academic rank	Establishment	Role
Mr. BOUDJAADAR Djamel	MCA	ENST Skikda	Chair
Mr. BOUBEKRI Hani	MCA	ENST Skikda	Supervisor
Mr. FARTAS Reda	MCA	U8M45	Co-supervisor
Mr. Diaf Madjid	Professor	UBMA	Examiner
Mr. GUERBOUS Lakhdar	MRA	CRNA Algiers	Examiner
Mr. HESSAINIA Amara	MCA	ENST Skikda	Examiner

Academic Year : 2025/2026

Dedication

*First and foremost, I thank **Allah**, the Almighty, for granting me strength, patience, and perseverance to accomplish this work.*

***To myself**,*
for facing challenges, overcoming difficulties, and never giving up.

***To my dear mother**,*
for her unconditional love, prayers, and constant support.

***To my dear father**,*
for his encouragement, guidance, and sacrifices throughout my journey.

***To my husband Djamal Eddine**,*
my true support and life partner, thank you for your patience, encouragement, and unwavering presence.

***To my beloved children**,*
***Ahmed Ouais** and **Nour El-Yasamin**, you are my greatest motivation and the meaning behind all my efforts.*

***To my brothers** and **sisters**,*
*and **to my dear mother-in-law** and **sisters-in-law**,*
thank you for your kindness, support, and care.

And to everyone who supported me with a kind word, a prayer, or sincere encouragement,
I dedicate this work with gratitude and appreciate

Acknowledgements

This doctoral work was carried out at the Laboratory of Physical Chemistry & Biology of Materials, Higher Normal School of Technological Education (ENSET-Skikda), as well as at the Laboratory of Laser Materials Physics and Optical Spectroscopy (LAPLASO), University of Annaba.

I would like to express my deep gratitude to my thesis supervisor, Dr. ***Boubekri Hani****, for his scientific guidance, valuable advice, and continuous availability throughout the completion of this work.*

My sincere thanks also go to my co-supervisor, Dr. ***Fartas Reda****, for his support, helpful suggestions, and constant scientific assistance.*

I also extend my sincere thanks to Professor ***Diaf Madjid****, Director of the Laboratory of Laser Materials Physics and Optical Spectroscopy (LAPLASO), University of Annaba, for his support and the interest he has shown in this work.*

I am deeply honored by the presence of Professor ***Boudjaadar Djamel****, who kindly accepted to chair the defense committee, and I would like to express my sincere gratitude to him. My sincere appreciation also goes to Professors* ***Guerbous Lakhdar*** *for kindly accepting the role of reviewer, and to Professors* ***Hessainia Amara*** *and* ***Diaf Madjid*** *for serving as*

members of the examination committee and for their valuable comments and suggestions.

Finally, I would like to thank all those who contributed, directly or indirectly, to the completion of this work.

Abstract

This thesis investigates the synthesis and spectroscopic characterization of two lead germanate-based oxyfluoride glass systems: a ternary GPF matrix (GeO_2–PbO–PbF_2) co-doped with Tb^{3+}/Yb^{3+} ions and a quaternary GPFC matrix (GeO_2–PbO–PbF_2–CdF_2) doped with Er^{3+} ions. The main objective is to evaluate their potential for photonic applications, particularly frequency conversion and optical amplification.

The samples were synthesized using the melt-quenching method followed by annealing, and their amorphous nature was confirmed by X-ray diffraction (XRD). In the Tb^{3+}/Yb^{3+} co-doped GPF system, luminescence studies reveal an up-conversion mechanism assisted by Yb^{3+} ions under near-infrared excitation. Power dependence measurements confirm a two-photon process involving cooperative energy transfer from Yb^{3+} to Tb^{3+} ions.

In parallel, the Er^{3+}-doped GPFC system was analyzed using the Judd–Ofelt formalism to determine the intensity parameters Ωt. The Ω_2 value (2.76×10^{-20} cm²) indicates significant local asymmetry and covalent character of the bonding environment. With a spectroscopic quality factor of 0.87 and a radiative lifetime of 4.31 ms for the $^4I_{13/2}$ level, this glass exhibits strong potential for optical amplification in the C-band of optical communications (1530–1565 nm).

These results highlight the strong potential of low-phonon-energy oxyfluoride glasses for advanced photonic devices and high-performance light sources.

Keywords: Oxyfluoride glasses, GPF, GPFC, Rare-earth ions, Judd–Ofelt theory, Upconversion luminescence, Optical amplification

Résumé

Cette thèse porte sur la synthèse et la caractérisation spectroscopique de deux systèmes de verres oxyfluorés à base de germanate de plomb : une matrice ternaire GPF (GeO_2–PbO–PbF_2) co-dopée par des ions Tb^{3+}/Yb^{3+} et une matrice quaternaire GPFC (GeO_2–PbO–PbF_2–CdF_2) dopée par des ions Er^{3+}. L'objectif principal est d'évaluer leur potentiel pour des applications photoniques, notamment la conversion de fréquence et l'amplification optique.

Les échantillons ont été élaborés par la méthode de trempe à partir du bain fondu, suivie d'un recuit, et leur nature amorphe a été confirmée par diffraction des rayons X (DRX). Dans le système GPF co-dopé Tb^{3+}/Yb^{3+}, les études de luminescence révèlent un mécanisme de conversion ascendante (up-conversion) assisté par les ions Yb^{3+} sous excitation dans le proche infrarouge. Les mesures de dépendance en puissance confirment un processus à deux photons impliquant un transfert d'énergie coopératif des ions Yb^{3+} vers les ions Tb^{3+}.

Parallèlement, le système GPFC dopé Er^{3+} a été analysé à l'aide du formalisme de Judd–Ofelt afin de déterminer les paramètres d'intensité Ωt. La valeur de Ω_2 (2,76× 10^{-20} cm²) met en évidence une asymétrie locale significative ainsi qu'un caractère covalent marqué de l'environnement de liaison. Avec un facteur de qualité spectroscopique de 0,87 et une durée de vie radiative de 4,31 ms pour le niveau $^4I_{13/2}$, ce verre présente un fort potentiel pour l'amplification optique dans la bande C des communications optiques (1530–1565 nm).

Ces résultats mettent en évidence le fort potentiel des verres oxyfluorés à faible énergie de phonons pour des dispositifs photoniques avancés et des sources lumineuses à haute performance.

Mots-clés : Verre oxyfluoré, GPF, GPFC, terres rares, théorie de Judd-Ofelt, up-conversion, amplification optique.

الملخص

تتناول هذه الأطروحة تحضير ودراسة الخصائص الطيفية لنظامين من الزجاج الأوكسي-فلوريدي المعتمد على جيرمانات الرصاص: مصفوفة ثلاثية (GeO_2–PbO–PbF_2 :GPF) مطعمة بشكل مزدوج بأيونات Tb^{3+}/Yb^{3+}، ومصفوفة رباعية (GeO_2–PbO–PbF_2–CdF_2 :GPFC) مطعمة بأيونات Er^{3+}. ويهدف هذا العمل أساسًا إلى تقييم إمكانيات هذه المواد في التطبيقات الفوتونية، لا سيما تحويل التردد والتضخيم البصري.

تم تحضير العينات باستخدام طريقة التبريد السريع من المصهور (melt-quenching) متبوعة بعملية التلدين، وقد تم تأكيد طبيعتها غير المتبلورة بواسطة حيود الأشعة السينية (XRD). في نظام GPF المطعم بشكل مشترك بـTb^{3+}/Yb^{3+} ، أظهرت دراسات التألق وجود آلية تحويل صاعد (up-conversion) مدعومة بأيونات Yb^{3+} تحت إثارة في نطاق الأشعة تحت الحمراء القريبة. كما أكدت قياسات اعتماد الشدة على القدرة وجود عملية ثنائية الفوتون تتضمن انتقال طاقة تعاوني من أيونات Yb^{3+} إلى أيونات Tb^{3+}.

بالتوازي مع ذلك، تم تحليل نظام GPFC المطعم بأيونات Er^{3+} باستخدام منهجية جَد–أوفلت (Judd–Ofelt) من أجل تحديد معاملات الشدة Ω_t. وتشير قيمة Ω_2 (2.76×10^{-20} سم²) إلى وجود لا تماثل محلي ملحوظ وطابع تساهمي لبيئة الروابط. ومع عامل جودة طيفي يبلغ 0.87 وزمن عمر إشعاعي قدره 4.31 ميلي ثانية للمستوى $^4I_{13/2}$، يُظهر هذا الزجاج إمكانات كبيرة للتضخيم البصري ضمن نطا ق C لمجال الاتصالات (1530–1565 nm)

تُبرز هذه النتائج الإمكانات العالية للزجاج الأوكسي-فلوريدي منخفض طاقة الفونونات في تطوير أجهزة فوتونية متقدمة ومصادر ضوئية عالية الأداء

الكلمات المفتاحية :الزجاج الأوكسي-فلوريدي، GPF، GPFC، العناصر الأرضية النادرة، نظرية Judd-Ofelt، التحويل الصاعد، التضخيم البصري

List of tables

Table	Title	Page
Table I-1	Electronic Configuration of trivalent rare earth ions	8
Table I-2	Determination of the Multiplicity of the Tb^{3+} Ion	16
Table I-**3**	Russell–Saunders (LS) term symbols and degeneracies for the Tb^{3+} ($4f^8$), Yb^{3+} ($4f^{13}$) and Er^{3+}($4f^{11}$) ions	17
Table I-4	Russell–Saunders (LS) spectroscopic terms and spin multiplicities for the Tb^{3+} ion ($4f^8$ configuration)	18
Table I-5	Spectroscopic term symbols and Russell–Saunders multiplets of the $4f^8$ configuration of the Tb^{3+} ion	18
Table I-6	Spectroscopic term symbols and Russell–Saunders multiplets of the $4f^{13}$ configuration of the Yb^{3+} ion	20
Table III-1	Physical Characteristics of the Studied GPF Matrix	61
Table III-2	Molar compositions in % of the GPF matrix	62
Table III-3	below describes the purity of the powders composing the glass	62
Table III-4	Weights of the different chemical components of GPF glass co-doped with Yb_2O_3 (4% mol) and Tb_2O_3 (1% mol)	63
Table III-5	Specific preparation parameters of the Er^{3+}-doped GeO_2–PbO–PbF_2–CdF_2 glass	69
Table III-6	Weights of the different chemical components of GPFC glass co-doped with Er_2O_3 (2% mol.).	69
Table IV-1	Integrated Absorption Cross-Sections σ_{int} and Mean Wavelengths $\bar{\lambda}$ of the Different Transitions of Er^{3+} Ions in the GeO_2–PbO–PbF_2–CdF_2 Matrix.	104
Table IV-2	Squared Reduced Matrix Elements of $U_{(t)}$ (t =2,4, 6) Obtained Between the Ground Level $^4I_{15}/_2$ and the Excited Levels $^{2S'+1}L'_{J'}$	105
Table IV-3	Measured and Calculated Electric Dipole Transition Strengths	107
Table IV-4	Radiative parameters for Er^{3+} ions in GPFC glass: Mean wavelengths (λ), electric (A_{ed}) and magnetic (A_{md}) dipole transition probabilities, branching ratios (β), and radiative lifetimes (τ_{rad})	109

List of figures

Figure	Title	Page
Figure I-1	Periodic table of elements	6
Figure I-2	Energy levels of various trivalent rare earth ions obtained by Dieke	9
Figure I-3	The probability of electron presence varies with distance from the nucleus in the 4f, 5s, 5p, and 6s orbitals of trivalent rare earth ions (TR^{3+})	10
Figure I-4	Analysis of the various interactions influencing the energy level splitting of Ln^{3+} ions	11
Figure I-5	(a) Absorption of a photon with energy hν, equivalent to the energy difference between levels 1 and 2 $h\nu = E_2 - E_1$ (b) Spontaneous emission of a photon with energy $h\nu=E_2-E_1$, emitted in any direction in space (c) Stimulated emission of a photon with energy hν, under the influence of an incident photon with energy hν	24
Figure I-6	a) Resonant energy transfer and energy transfer assisted by: b) emission of phonons c) phonon absorption	26
Figure I-7	Non-radiative resonant transfer (energy migration)	27
Figure I-8	Principle of energy transfer (ET) by cross-relaxation	28
Figure I-9	Mechanism of energy transfer by up conversion a) Sequential absorption process b) Photon addition process by energy transfer (PAET)	29
Figure I-10	The mechanisms of Down-Shifting with (a) one ion and (b) two ions	30
Figure I-11	Different energy transfer processes through Quantum-Cutting	31
Figure I-12	Energy Level Diagram of Yb^{3+} Ion	32
Figure I-13	Absorption coefficient of the germanate glass doped with 0.7 Yb_2O_3/0.7 Tb_2O_3	33

Figure I-14	Deconvolution of the absorption spectrum of NBSAZBYb10 glass	33
Figure I-15	Emission spectra of SAZBYb glasses. Inset shows the deconvolution of the emission spectrum in the spectral region from 990 nm to 1050 nm.	34
Figure I-16	Energy Level Diagram of Tb^{3+} Ion	35
Figure I-17	Room temperature absorption spectra of Tb^{3+} doped CdF_2 single crystal (a) UV–Visible range, (b) near infrared range	36
Figure I-18	Excitation spectrum of Tb^{3+}doped CdF_2 single crystal recorded in the UV–Visible spectral range 250–525 nm	37
Figure I-19	Fluorescence spectrum of Tb^{3+}doped CdF_2 single crystal under excitation wavelength k = 350 nm	38
Figure I-20	Energy Level Diagram of Er^{3+} Ion	39
Figure II-1	Variation of the specific volume of glass and crystal as a function of temperature	46
Figure III-1	the bottles of the powders used	63
Figure III-2	Photograph of a porcelain crucible (high form) without a lid Used in the synthesis step	64
Figure III-3	Photograph of the agate mortar used for grinding, the porcelain crucible, and the chamber furnace in which the crucible is placed	64
Figure III-4	Diagram of the thermal treatment to be followed during glass production GPF	65
Figure III-5	Stages of glass synthesis	65
Figure III-6	(a) Photograph of the Nabertherm brand tubular furnace used for annealing, (b) Glass placed in a porcelain tray inside the tubular furnace heated to 300 °C	66
Figure III-7	Diagram representing the stages of the annealing program	66
Figure III-8	Photograph of the Metkon Forcipol 1V polishing machine	67
Figure III-9	(a) Photograph of the polisher fed by a cloth on which diamond paste is applied, (b) different cloths used	68
Figure III-10	Illustration of X-ray reflection in accordance with Bragg's Law	70

Figure III-11	The geometry of the Bragg-Brentano setup	71
Figure III-12	Photograph of the Panalytical Empyrean X-ray diffractometer (7602 EA, Almelo, The Netherlands)	72
Figure III-13	(a) Principle diagram of the DTA. (b) Deviation from the heating law. (c) DTA curve	73
Figure III-14	A symmetric Setaram analyzer (TAG 24)	74
Figure III-15	Photograph of the SHIMADZU UV-3600 PLUS spectrophotometer	75
Figure III-16	Principle diagram of a double-beam spectrophotometer	76
Figure III-17	Photograph of the Horiba brand spectrofluorometer, model Fluoromax-4, available at the LAPLASO laboratory of the University of Annaba	77
Figure III-18	Descriptive diagram of the Horiba Fluoromax-4 spectrofluorometer	77
Figure IV-1	XRD spectrum of Tb^{3+}–Yb^{3+} co-doped GeO_2–PbO–PbF_2 oxyfluoride glass	83
Figure IV-2	Absorption spectrum of Tb^{3+}–Yb^{3+} co-doped GeO_2–PbO–PbF_2 oxyfluoride glass: (a) visible range, (b) infrared (IR) range.	85
Figure IV-3	Tauc plots of Tb^{3+}–Yb^{3+} co-doped GeO_2–PbO–PbF_2 oxyfluoride glass. In insert, indirect band gap (E_g^{ind})	87
Figure IV-4	Excitation Spectrum of Tb^{3+}–Yb^{3+} co-doped GeO_2–PbO–PbF_2 oxyfluoride glass	88
Figure IV-5	Emission spectra of Tb^{3+}–Yb^{3+} co-doped GeO_2–PbO–PbF_2 oxyfluoride glass under 375 nm and 976 nm excitation wavelengths.	90
Figure IV-6	Diode laser pump power evolution of the emission spectrum of Tb^{3+}–Yb^{3+} co-doped GeO_2–PbO–PbF_2 oxyfluoride glass over the range 300-600 mW ($\lambda_{exc} = 940nm$).	91
Figure IV-7	Log–log plot of emission intensities as a function of incident power Tb^{3+}–Yb^{3+} co-doped GeO_2–PbO–PbF_2 oxyfluoride glass.	92
Figure IV-8	Partial energy level diagram of Tb^{3+} illustrating the Yb^{3+}→ Tb^{3+}energy transfer mechanism under 940 nm excitation.	93

Figure IV-9	Time-resolved luminescence of Tb^{3+}–Yb^{3+} co-doped GeO_2–PbO–PbF_2 oxyfluoride glass under 976 nm excitation.(a) Three-dimensional time-resolved emission spectrum.(b) Decay curves recorded for the $^5D_4 \rightarrow {}^7F_6$ (490 nm), $^5D_4 \rightarrow {}^7F_5$ (545 nm), and $^5D_4 \rightarrow {}^7F_4$ (621 nm) transitions of Tb^{3+}.	97
Figure IV-10	CIE chromaticity diagram of Tb^{3+}–Yb^{3+} co-doped GeO_2–PbO–PbF_2 oxyfluoride glass under 375 nm and 976 nm excitation wavelengths	98
Figure IV-11	Room-Temperature Absorption Spectrum of GeO_2–PbO–PbF_2–CdF_2 : Er^{3+} Glass in the NIR Region	100
Figure IV-12	Room-Temperature Absorption Spectrum of GeO_2–PbO–PbF_2–CdF_2 : Er^{3+} (2 mol%) oxyfluoride Glasses in the UV–Visible Region	101

Table of Contents

Table of Contents

General introduction 1

Bibliographic references 4

Chapter I: Spectroscopy of rare earth ions 6

Introduction 6

I-1. Generalities on rare earths 7

I-2. Electronic structure 8

I-3. Optical properties of rare earth ions 9

I-4. Hamiltonian of the rare earth ion in the host matrix 11

I-5. Crystal field theory 13

I-6. Lifting of degeneracy and Stark sublevels 14

I-7. Number of microstates of the $4f^{13}$ and $4f^{8}$ configurations 15

I-8. Degeneracy of spectroscopic terms ^{2S+1}L 16

I-8-1. Degeneracy of spectroscopic terms Tb^{3+} 16

I-8-2. Degeneracy of spectroscopic terms Yb^{3+} 17

I-8-3. Degeneracy of spectroscopic terms Er^{3+} 17

I-9. Degeneracy of $^{2S+1}L_J$ multiplets 18

I-10. Selection rules for optical transitions 20

I-11. Interaction of rare earth ions with electromagnetic radiation 21

I-11-1. Radiative transitions 21

a) Absorption 21

b) Emission 22

I-11-2. Non-radiative transitions 24

I-12. Energy transfer between rare-earth ions 25

I-12-1. Resonant or phonon-assisted energy transfer 25

I-12-2. Direct transfer 26

I-12-3. Energy migration 26

I-12-4. Cross relaxation 27

I-13. Energy transfer by up-conversion (APTE) 28

I-14. Energy transfer by down-conversion 29

a) Down-shifting 29

b) Quantum cutting 30

I-15. Spectroscopic characteristics of the studied RE^{3+} ions 31

I-15-1. The ion ytterbium (Yb^{3+}) 31

a) Characteristics of the trivalent ytterbium ion (Yb^{3+}) 31

I-15-2. The ion terbium (Tb^{3+}) 34

a) Characteristics of the trivalent terbium ion (Tb^{3+}) 34

I-15-3. The ion erbium (Er^{3+}) 38

Bibliographic references 40

Chapter II: Glasses 43

Introduction 43

II-1. History 43

II-2. Definition of a glass 44

II-3. The glass transition 45

II-4. The major families of glasses 47

II-4-1. Oxide glasses 47

II-4-2. Metallic glasses 47

II-4-3. Halide glasses 48
Fluorinated glasses 48
Chloride glasses 49
II-4-4. Chalcogenide glasses 50
II-4-5. Oxyfluoride glasses 51
Importance of oxyfluoride glasses for up-conversion applications 52
II-5. Properties of glasses 52
Optical properties 52
a) Transmission of light 54
b) Refractive index and dispersion 55
c) Refractive index of a composite glass 55
Thermal properties 56
a) Specific heat (C_p) 56
b) Thermal conductivity (K) 56
c) Coefficient of thermal expansion (α) 56
Bibliographic references 57
Chapter III: Glass synthesis and characterization techniques 60
Introduction 60
III-1. Synthesis of glasses 60
III-1-1. Composition of the glass to be developed 60
a) Physical properties of the studied glass 61
b) Molar composition of the developed glass 61
III-1-2. Synthesis process 62
a) Weighing of different constituents according to the concentration of the dopants 62
b) Description of the crucible 63
c) Grinding and mixing of powders 64
d) Furnace heating program and quenching of the molten bath 64
e) Glass solidification by annealing 65
f) Polishing the glass to obtain two parallel surfaces 66

III-2. Characterization techniques 69

III-2-1. Structural characterization by X-ray diffraction 69

a) Overview of X-ray diffraction (XRD) 69

b) Bragg-Brentano geometry 70

c) Description of the experimental setup 72

III-2-2. Thermal characterization by differential thermal analysis (DTA) 72

a) Principle of operation 72

b) Description of the equipment 73

III-2-3. Recording of absorption and emission spectra 75

III-2-3-1. Recording of absorption spectra 75

a) Absorption spectra at room temperature 75

b) Description of the SHIMADZU UV-3600 PLUS spectrophotometer 75

III-2-3-2. Recording of emission spectra 76

a) Emission spectra at room temperature 76

b) Description of the Horiba Fluoromax-4 spectrofluorometer 76

c) Optical arrangement 77

III-2-3-3. Photoluminescence measurements 78

III-2-3-4. Time-resolved photoluminescence measurements 79

Bibliographic references 80

Chapter IV: Results and interpretations 81

Introduction 81

IV-1. Physical properties of Tb^{3+}/Yb^{3+} co-doped GPF oxyfluoride glass 81

IV-2. Structural characterization of Tb^{3+}/Yb^{3+} co-doped GPF oxyfluoride glass 83

IV-3. Optical absorption spectroscopy of Tb^{3+}/Yb^{3+} co-doped GPF oxyfluoride glass 84

IV-4. Optical energy gap of Tb^{3+}/Yb^{3+} co-doped GeO_2–PbO–PbF_2 oxyfluoride glass 86

IV-5. Excitation spectroscopy of Tb^{3+}/Yb^{3+} co-doped GeO_2–PbO–PbF_2 oxyfluoride glass…..88

IV-6. Up-conversion emission of Tb^{3+}/Yb^{3+} co-doped GeO_2–PbO–PbF_2 oxyfluoride glass….89

IV-6-1. Up-conversion emission spectra under NIR excitation 89

IV-6-2. Power dependence of the up-conversion emission 91

IV-6-3. Energy transfer mechanism $Yb^{3+} \rightarrow Tb^{3+}$ 93

IV-6-4. Time-resolved luminescence and decay analysis 95

IV-7. Chromaticity analysis and multicolor emission 97

IV-8. Judd–Ofelt analysis of Er^{3+} in GeO_2–PbO–PbF_2–CdF_2 oxyfluoride glass 98

IV-8-1. Relationship between radiative transition probabilities and emission cross-section

……..……..…..99

IV-8-2. Absorption spectroscopic characterization 99

IV-8-3. Absorption spectrum in the near-infrared region (700–1700 nm) 99

IV-8-4. Absorption spectrum in the visible region (400–700 nm) 100

IV-8-5. Absorption spectrum in the ultraviolet region (200–400 nm) 101

IV-9. Influence of the GeO_2–PbO–PbF_2–CdF_2:Er^{3+} matrix and nature of the transitions 101

IV-10. Selection and properties of the oxyfluoride matrix GeO_2–PbO–PbF_2–CdF_2:Er^{3+} 102

IV-11. Formalism of the Judd–Ofelt theory 102

IV-12. Exploitation of the Judd–Ofelt analysis 103

a) Mean wavelength and absorption cross-section..... 103

b) Transition strengths 104

c) Calculated forced electric dipole transition strengths 105

d) Calculated magnetic dipole transition strengths 105

e) Measured electric and magnetic dipole transition strengths 108

f) Spontaneous transition probability 108

g) Radiative lifetime of an emitting level and branching ratio 108

Bibliographic references 113
General conclusion 116

General Introduction

General Introduction

Oxyfluoride glasses have attracted growing interest in the field of optical materials over the past decades due to their unique ability to combine the advantageous properties of oxide and fluoride glasses. These materials exhibit high optical transparency over wide spectral ranges, relatively low phonon energy (typically in the range of 500–600 cm^{-1}), good chemical durability, and excellent thermal stability. Such characteristics make oxyfluoride glasses particularly suitable for advanced photonic applications including solid-state lasers, optical amplifiers, frequency conversion devices, integrated photonic components, and up-conversion luminescence materials [1–7]. Compared to conventional silicate glasses, which exhibit higher phonon energies (900 – 1100 cm^{-1}), the reduced phonon energy of oxyfluoride glasses significantly limits non-radiative multiphonon relaxation processes, thereby enhancing the luminescence efficiency and quantum yield of rare-earth-doped systems [2,3].

Rare earth ions, especially trivalent lanthanide ions (Ln^{3+}), play a central role as active optical centers in modern photonic materials due to their remarkable spectroscopic properties. These properties originate from electronic transitions within the partially filled 4f shell, which is effectively shielded from the surrounding host matrix by the filled $5s^2$ and $5p^6$ orbitals. As a result, rare earth ions exhibit sharp emission lines, high color purity, and stable radiative transitions that are weakly influenced by the local environment [8–10]. Their emission wavelengths span a broad spectral range extending from the ultraviolet to the infrared regions, enabling their use in numerous applications such as up-conversion luminescence, temperature sensing, photonic amplification, and optical imaging. Nevertheless, the optical performance of rare earth ions remains strongly dependent on the nature of the host matrix, making the choice of glass composition a key parameter for optimizing luminescence behavior [8,10].

Among rare-earth co-doped systems, Tb^{3+}/Yb^{3+} combinations have attracted considerable attention owing to their up-conversion luminescence under near-infrared excitation around 980 nm. In such systems, Yb^{3+} ions act as efficient sensitizers due to their simple electronic structure and strong absorption corresponding to the $^2F_{7/2} \rightarrow {}^2F_{5/2}$ transition, while Tb^{3+} ions serve as activators emitting visible radiation. The up-conversion process is generally governed by cooperative energy transfer mechanisms involving excited Yb^{3+} ions, which preferentially populate the lower-energy $^5D_4$ level of Tb^{3+}. As a result, the characteristic emission is dominated by green luminescence

arising from the $^5D_4 \rightarrow {}^7F_J$ transitions, whereas emissions originating from the higher-energy $^5D_3$ level are often weak or absent under near-infrared excitation conditions, depending on the host matrix and energy transfer dynamics [11–15].

Oxyfluoride glasses are particularly favorable hosts for Tb^{3+}/Yb^{3+} up-conversion systems because their low phonon energy significantly suppresses non-radiative relaxation pathways, thereby improving energy transfer efficiency and emission intensity [3-5]. In this context, the GeO_2–PbO–PbF_2 glass system represents an attractive oxyfluoride host matrix. Germanium dioxide (GeO_2) acts as a network former providing good glass-forming ability, high refractive index, and wide optical transparency, while the incorporation of PbO and PbF_2 contributes to lowering the phonon energy and enhancing the solubility of rare earth ions. Previous studies have shown that this glass composition offers a suitable compromise between structural stability, thermal properties, and optical performance, making it promising for rare-earth-doped photonic applications [6, 7, 14].

The present doctoral work is devoted to a systematic investigation of the structural, thermal, and optical properties of a 50GeO_2–30PbO–20PbF_2 oxyfluoride glass doped with Tb^{3+} and Yb^{3+} ions, with particular emphasis on understanding up-conversion luminescence mechanisms and energy transfer processes between the rare earth ions. Structural characterization techniques are employed to confirm the amorphous nature of the prepared glasses, while thermal analysis is used to evaluate their stability and resistance to crystallization [4, 6]. Optical absorption, photoluminescence, and up-conversion measurements are performed to analyze the spectroscopic behavior of the doped system [11–15]. In addition, the Judd–Ofelt theoretical approach is applied to the absorption spectra of an Er^{3+}-doped 60GeO_2–20PbO–9PbF_2–9CdF_2 oxyfluoride glass in order to determine the radiative properties of Er^{3+} ions and to gain insight into their local environment within the glass matrix [16–18].

This thesis is organized as follows.

Chapter 1 is devoted to the spectroscopy of rare earth ions and presents the fundamental theoretical background necessary for understanding their optical behavior, including electronic configurations, energy level structures, and selection rules governing optical transitions.

Chapter 2 focuses on glass materials as host matrices for rare earth ions, highlighting the structure and properties of different glass families with particular emphasis on oxyfluoride glasses and germanate-based systems.

Chapter 3 describes the synthesis procedures and experimental techniques employed in this work, including glass preparation, structural and thermal characterization, and optical spectroscopy methods.

Chapter 4 presents and discusses the experimental results, correlating structural, thermal, and optical properties with up-conversion luminescence behavior in Tb^{3+}/Yb^{3+}-doped glasses and Judd–Ofelt analysis in Er^{3+}-doped oxyfluoride systems, in order to evaluate the potential of the studied materials for photonic application

Bibliographic references

[1] M. Poulain, “Fluoride and oxyfluoride glasses,” *Journal of Non-Crystalline Solids*, 140 (1992) 1–10.

[2] S. Tanabe, “Optical properties of heavy-metal oxide and oxyfluoride glasses,” *Journal of the American Ceramic Society*, 84 (2001) 222–238.

[3] J. Qiu, “Rare-earth-doped oxyfluoride glasses and glass-ceramics,” *Journal of Non-Crystalline Solids*, 354 (2008) 223–230.

[4] M. C. Gonçalves et al., “Rare-earth-doped transparent glass ceramics,” *Comptes Rendus Chimie*, 5 (2002) 845–854.

[5] Z. Li et al., Multicolor upconversion in oxyfluoride glass-ceramics, *Scientific Reports*, 7 (2017) 6518.

[6] M. E. Cruz et al., “Rare-earth doped transparent oxyfluoride glass-ceramics: processing is the key,” *Optical Materials Express*, 12 (2022) 3493–3516.

[7] Z. Li et al., Tailoring optical properties of rare-earth doped oxyfluoride glass-ceramics, *Advanced Optical Materials*, 11 (2023) 2202475.

[8] B. Henderson, G. F. Imbusch, *Optical Spectroscopy of Inorganic Solids*, Oxford University Press, 1989.

[9] A. J. Kenyon, “Recent developments in rare-earth doped materials for photonics,” *Progress in Quantum Electronics*, 26 (2002) 225–284.

[10] J. Hehlen, “Spectroscopy and dynamics of rare-earth ions in glasses,” *Journal of Luminescence*, 119–120 (2006) 387–397.

[11] F. Auzel, “Upconversion and anti-Stokes processes with f and d ions in solids,” *Chemical Reviews*, 104 (2004) 139–173.

[12] T. Yamashita, Y. Ohishi, Cooperative energy transfer between Tb^{3+} and Yb^{3+} ions co-doped in glass, *Journal of Non-Crystalline Solids*, 354 (2008) 1883–1890.

[13] Y. Arai et al., “Upconversion properties of Tb^{3+}–Yb^{3+} codoped glasses,” *Journal of Applied Physics,* 105 (2009) 083105.

[14] V. Scarnéra et al., Green upconversion in Yb^{3+}–Tb^{3+} doped fluoro-germanate glasses, *Optical Materials*, 33 (2010) 159–163.

[15] Q. Duan et al., Upconversion emission of Tb^{3+}–Yb^{3+} codoped systems, *Journal of the Optical Society of America B*, 30 (2013) 456–462.

[16] B. R. Judd, “Optical absorption intensities of rare-earth ions,” *Physical Review*, 127 (1962) 750–761.

[17] G. S. Ofelt, “Intensities of crystal spectra of rare-earth ions,” *Journal of Chemical Physics*, 37 (1962) 511–520.

[18] A. Ćirić et al, Self-referenced Judd–Ofelt analysis of rare-earth doped materials, *Scientific Reports*, 12 (2022) 563.

Chapter I :Rare Earth Ions Spectroscopy

Introduction

The periodic table contains elements with diverse physical and chemical characteristics. Among these are the rare-earth elements, also known as the lanthanides, which range from lanthanum (Z = 57) to lutetium (Z = 71). The group is often extended to include scandium and yttrium due to their similar chemical behavior **[1]**.

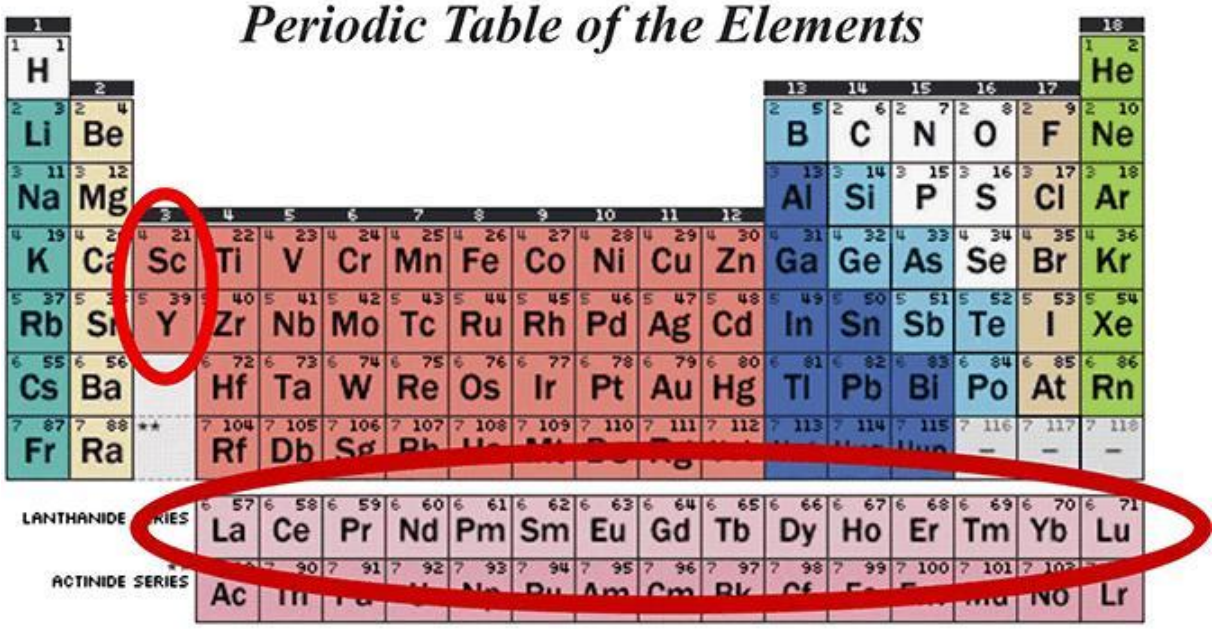


Figure I-1: Periodic table of elements [2]

Rare-earth ions are widely recognized for their magnetic properties, but most notably for their exceptional luminescent behavior.

Electronic transitions within their 4f orbitals give rise to narrow absorption and emission bands, spanning a broad spectral range from the infrared to the ultraviolet [3, 4]. This rich optical behavior makes them highly valuable in numerous applications such as television phosphors, scientific scintillators, and laser materials [5]. These elements generally occur in the trivalent state (Ln^{3+}), characterized by an electronic configuration of [Xe] $4f^N$. The 4f orbitals are obscured by the external 5s and 5p orbitals, leading to negligible interaction with the surrounding host matrix and providing significant spectral stability, even in amorphous environments such as glass [3, 4].

To fully harness their potential, it is essential to understand their electronic structure, the mechanisms of absorption and emission, and the various factors that influence their optical behavior, especially in doped glass matrices.

Accordingly, this chapter provides a detailed study of the fundamental spectroscopic properties of rare-earth ions, as a foundation for exploring their role in doped oxyfluoride glasses. In this context, rare-earth-doped oxyfluoride glasses constitute an ideal platform for investigating energy transfer mechanisms, up-conversion processes, and structure–property relationships.

I-1. Generalities on rare earths elements

The discovery of rare earth elements took place in 1794 by J. Gadolin in Ytterby, Sweden, where they were identified in the form of oxides containing a multitude of elements he called Yttria. The process of separating these elements, which have similar chemical properties, was difficult and took over a century for their complete isolation. For example, Neodymium was long associated with Praseodymium in a compound called didymium (from the Greek "didymes," meaning twins), where the existence of several elements was presumed despite many failed separation attempts. The family of rare earth elements comprises lanthanide elements, with atomic numbers spanning from Z=57 (Lanthanum, La) to Z=71 [6] (Lutetium, Lu), elements associated with Scandium (Sc, Z=21) and Yttrium (Y, Z=39), which have similar chemical properties. Trivalent lanthanide ions, which have an incomplete 4f shell (ranging from Ce^{3+} with an electronic structure of [Xe] $4f^1$ to Yb^{3+} with an electronic structure of [Xe] $4f^{13}$), have specific optical characteristics, which is why they are commonly used as optically active ions in luminescent materials. This series of compounds is now used in various fields, including catalysis, metallurgy, magnetism, and of course optics. In this particular application, rare earth elements are used for their electronic characteristics, which allow for powerful emissions ranging from ultraviolet (UV) to mid-infrared (IR). These rare earth elements are very reactive to oxygen and easily oxidize when exposed to air. They are typically handled with protective gloves, under a controlled atmosphere of very purified and continuously renewed argon. In their metallic form, these elements readily combine with other transition elements to form intermetallic compounds widely analyzed for their magnetic characteristics. In their ionic form, they are derived from

solid ionic materials such as rare earth fluorides and oxides. They are generally found in their trivalent ionic form, which corresponds to the condensed electronic configuration [Xe] $4f^N$, with N ranging from 1 to 14. It is important to mention, however, that some rare earth ions are found in divalent (Eu^{2+}, Sm^{2+}, Yb^{2+}, Dy^{2+}, and Tm^{2+}) or tetravalent (Ce^{4+}) forms. Rare earth elements are characterized by a partially filled 4f subshell. The electrons in the 4f subshell predominantly govern the optical and magnetic characteristics of these elements, with all optical transitions taking place between the energy levels of the 4f configuration.

I-2. Electronic structure

The electronic configuration of rare-earth (RE^{3+}) ions is based on that of Xenon, whose atomic number is Z = 54: [Xe] = $1s^2\ 2s^2\ 2p^6\ 3s^2\ 3p^6\ 3d^{10}\ 4s^2\ 4p^6\ 4d^{10}\ 5s^2\ 5p^6$. To this configuration, the 4f shell must be added, where one to fourteen electrons are arranged, ranging from Ce^{3+} to Lu^{3+} (Table I-1). In a trivalent state, the electrons from the 5d and 6s subshells of the neutral atom are removed. Thus, the basic electronic configuration is $4f^N$, (N taking values from 1 for Cerium to 14 for Lutetium).

Table I-1: Electronic Configuration of trivalent rare earth ions

Atomic Number	Element (Symbol)	Electronic Configuration (Atoms)	Electronic Configuration of Trivalent Ions (TR^{3+})	Ground State of Trivalent Ions (TR^{3+})
57	Lanthanum (La)	$[X_e]4f^05d^16s^2$	$[X_e]4f^0$	$^1S_0$
58	Cerium (Ce)	$[X_e]4f^25d^06s^2$	$[X_e]4f^1$	$^2F_{5/2}$
59	Praseodymium (Pr)	$[X_e]4f^35d^06s^2$	$[X_e]4f^2$	$^3H_4$
60	Neodymium (Nd)	$[X_e]4f^45d^06s^2$	$[X_e]4f^3$	$^4I_{9/2}$
61	Promethium (Pm)	$[X_e]4f^55d^06s^2$	$[X_e]4f^4$	$^5I_4$
62	Samarium (Sm)	$[X_e]4f^65d^06s^2$	$[X_e]4f^5$	$^6H_{5/2}$
63	Europium (Eu)	$[X_e]4f^75d^06s^2$	$[X_e]4f^6$	$^7F_0$
64	Gadolinium (Gd)	$[X_e]4f^75d^16s^2$	$[X_e]4f^7$	$^8S_{7/2}$
65	**Terbium(Tb)**	$\boldsymbol{[X_e]4f^95d^06s^2}$	$\boldsymbol{[X_e]4f^8}$	$\boldsymbol{^7F_6}$
66	Dysprosium (Dy)	$[X_e]4f^{10}5d^06s^2$	$[X_e]4f^9$	$^6H_{15/2}$
67	Holmium (Ho)	$[X_e]4f^{11}5d^06s^2$	$[X_e]4f^{10}$	$^5I_8$
68	**Erbium (Er)**	$\boldsymbol{[X_e]4f^{12}5d^06s^2}$	$\boldsymbol{[X_e]4f^{11}}$	$\boldsymbol{^4I_{15/2}}$

69	Thulium (Tm)	$[X_e]4f^{13}5d^06s^2$	$[X_e]4f^{12}$	$^3H_6$
70	**Ytterbium (Yb)**	$[X_e]4f^{14}5d^06s^2$	$[X_e]4f^{13}$	$^2F_{7/2}$
71	Lutetium (Lu)	$[X_e]4f^{14}5d^16s^2$	$[X_e]4f^{14}$	$^1S_0$

Diecke and his team [7] identified a large number of energy levels for the $4f^n$ configuration of TR^{3+} ions from Cerium to Ytterbium in the LaCl3 matrix. This work is documented in (Figure I-2)

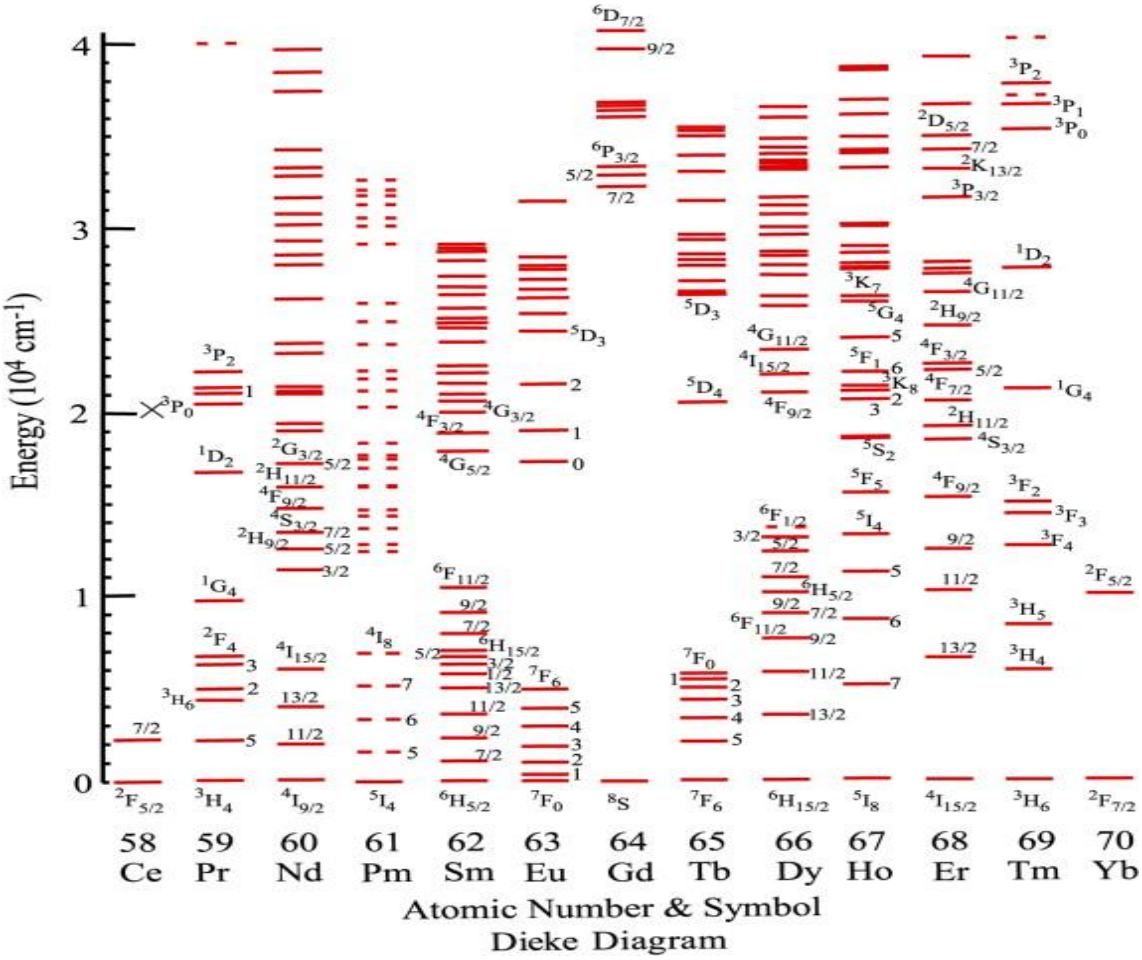


Figure I-2: Energy levels of various trivalent rare earth ions obtained by Dieke [8]

I-3. Optical properties of rare earth ions

The electrons belonging to the incomplete inner $4f^N$ shell (optically active electrons) are thus shielded from the crystal environment by the completely filled inner shells $5s^2$ $5p^6$ (figure I-3). Consequently, the electrons residing in the partially filled $4f^N$ shell play a crucial role in determining the optical and magnetic characteristics of rare earth ions.

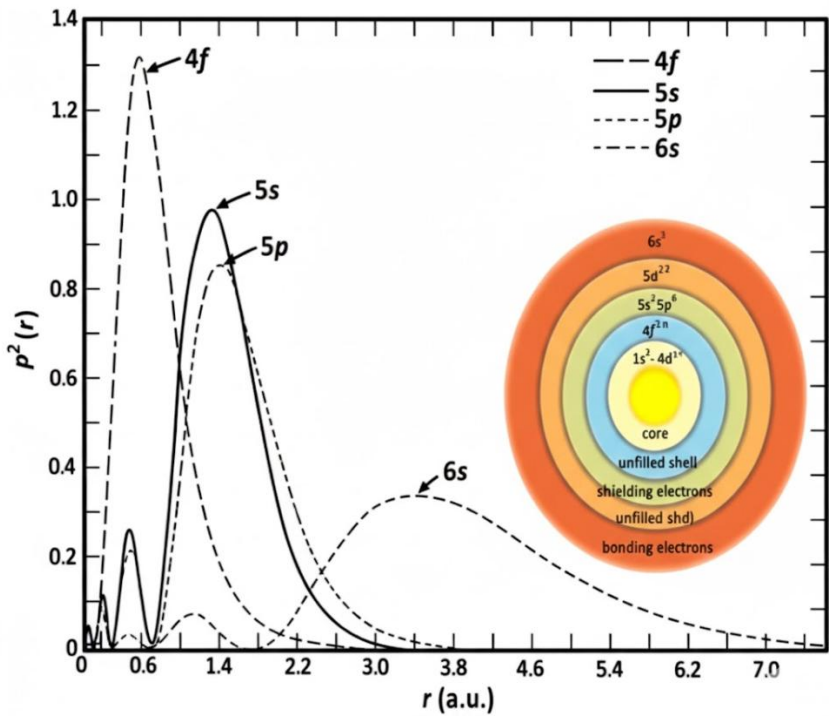


Figure I-3: The probability of electron presence varies with distance from the nucleus in the 4f, 5s, 5p, and 6s orbitals of trivalent rare earth ions (TR^{3+}) [1]

The optical spectra of rare earth ions in solids corresponds to electronic transitions within the 4f shell. They are characterized by fine lines due to the shielding effect of the completely filled outer shells $5s^2$ $5p^6$ on the crystal field to which the 4f electrons are subjected. The energy levels of the $4f^n$ configuration of Lanthanide ions exhibit a degeneracy characterized by $\frac{14!}{(14-N)!N!}$ microstates.

This degeneracy is partially or completely lifted under the effect of various perturbations.

- Coulomb repulsion results in the splitting of energy levels, yielding the terms 2S+1L of the free ion, each of which is degenerate (2S+1)(2L+1) times. The energy gap between two subsequent terms is approximately 10^4 cm^{-1}.
- Spin-orbit coupling splits these terms into multiplets $^{2S+1}L_J$, with the order of magnitude of the splitting being around 10^3 cm^{-1}.
- The influence of the crystal field partially or entirely removes the degeneracy of the different multiplets, resulting in the formation of the Stark sublevels Γi. The division of the Stark sublevels associated with a specific multiplets is approximately 10^2 cm^{-1}. The gradual separation of energy levels of the rare earth

ion, originating from the $4f^N$ configuration due to these disturbances, together with the associated energy values, is illustrated in Figure (I-4).

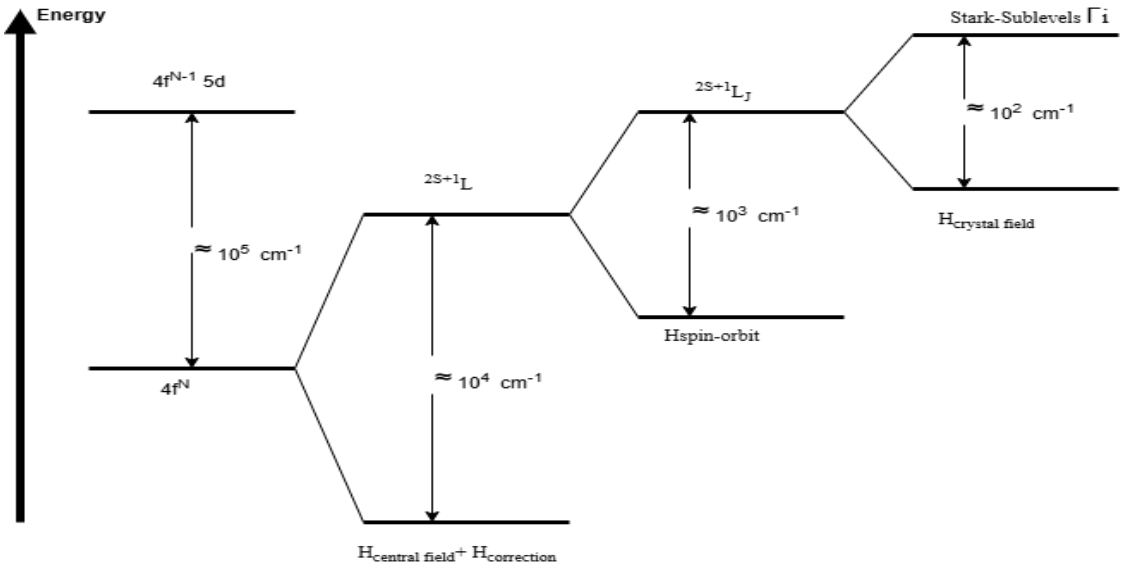


Figure I-4: Analysis of the various interactions influencing the energy level splitting of Ln^{3+} ions [9]

I-4. Hamiltonian of the rare earth ion in the host matrix

In quantum mechanics, the energy levels of an ion are, in fact, the eigenstates of a microscopic system. They can be obtained by solving the Schrödinger equation:

$$H\psi = E\psi \qquad \text{(Eq. I-1)}$$

The Hamiltonian H of the rare earth ion within the matrix, whether crystalline or amorphous, comprises the Hamiltonian of the free ion and the interaction Hamiltonian between the electrons in the active 4f shell and the electrostatic field generated by the crystal environment:

$$H = H_{\text{free ion}} + H_{\text{crystal field}} \qquad \text{(Eq. I-2)}$$

The Hamiltonian of the free ion itself consists of several terms.

$$H_{\text{free ion}} = \sum_{i=1}^{N}\left[\frac{P_i^2}{2m} - \frac{-Ze^2}{4\pi\varepsilon_0 r_i} + \xi(r_i)\vec{l}_i.\vec{S_i}\right] + \sum_{\substack{i,j=1 \\ i>j}}^{N}\frac{e^2}{4\pi\varepsilon_0 r_{ij}} \qquad \text{(Eq. I-3)}$$

- $\frac{P_i^2}{2m}$: The kinetic energy operator for the *i*-th electron (mass *m*, charge –*e*).

- $\frac{-Ze^2}{4\pi\varepsilon_0 r_i}$: The operator describing the Coulomb attraction between the *i*-th electron and the nucleus (charge *Ze*).
- $\xi(r_i)\vec{l}_i.\vec{s_i}$: The spin-orbit coupling Hamiltonian for the *i*-th electron.
- $\frac{e^2}{4\pi\varepsilon_0 r_{ij}}$ The Coulomb repulsion operator between the *i*-th and *j*-th electrons.

The summations are performed over the N electrons in the incomplete 4f shell.
This Hamiltonian does not incorporate any additional interactions within the ion, such as intrinsic magnetic interactions among the magnetic moments of electrons (spin interactions), as well as the interactions between the orbital and intrinsic magnetic moments of electrons and the nuclear magnetic moment, or hyperfine structure, since these interactions are significantly weaker than electrostatic interactions and spin-orbit coupling.

In a general way, the Hamiltonian of a free ion can be written as:

$$H_{free\ ion} = H_{central\ field} + H_{correction} + H_{spin\text{-}orbit} \qquad \text{(Eq. I-4)}$$

The initial component of the Hamiltonian encompasses the kinetic and potential contributions of each 4f electron within the framework of the "central field approximation". We then acknowledge that each electron experiences an average central potential produced by the nucleus and all other electrons. The Hamiltonian is expressed as:

$$H_{central\ field} = \sum_{i=1}^{N}\left[-\frac{\hbar^2}{2m}\Delta_i + V(r_i)\right] \qquad \text{(Eq. I-5)}$$

The second term corresponds to a corrective term in the Hamiltonian, which accounts for the difference between the average central potential and the actual electron nucleus Coulomb interaction, as well as for the electron–electron Coulomb repulsion.

This correction arises from the use of the central-field approximation and aims to represent the Coulomb effects as accurately as possible:

$$H_{correction} = \sum_{i=1}^{N}\left[-\frac{Ze^2}{4\pi\varepsilon_0 r_i} - V(r_i)\right] + \sum_{j>i}\frac{1}{4\pi\varepsilon_0}\frac{e^2}{r_{ij}} \qquad \text{(Eq. I- 6)}$$

The last term of the Hamiltonian accounts for the spin-orbit coupling:

$$H_{spin-orbit} = \sum_{i=1}^{N} \xi(r_i)\vec{l}_i.\overrightarrow{S_i} \qquad \text{(Eq. I-7)}$$

Where $\xi(r_i) = \frac{\hbar^2}{2m^2c^2r_i}\frac{\partial V(r_i)}{\partial r_i}$

Therefore:

$$\mathrm{H_{free\ ion}} = \sum_{i=1}^{N}\left(-\frac{\hbar^2}{2m}\Delta_i - \frac{1}{4\pi\varepsilon_0}\frac{Ze^2}{r_i} + \sum_{j>i}\frac{1}{4\pi\varepsilon_0}\frac{e^2}{r_{ij}}\right) + \sum_{i=1}^{N}\xi(r_i)\vec{l}_i.\overrightarrow{S_i} \qquad \text{(Eq. I-8)}$$

I-5. Crystal field theory

When a free rare-earth ion is incorporated into a glassy or crystalline matrix, such that interactions between dopant ions can be neglected, it becomes necessary to consider the interaction between the electric field created by the surrounding ligands and the rare-earth ion. This additional interaction is referred to as the crystal field. The primary effect of the crystal field is the breaking of the spherical symmetry of the free ion, which is replaced by the point symmetry of the crystallographic site occupied by the dopant ion.

This reduction in symmetry leads to a lifting of the degeneracy of the $^{2S+1}L_J$ multiplets. Consequently, an energy level characterized by a total angular momentum J splits into (2J+1) Stark sublevels when J is an integer, and into (J+1/2) Kramers doublets when J is a half-integer. The exact number of expected sublevels depends both on the nature of the rare-earth ion and on the local point symmetry [10].

However, the $4f^N$ electronic shell remains strongly shielded from the external environment by the $5s^2$ and $5p^6$ shells. This shielding effect significantly reduces the influence of the crystal field, allowing it to be treated as a perturbation applied to the free ion. The Hamiltonian describing a RE^{3+} ion in a matrix can therefore be expressed as:

$$\mathrm{H_{ion\ dopant}} = \mathrm{H_{ion\ libre}} + \mathrm{H_{crystal\ field}} \qquad \text{(Eq. I-9)}$$

The Hamiltonian of the crystal field is:

$$H_{crystal\ field} = \frac{1}{4\pi\varepsilon_0}\sum_i \sum_j \frac{z_j.e^2}{\|\vec{R}_j - \vec{r}_i\|} \quad \text{(Eq. I-10)}$$

where r_i is the position of the i-th electron.

R_j is the position vector of the j-th ligand relative to the center of the site occupied by the doped ions. The ligand carries an effective electric charge $q_j = z_j e$, which may be positive or negative. The summations are performed over all ligands and all electrons.

Since the free-ion Hamiltonian is solved assuming spherical symmetry, the crystal field Hamiltonian can be expanded in terms of spherical harmonics, or equivalently, in operators that transform like spherical harmonics [6]. The crystal field Hamiltonian then becomes:

$$H_{crystal\ field} = \sum_{k,q,i} B_q^k \,.\, (C_q^k)_i \quad \text{(Eq. I-11)}$$

With $$(C_q^k)_i = \sqrt{\frac{4}{2k+1}}\,.\, Y_q^k(\theta_i, \varphi_i) \quad \text{(Eq. I-12)}$$

$$B_q^k = A_q^k \langle r^k \rangle \quad \text{(Eq. I-13)}$$

The coefficientsB_q^k, known as crystal field parameters, are semi-empirical quantities that can be expressed in terms of the radial integrals $\langle r^k \rangle$ of the 4f electrons of the dopant ion.

The action of the crystal field on the dopant ion has the effect of distorting the spherical symmetry of the free ion and splitting each $^{2S+1}L_J$ multiplet into different Stark levels, which lifts their degeneracy. This will depend on the point symmetry of the site where the rare-earth ion is located.

I-6. Lifting of degeneracy and Stark sublevels

The crystal field disturbs the spherical symmetry of the free ion, leading to a lifting of the degeneracy of the $^{2S+1}L_J$ multiplets and their splitting into several energy levels known as Stark sublevels. This splitting is strongly influenced by the local point symmetry of the site occupied by the dopant ion, as well as by the strength of the interactions with neighboring ions in the host matrix.
In the case of an isolated free ion, spherical symmetry preserves the degeneracy of the spectroscopic energy levels. When the ion is incorporated into a solid matrix, this

symmetry is reduced by the crystal field, and the degeneracy is partially or fully lifted. The resulting number of Stark sublevels depends on the electronic configuration of the ion and on the symmetry of the crystal field.

For the Yb^{3+} ion, which has an odd number of 4f electrons ($4f^{13}$), Kramers' theorem applies, and each energy level remains at least doubly degenerate.

Consequently, the J = 7/2 level splits into a maximum of four Stark doublets (J + 1/2 = 4).

In contrast, the Tb^{3+} ion, which contains an even number of 4f electrons ($4f^{8}$), is a non-Kramers ion. In this case, the crystal field can completely lift the degeneracy of the J = 6 level, resulting in the formation of up to (2J + 1 = 13) distinct Stark sublevels, whose energies depend on the local symmetry and strength of the crystal field.

This contrasted behavior between Yb^{3+} and Tb^{3+} ions highlights the crucial role played by the number of 4f electrons, the value of J, and the site symmetry in determining the energy-level structure of rare-earth ions in optically active materials.

I-7. Number of microstates of the $4f^{13}$ and $4f^{8}$ configurations

The number of possible microstates for a given electronic configuration can be calculated using combinatorial considerations according to:

$$N_L^X = \frac{N_L!}{n!(N_L - n)!} \qquad \text{(Eq. I-14)}$$

Where N_L represents the total number of available states in the considered shell and n is the number of electrons occupying this subshell. For the 4f shell, (N_L=14).

For the trivalent Yb^{3+} ion, which has a $4f^{13}$ configuration (n = 13), the number of possible microstates is:

$$N_L^X = \frac{14!}{13!(14-13)!} = 14 \text{ states} \qquad \text{(Eq. I-15)}$$

For the Tb^{3+} ion, which has a $4f^{8}$ configuration (n = 8), the number of possible microstates is:

$$N_L^X = \frac{14!}{8!(14-8)!} = 3003 \text{ states} \qquad \text{(Eq. I-16)}$$

These values correspond to the total number of combinatorial microstates associated with each electronic configuration and should not be confused with the spectroscopic degeneracy or the number of Stark sublevels, which are determined by the total angular momentum J and by crystal field effects.

I-8. Degeneracy of Spectroscopic Terms ^{2S+1}L

The spectroscopic term ^{2S+1}L is characterized by a spin multiplicity (2S + 1), corresponding to the possible values of the spin magnetic quantum number M_S ranging from –S to +S and by an orbital multiplicity (2L + 1), corresponding to the possible values of the orbital magnetic quantum number M_L ranging from –L to +L. Each pair (M_L, M_S) represents a distinct quantum state [11]. Therefore, the total degeneracy of a given spectroscopic term ^{2S+1}L is given by:

$$^{2S+1}L = (2S + 1)\,(2L + 1) \qquad \textbf{(}\text{Eq. I-17)}$$

I-8-1. Degeneracy of spectroscopic terms Tb^{3+}

In the case of the Tb^{3+} ion, which has a $4f^8$ electronic configuration, Hund's rules yield a total spin S = 3 and an orbital angular momentum L = 3, corresponding to the spectroscopic term ^7F. The degeneracy of this term is thus:

$(2 \times 3 + 1) \cdot (2 \times 3 + 1) = 7 \times 7 = 49$ states.

Table I-2: Determination of the Multiplicity of the Tb^{3+} Ion

-3	-2	-1	0	+1	+2	+3	Spin	Spin multiplicity $2\|S\| + 1$
↑↓	↑	↑	↑	↑	↑	↑	$\frac{6}{2}$	7 (Septet)
↑↓	↑	↑	↑	↑	↑	↓	$\frac{4}{2}$	5(Quintet)
↑↓	↑	↑	↑	↑	↓	↓	$\frac{2}{2}$	3(Triplet)
↑↓	↑	↑	↑	↓	↓	↓	$\frac{0}{2}$	1 (Singlet)
↑↓	↑	↑	↓	↓	↓	↓	$\frac{-2}{2}$	3(Triplet)
↑↓	↑	↓	↓	↓	↓	↓	$\frac{-4}{2}$	5(Quintet)
↑↓	↓	↓	↓	↓	↓	↓	$\frac{-6}{2}$	7(Septet)

I-8-2. Degeneracy of spectroscopic terms Yb^{3+}

As for the Yb^{3+} ion, it contains 13 electrons in the 4f shell, which is equivalent to a configuration with a single hole and can therefore be treated as a single-electron $4f^1$ configuration. This leads to a total spin S = 1/2 and an orbital angular momentum L = 3, corresponding to the spectroscopic term ^2F.

The total degeneracy of this spectroscopic term, prior to spin–orbit coupling, is given by:

$(2 \times 1/2 + 1) \cdot (2 \times 3 + 1) = 2 \times 7 = 14$ states

I-8-3. Degeneracy of spectroscopic terms Er^{3+}

The Er^{3+} ion, characterized by an electronic configuration of $4f^{11}$, can be conveniently described in terms of three holes, making it equivalent to a $4f^3$ configuration. According to Hund's rules, this leads to a total spin quantum number S = 3/2 and an orbital angular momentum L = 6, corresponding to the spectroscopic term ^4I. The degeneracy of this term prior to spin–orbit coupling is given by:

$(2S + 1)(2L + 1) = (2 \times 3/2 + 1)\ (2 \times 6 + 1) = 4 \times 13 = 52$ states

This high degeneracy is subsequently lifted by spin–orbit coupling, leading to the splitting into multiple J levels, with the ground state corresponding to $^4I_{15/2}$.

Table I-3: Russell–Saunders (LS) term symbols and degeneracies for the Tb^{3+} ($4f^8$), Yb^{3+} ($4f^{13}$) and Er^{3+} ($4f^{11}$) ions

Ion	Configuration	S	L	Terme LS	J	Fondamental level	Degeneracy
Tb^{3+}	$4f^8$	3	3	^7F	6	$^7F_6$	49
Yb^{3+}	$4f^{13}$	1/2	3	^2F	7/2	$^2F_{7/2}$	14
Er^{3+}	$4f^{11}$	3/2	6	^4I	15/2	$^4I_{15/2}$	52

The table I-4 lists all spectroscopic terms arising from the $4f^8$ electronic configuration, together with their corresponding spin multiplicities (2S+1) and orbital angular momentum quantum numbers, within the framework of Russell–Saunders (LS) coupling. Since the Tb^{3+} ion has an even number of 4f electrons, it is a non-Kramers ion, and its spectroscopic terms are not subject to Kramers degeneracy. Consequently,

in the absence of spin–orbit coupling, each LS term exhibits a total degeneracy given by (2S+1) (2L+1). These terms are subsequently split into J multiplets by spin–orbit interaction and further into Stark sublevels under the action of the crystal field, depending on the local site symmetry.

Table I-4: Russell–Saunders (LS) spectroscopic terms and spin multiplicities for the Tb^{3+} ion ($4f^8$ configuration) [12]

Configuration	Ion	Multiplicity	Multiplicity 2S+1	Spectroscopic Terms
$4f^8/4f^6$	Tb^{3+}/Eu^{3+}	Singlet	1	S, P, D, F, G, H, I, K, L, M, N, O, Q,
		Triplet	3	4, 6, 4, 8, 4, 7, 3, 4, 2,2
		Quintet	5	P, D, F, G, H, I, K, L, M, N, O
				6, 5, 9, 7, 9, 6, 6, 3, 3,
		Septet	7	S, P, D, F, G, H, I, K, L,
				3, 2, 3, 2, 2
				F

I-9. degeneracy of $^{2S+1}L_J$ multiplets

On the other hand, the multiplets, denoted $^{2S+1}L_J$, involves the eigenvalue of the total angular momentum J in addition to the eigenvalues S and L. The different possible values of the states. M_L and M_s can no longer be considered as good quantum numbers because L and S have been coupled, resulting in a state subjected to the action of the resultant spin-orbit coupling J. In this case, the number of states associated with the multiplet is determined solely by the number of possible values of M_J, since M_J could take values ranging from -J to +J. So, the total degeneracy of the multiplet $^{2S+1}L_J$ is then 2J + 1.

In order to distinguish the multiplets $^{2S+1}L_J$ corresponding to each spectroscopic term ^{2S+1}L, Hund's three rules were applied to the Terbium ion (Tb^{3+}) and Ytterbium (Yb^{3+}). The obtained results are presented in table I-5 and table I-6, respectively:

Table I-5: Spectroscopic term symbols and Russell–Saunders multiplets of the $4f^8$ configuration of the Tb^{3+} ion

Degeneracy	Septets (7)
Term ^{2S+1}L	F
2S+1	7

S	3
L	3
$\|\boldsymbol{L}-\boldsymbol{S}\| \leq \boldsymbol{J} \leq \|\boldsymbol{L}+\boldsymbol{S}\|$	$0 \leq J \leq 6$
J=	0, 1 ,2, 3, 4, 5, 6
$^{2S+1}L_J$ Multiples	^7F_J

Degeneracy	Singlet (1)											
Term ^{2S+1}L	S	P	D	F	G	H	I	K	L	M	N	O
2S+1	1	1	1	1	1	1	1	1	1	1	1	1
S	0	0	0	0	0	0	0	0	0	0	0	0
L	0	1	2	3	4	5	6	7	8	9	10	11
$\|L-S\| \leq J \leq \|L+S\|$	0≤J≤0	1≤J≤1	2≤J≤2	3≤J≤3	4≤J≤4	5≤J≤5	6≤J≤6	7≤J≤7	8≤J≤8	9≤J≤9	10≤J≤10	11≤J≤11
J=	0	1	2	3	4	5	6	7	8	9	10	11
$^{2S+1}L_J$ Multiples	$^2S_0$	$^2P_1$	$^2D_2$	$^2F_3$	$^2G_4$	$^2H_5$	$^2I_6$	$^2K_7$	$^2L_8$	$^2M_9$	$^2N_{10}$	$^2O_{11}$

Degeneracy	Triplets (3)										
Term ^{2S+1}L	P	D	F	G	H	I	K	L	M	N	O
2S+1	3	3	3	3	3	3	3	3	3	3	3
S	1	1	1	1	1	1	1	1	1	1	1
L	1	2	3	4	5	6	7	8	9	10	11
$\|L-S\| \leq J \leq \|L+S\|$	0≤J≤2	1≤J≤3	2≤J≤4	3≤J≤5	4≤J≤6	5≤J≤7	6≤J≤8	7≤J≤9	8≤J≤10	9≤J≤11	10≤J≤12
J=	0,1,2	1,2,3	2,3,4	3,4,5	4,5,6	5,6,7	6,7,8	7,8,9	8,9,10	9,10,11	10,11,12
$^{2S+1}L_J$ Multiples	$^3P_0$ $^3P_1$ $^3P_2$	$^3D_1$ $^3D_2$ $^3D_3$	$^3F_2$ $^3F_3$ $^3F_4$	$^3G_3$ $^3G_4$ $^3G_5$	$^3H_4$ $^3H_5$ $^3H_6$	$^3I_5$ $^3I_6$ $^3I_7$	$^3K_6$ $^3K_7$ $^3K_8$	$^3L_7$ $^3L_8$ $^3L_9$	$^3M_8$ $^3M_9$ $^3M_{10}$	$^3N_9$ $^3N_{10}$ $^3N_{11}$	$^3O_9$ $^3O_{10}$ $^3O_{11}$

Degeneracy	Quintets (5)								
Term ^{2S+1}L	S	P	D	F	G	H	I	K	L
2S+1	5	5	5	5	5	5	5	5	5
S	2	2	2	2	2	2	2	2	2
L	0	1	2	3	4	5	6	7	8

$\|L - S\| \leq J \leq \|L + S\|$	2≤J≤ 2	1≤J≤3	0≤J≤4	1≤J≤5	2≤J≤ 6	3≤J≤7	4≤J≤8	5≤J≤9	6≤J≤10
J=	2	1,2 ,3	0,1,2,3,4	1,2,3,4, 5	2,3,4, 5,6	3,4,5,6,7	4,5,6,7,8	5,6,7,8,9	6,7,8,9,10
$^{2S+1}L_J$ Multiples	$^5S_2$	$^5P_1$ $^5P_2$ $^5P_3$	$^5D_0$ $^5D_1$ $^5D_2$ $^5D_3$ $^5D_4$	$^5F_1$ $^5F_2$ $^5F_3$ $^5F_4$ $^5F_5$	$^5G_2$ $^5G_3$ $^5G_4$ $^5G_5$ $^5G_6$	$^5H_3$ $^5H_4$ $^5H_5$ $^5H_6$ $^5H_7$	$^5I_4$ $^5I_5$ $^5I_6$ $^5I_7$ $^5I_8$	$^5K_5$ $^5K_6$ $^5K_7$ $^5K_8$ $^5K_9$	$^5L_6$ $^5L_7$ $^5L_8$ $^5L_9$ $^5L_{10}$

Table I-6: Spectroscopic term symbols and Russell–Saunders multiplets of the $4f^{13}$ configuration of the Yb^{3+} ion

Degeneracy	doublet (2)
Term ^{2S+1}L	F
2S+1	2
S	½
L	3
$\|\boldsymbol{L} - \boldsymbol{S}\| \leq \boldsymbol{J} \leq \|\boldsymbol{L} + \boldsymbol{S}\|$	$5/2 \leq J \leq 7/2$
J=	5/2, 7/2
$^{2S+1}L_J$ Multiples	^2F_J

I-10. Selection Rules for Optical Transitions

The interaction of rare earth ions with electromagnetic radiation can lead to transitions between the energy levels $^{2S+1}L_J$, transitions governed by selection rules. The interaction of the rare earth electrons with the crystal field primarily leads to two types of transitions [13]: electric dipole transitions and magnetic dipole transitions.

When the introduction of a rare earth ion into a matrix, it experiences the influence of the matrix's crystal field. The states of the configuration are then combined with those of the initial excited configuration. Electric dipole transitions are permitted and are referred to as forced dipole transitions. By using the Judd and Ofelt model [14, 15], which describes the intensities of these transitions and considering the various spin-orbit coupling terms and the crystal field, the selection rules for forced electric dipole transitions can be defined as:

$\Delta l = \pm 1$; $\Delta L \leq 6$; $\Delta S = 0$; $|\Delta J| \leq 6$

Magnetic dipole transitions are much less intense than electric dipole transitions. The selection rules for an ion present in a matrix are defined by:

Δl = 0 (No change in parity) ; ΔJ = 0, ±1 ; ΔL = 0, ±1 ; ΔS = 0

I-11. Interaction of rare earth ions with electromagnetic radiation

There are interactions of rare earth ions with electromagnetic radiation. This interaction will give rise to transitions between the different energy levels of the ions, which can be classified into two categories depending on whether they are accompanied or not by the exchange of a photon:

-Radiative transitions.

-Nonradiative transitions.

I-11-1. Radiative transitions

a) Absorption

Let us consider an electromagnetic wave composed of photons with energy E = hν passing through a material containing rare-earth ions. If the photons possess energy around the energy difference ΔE between the ground state and the excited state, they may be absorbed by the rare-earth ion, resulting in a transition from the ground state to the excited state. Figure (I-5a) illustrates the absorption process.

$$I_t(\lambda) = I_0 e^{-OD(\lambda)} \qquad \text{(Eq. I-18)}$$

Where:

$I_0(\lambda)$ is the incident light intensity for a given monochromatic radiation. $I_t(\lambda)$ Represents the light intensity transmitted through the sample of thickness L. $OD(\lambda)$ Represents the optical density.

The absorption spectrum is represented by the curve DO(λ) = f(λ), a dimensionless number that is contingent upon the thickness L of the sample.

To eliminate the dependence on dopant ion concentration and the sample thickness, the concept of the absorption cross-section σ_{abs} , expressed in cm², is more commonly used. It is derived from the optical density as follows:

$$I_t(\lambda) = I_0 e^{-N\sigma_{abs}L} \qquad \text{(Eq. I-19)}$$

$$\sigma_{abs}(\lambda) = 2.3 \times \frac{DO(\lambda)}{N_{total}.L} \quad \text{(Eq. I-20)}$$

N_{total} : The ion density is expressed in ions/cm³, whereas L denotes the sample thickness in centimeters. The absorption cross-section σ_{abs} is defined as the proportionality constant relating the probability of photon absorption to the ion density per unit area. The values of the absorption cross-section can be derived from the absorption spectra measurements. These actions are performed using a double-beam spectrophotometer. A white light beam is directed towards a monochromator to select the wavelength **λ**, which is then split into two beams of equivalent power: the reference beam with intensity $I_0(\lambda)$and the beam that has passed through the sample with intensity $I_t(\lambda)$.

b) Emission

- **spontaneous emission**

Once in its excited state and without any external action, the rare earth ion spontaneously returns to its minimum energy state. Light is then emitted, which is the phenomenon of spontaneous emission Figure I-5b. The variation in the population of ions between energy levels E_1 and E_2 can be written as:

$$\frac{dN_1}{dt} = A_{21}.N_1 = -\frac{dN_2}{dt} \quad \text{(Eq. I-21)}$$

A_{21} is the Einstein coefficient, which corresponds to the probability of spontaneous emission per unit time. It is expressed in s^{-1} and is inversely proportional to the radiative lifetime of the energy level E_2.

$$A_{21} = \frac{1}{\tau_{rad}} \quad \text{(Eq. I-22)}$$

There may be several energy levels E_j below the excited level E_m. The ions can then undergo spontaneous transitions to each of these levels. For each transition, a spontaneous emission probability A_{mj} can be established. The overall likelihood of de-excitation is the aggregate of all these probabilities, and the radiative lifespan is:

$$\tau_{rad} = \frac{1}{\sum_j A_{mj}} \quad \text{(Eq. I-23)}$$

The branching ratio β for a given transition is then defined by the following relation:

$$\beta = \frac{A_{mj}}{\sum_j A_{mj}} = A_{mj}.\tau_{rad} \qquad \text{(Eq. I-24)}$$

- **Stimulated emission**

The incident electromagnetic wave can lead to the de-excitation of an electron in the state E_2 by the emission of a photon with the same properties (wavelength, phase, direction, and polarization) as the incident photon. Stimulated emission works as a duplication of light. Its realization requires a population exchange between levels E_2 and E_1. Figure I-5c illustrates the stimulated emission of a photon.

The concept of stimulated emission serves as the foundation for the laser effect. To be effective, it is necessary that:

- Stimulated emission prevails over absorption. Thus, N_2 must be much greater than N_1 (N_1 and N_2 represent the population of levels 1 and 2), which means there must be a population inversion compared to the thermal equilibrium state.
- Stimulated emission prevails over spontaneous emission, a condition fulfilled when the photon flux density ρ(v) is high. Thus, the amplifier must be positioned inside a laser cavity consisting of two parallel mirrors: one reflects 100% and the other reflects between 95% and 99%, depending on the laser wavelength. The laser material, under optical or electrical stimulation, generates radiation that is intensified within the laser cavity. An intense and coherent light beam is produced from the mirror transmitting 1-5%.

The population equation for levels 1 and 2 is formulated as follows:

$$\frac{dN_2}{dt} = -N_2.B_{21}.\rho(V) \qquad \text{(Eq. I-25)}$$

Where $\rho(V)$ is the spectral energy flux density of the photons.

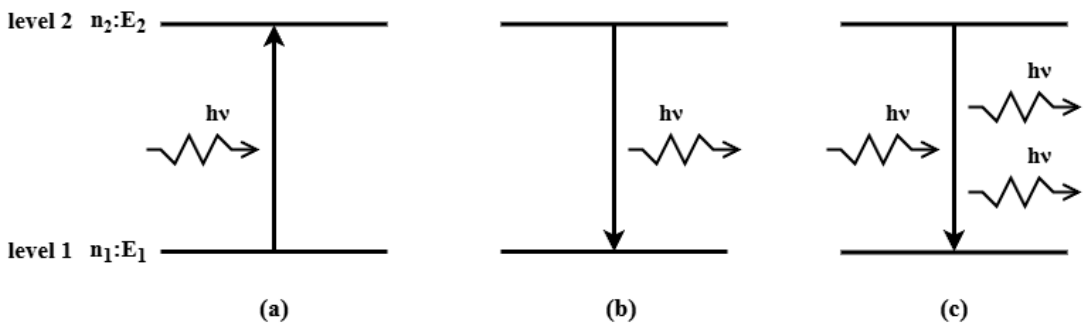


Figure I-5: (a) Absorption of a photon with energy hν, equivalent to the energy differencebetween levels 1 and 2 hν = E_2 - E_1. (b) Spontaneous emission of a photon withenergy hν=E_2-E_1, emitted in any direction in space. (c) Stimulated emission of a photon with energy hν, under the influence of an incident photon with energy hν. The two emitted photons are identical: same frequency, same phase, same direction. They are said to be coherent.

I-11-2. Non-radiative transitions

The atom can sometimes return to its ground energy state by releasing energy to the lattice through the creation of phonons; this transition is then termed non-radiative. Non-radiative transitions are clearly more influenced by the composition of the matrix (for example, oxide or fluorinated matrix) than radiative transitions. The Schrödinger equation summarizes that the probability of non-radiative transition increases with temperature and decreases as the energy gap between the levels increases. If the electronic states are close enough, on the scale of KT, the transitions will occur rapidly. This causes the thermal occupation of the higher levels.

$$W_{nr}^{p}(T) = W_{nr}^{p}(0).\left(\frac{\exp\left(\frac{\Delta E}{KT}\right)}{\exp\left(\frac{\Delta E}{KT}\right)-1}\right) \qquad \text{(Eq. I-26)}$$

Where:

ΔE: the energy gap between the concerned levels.

P: the number of phonons in the matrix.

$W_{nr}^{p}(0)$: the transition probability at 0 K with $W_{nr}^{p}(0) = \beta_{el}\exp(-\alpha(\Delta E - 2h\omega_{max}))$

β_{el} and α represent the experimental parameters.

$h\omega_{max}$: the maximum energy of the matrix phonons.

During a relaxation process, when the added energy exceeds the maximum energy of the phonon associated with the material, several phonons can form simultaneously, leading to the designation of multi-phonon relaxation. If the non-radiative relaxation rate of a level is similar to its radiative transition rate, the efficiency of the luminescence process associated with that level deteriorates. We refer to vibrational transitions to define those that involve both a photon and one or more vibrational levels.

No-radiative transitions have both positive and unfavorable impacts, as they offer the possibility to occupy or release a certain level. Thus, they offer the possibility to optimize or reduce the yield of a specific transition based on the criteria [16].

I-12. Energy transfer between rare-earth ions

When the concentration of rare-earth ions is increased in a host matrix, either for the same type of ion or for different types (codoping), ion-ion interactions occur. Generally, this phenomenon takes place when the average distance between ions reaches a few nanometers, that is, assuming a uniform distribution, when the ion concentration reaches 10^{27} m^{-3}. In the case of codoping, understanding such phenomena is crucial to explain the different optical processes involved in rare-earth-doped ions in solid matrices. Energy transfer occurs when absorption and emission do not take place at the same site. One can distinguish between radiative and non-radiative transfer, resonant transfer, and phonon-assisted transfer.
There are different types of interaction between ions that lead to the depopulation of an excited state [17]. The likelihood of energy transfer correlates with the overlap between the donor ion's emission and the acceptor ion's absorption.

I-12-1. Resonant or phonon-assisted energy transfer

In the case of resonant energy transfer, the interacting neighboring ions possess matching or nearly matching energy levels. The donor ion D, initially in its excited state D*, relaxes to its ground state or to a lower-energy level, while the acceptor ion A absorbs the released energy and is promoted from its ground state to an excited state A* (Figure I-6a). This process requires a significant spectral overlap between the emission spectrum of the donor ion and the absorption spectrum of the acceptor ion.

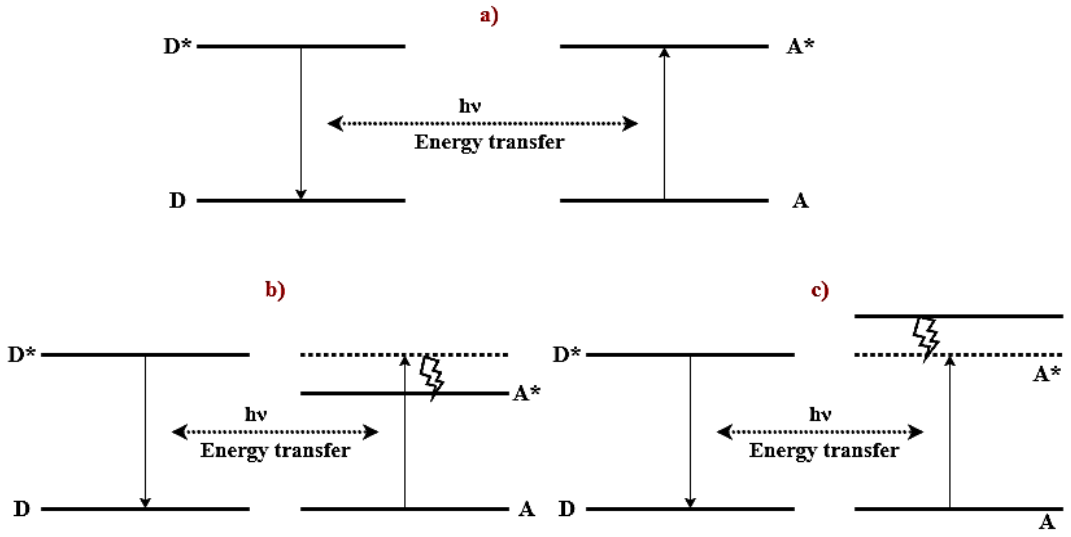


Figure I-6: (a) Resonant energy transfer and energy transfer assisted by: (b) emission of phonons (c) phonon absorption

In the case where the energy difference between the involved donor and acceptor levels is not strictly resonant, the process is referred to as non-resonant or phonon-assisted energy transfer. In order to satisfy total energy conservation, the emission or absorption of one or more phonons from the host lattice may occur, depending on whether the energy released during the donor transition D* → D is greater than or smaller than the energy required for the acceptor transition A → A* (Figures I-6b and c).

I-12-2.Direct Transfer

Direct transfer, illustrated in figure I-6a, is a non-radiative mechanism in which two ions, one in an excited state (donor) and the other in the ground state (acceptor), interact resonantly so that the donor transfers its excitation energy to the acceptor without the emission of a real photon.

I-12-3. Energy migration

Energy migration is a non-radiative resonant energy transfer process that becomes increasingly efficient as the concentration of trivalent lanthanide ions (RE^{3+}) increases, resulting in shorter interionic distances. In this mechanism, energy is transferred between neighboring ions that possess identical or nearly identical energy levels.

When an acceptor ion A is initially in its ground state, a donor ion D in an excited state can relax to its ground state while simultaneously transferring its excitation energy to

the acceptor ion, promoting it to an excited state. This excitation can then be transferred step by step between equivalent Ln^{3+} ions within the host matrix, a process referred to as energy migration (Figure I-7).

Energy migration typically ends when the excitation is transferred to a specific acceptor ion or to a quenching center, also called a trap, which increases the probability of non-radiative de-excitation and luminescence quenching. Such traps may correspond to impurities, defects, or clustering centers within the material [18, 19].

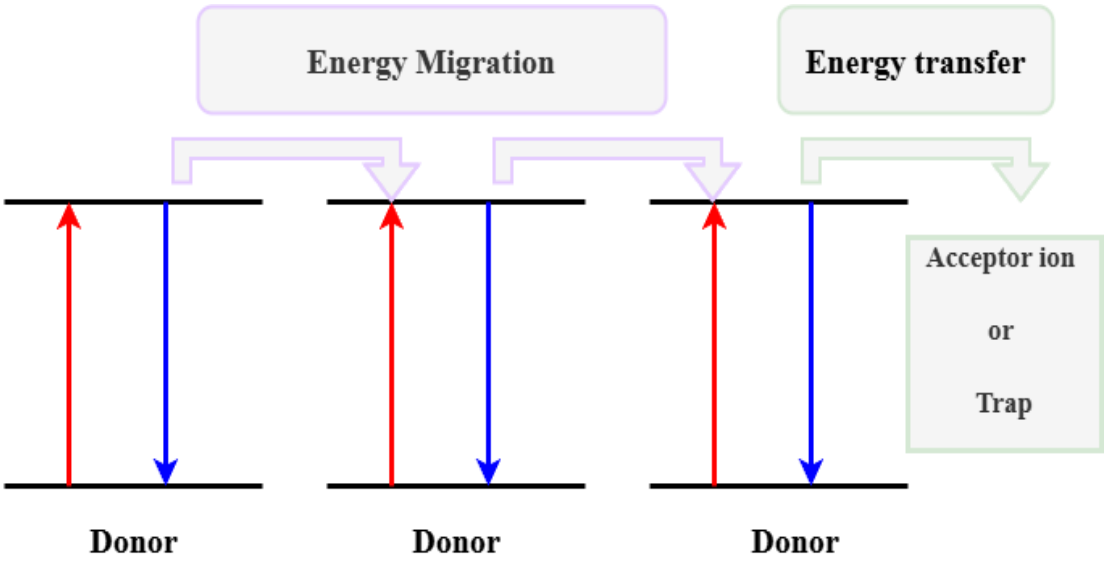


Figure I-7: Non-radiative resonant transfer (energy migration)

I-12-4. Cross relaxation

This mechanism may occur between distinct ions or ions of same types. The transfer is referred to as cross-relaxation when, at the conclusion of the transfer, the electrons of the donor ion are not in the ground state but occupy an energy level between D^{**} (initially excited) and D (fundamental) (Figure I-8). When this transfer occurs between two ions of the same kind, it is referred to as self-quenching.

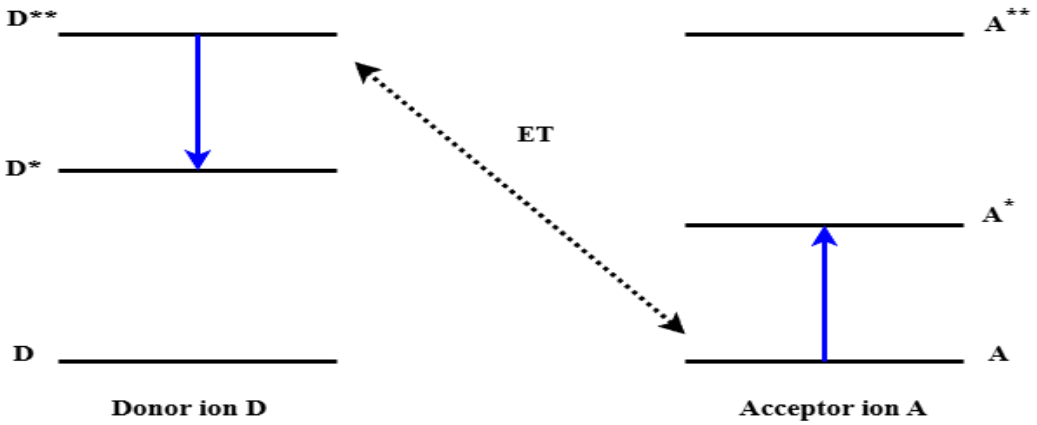


Figure I-8: Principle of energy transfer (ET) by cross-relaxation

I-13. Energy transfer by up-conversion (APTE)

The term *up-conversion* refers to a process in which the emitted fluorescence photon has a shorter wavelength (higher energy) than that of the photons used for optical pumping.

The up-conversion process can occur through two main mechanisms:

• **Sequential absorption of two photons (Excited-State Absorption, ESA):** In this case, a first photon with energy $h\nu_1$ populates an intermediate so-called reservoir level (level A* in figure I-9a). A second photon with energy $h\nu_2$ is then absorbed from this excited state, promoting the ion to a higher excited level (level A**). Radiative emission subsequently occurs from this level to the ground state, with an emitted photon energy $h\nu_e$ such that:

$$h\nu_e > h\nu_1 \qquad \text{And} \qquad h\nu_e > h\nu_2$$

• **Photon addition by energy transfer (APTE):**

This mechanism, first demonstrated by F. Auzel in 1966 [20], involves two neighboring ions, referred to as the *donor* and the *acceptor*, both initially in their excited states (D* and A*). Through a non-radiative resonant interaction, the donor ion transfers its excitation energy to the acceptor ion. As a result, the donor relaxes to its ground state D, while the acceptor is promoted to a higher excited state A** (figures I-9b). The subsequent radiative relaxation of this state leads to up-converted emission

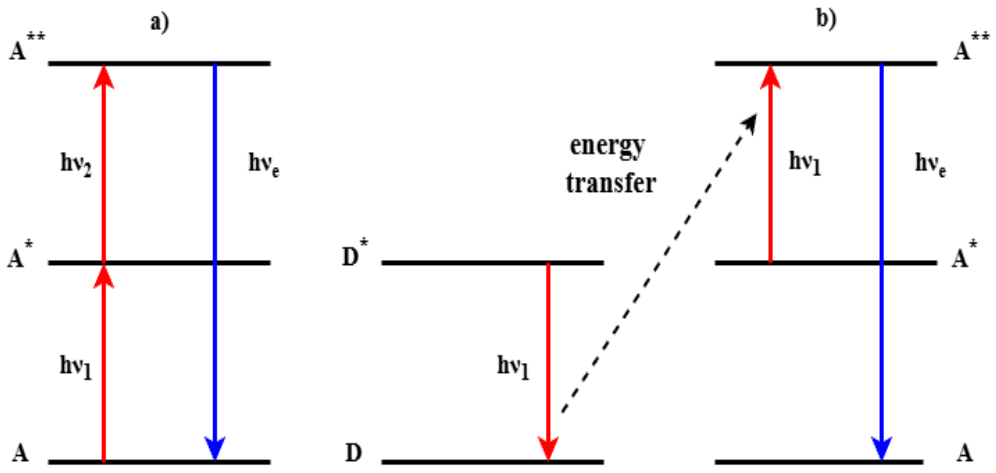


Figure I-9: Mechanism of energy transfer by up conversion (a) Sequential absorption process (b) Photon addition process by energy transfer (PAET)

The two processes may compete; APTE (Energy Transfer Up conversion) will occur when the rare earth ions are close to each other, which happens at high concentrations.

I-14. Energy transfer by down-conversion

In the down conversion process, two mechanisms are distinguished: the Down-Shifting (DS) mechanism and the Quantum-Cutting (QC) mechanism.

a) Down-Shifting

This mechanism allows the generation of a low-energy photon from a higher-energy photon. It generally follows Stokes' law, with the excess energy dissipated as phonons. The Down-Shifting mechanism can occur through two different pathways (Figure I-10):

- An ion absorbs a high-energy photon and emits a lower-energy photon itself (Figure I-10a).
- An ion absorbs a high-energy photon and then transfers its energy to another ion, which emits a lower-energy photon (Figure I-10b).

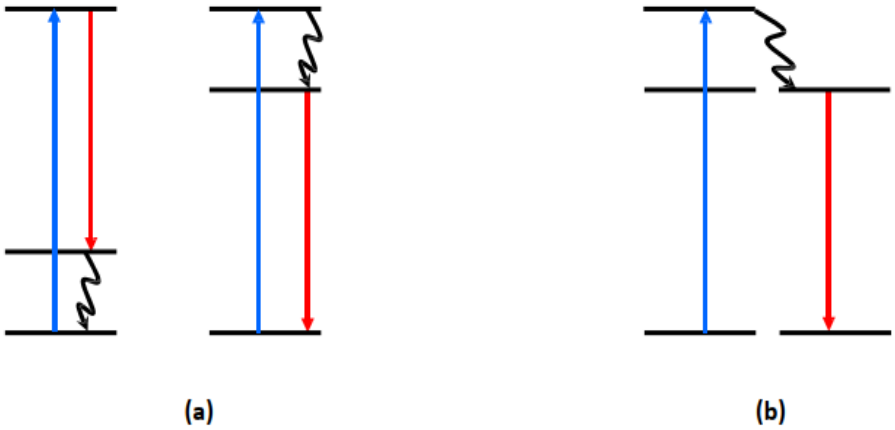


Figure I-10: The mechanisms of Down-Shifting with (a) one ion and (b) two ions

b) Quantum-Cutting

The second mechanism characterizing the down conversion process is Quantum-Cutting, a process with an internal quantum emission efficiency (number of photons emitted/number of photons absorbed) greater than 100%, and which can reach up to 200% [21, 22-24].In this process, a single highly energetic incident photon (VUV or UV) is split into two or more lower-energy photons (visible). This can occur through two different pathways:

- **The first pathway** involves a single type of rare-earth ion possessing at least three energy levels. When such an ion absorbs a high-energy photon, it emits two lower-energy photons (Figure I-11a). This process is also called a cascade emission.
- **The second pathway** involves a pair of different types of rare-earth ions (Figure I-11b–d). Three possible cases are distinguished:
    - First case: The type I ion, which has three energy levels, absorbs the excitation energy and transfers it to two type II emitter ions through a cross-relaxation energy transfer followed by a direct transfer (Figure I-11b), resulting in the emission of two photons.
    - Second case: The type I ion absorbs the excitation energy and transfers part of it to a type II emitter ion via cross-relaxation. Eventually, both ions relax to their ground states, each emitting one photon) Figure I-11c).

- **Third case:** After absorbing the excitation energy, the type I ion emits the first photon and then transfers the remaining energy directly to a type II ion, which emits the second photon (Figure I-11d).

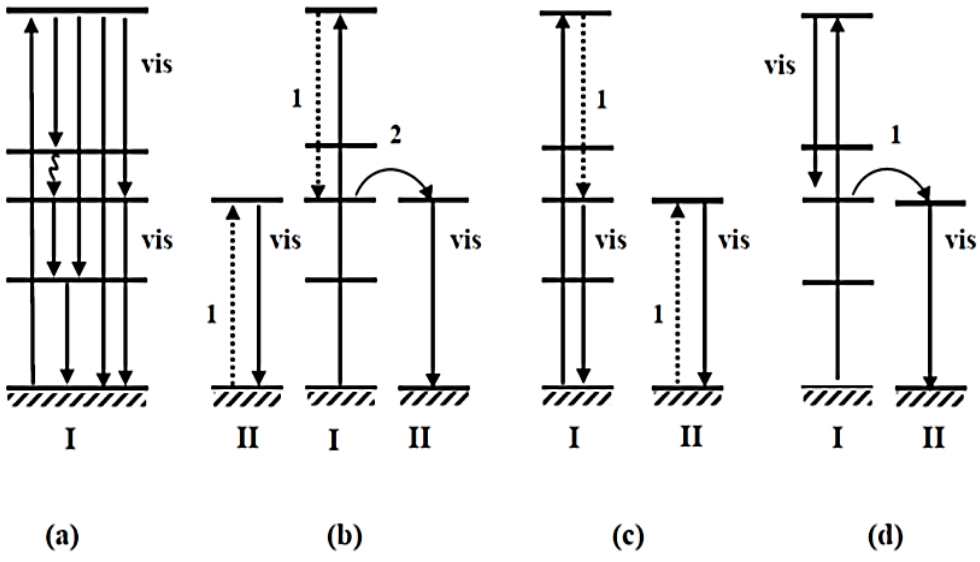


Figure I-11: Different energy transfer processes through Quantum-Cutting

I-15. Spectroscopic characteristics of the studied TR^{3+} ions

I-15-1. The ion Ytterbium (Yb^{3+})

a) Characteristics of the trivalent ytterbium ion (Yb^{3+})

The trivalent ytterbium ion (Yb^{3+}) has the electronic configuration [Xe] $4f^{13}$, meaning it has 13 electrons in the active 4f shell. This ion belongs to the lanthanide series, where the 4f electrons are partially shielded by the outer shells ($5s^25p^6$). This shielding makes its optical properties relatively insensitive to the host lattice, but they remain sensitive to the local symmetry of the ion's position within the material [25].

Yb^{3+} has a simple two-level structure, unlike other rare earth ions with complex energy structures:

The ground state of Yb^{3+} is: $^2F_{7/2}$.

The only excited state is: $^2F_{5/2}$.

The ground state $^2F_{7/2}$ is the lowest energy level, with a degeneracy of 2J+1 = 8 times. The electronic transitions in Yb^{3+} are of the f–f type and primarily occur between the $^2F_{7/2}$ and $^2F_{5/2}$ levels. These transitions are forbidden according to the selection rules because they conserve parity, but they become partially allowed due to the crystal field effect, which mixes states of different parity. Some of these transitions can also be of the magnetic dipole type.

The Yb^{3+} ion exhibits absorption and emission spectra predominantly in the near-infrared (NIR) region, namely near a wavelength of 980 nanometers [26]. The transitions noted in the absorption and emission spectra relate to electronic transitions between the Stark sublevels of the excited state $^2F_{5/2}$ and the ground state $^2F_{7/2}$.

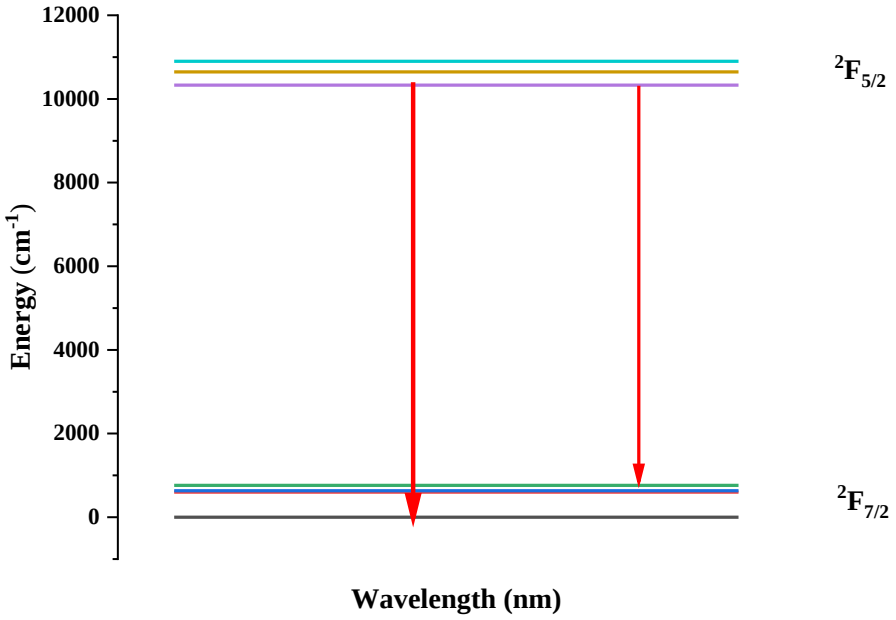
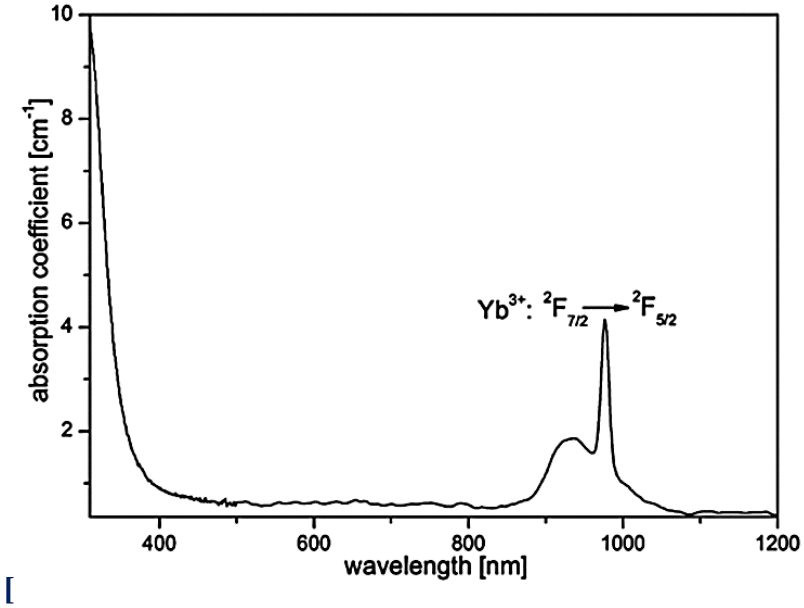


Figure I-12: Energy Level Diagram of Yb^{3+} Ion

According to the article Spectroscopic Properties of (Yb^{3+}/Tb^{3+}) Doped Germanate Glasses, the absorption spectrum shown in Figure I-13 indicates that the glass exhibits high transparency in both the visible and near-infrared regions. A broad absorption band centered at 976 nm is characteristic of Yb^{3+} ions and corresponds to the electronic transition between the $^2F_{7/2}$ ground state and the $^2F_{5/2}$ excited state [27]. Furthermore, in the article Optical Properties of Yb^{3+}-Doped NBSAZB Glasses for IR Lasers, the absorption spectrum presented in Figure I-14 shows an increase attributed to electronic

transitions between the Stark sublevels of the $^2F_{7/2}$ ground state and the $^2F_{5/2}$ excited state. The absorption spectra of Yb^{3+}-doped NBSAZB glasses, for concentrations ranging from 0 to 2.0 mol%, exhibit a main absorption band centered at 976 nm, along with two weaker sub-bands located at approximately 919 nm and 953 nm. All samples display similar spectral features, with the absorption intensity increasing as the Yb^{3+} concentration rises [28].



[

Figure I-13: Absorption coefficient of the germanate glass doped with 0.7 Yb_2O_3/0.7 Tb_2O_3 [27]

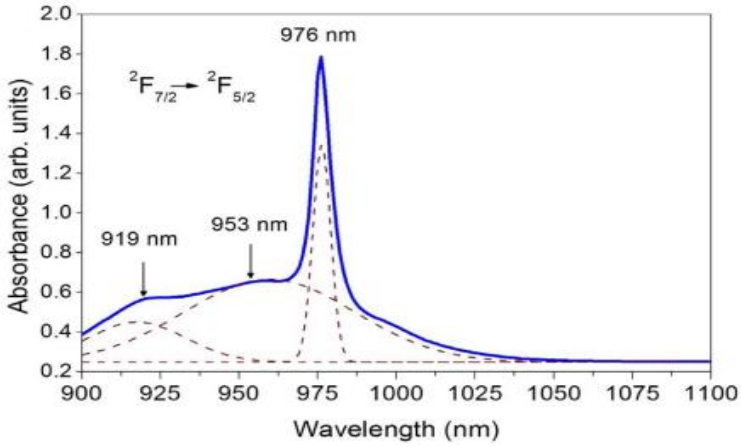


Figure I-14: Deconvolution of the absorption spectrum of NBSAZBYb10 glass [28]

According to the article "Optical properties of Yb^{3+}-doped NBSAZB glasses for IR lasers", the near-infrared (NIR) emission spectrum of NBSAZBYb glass under 808 nm

laser excitation, as shown in Figure 7, exhibits a main emission band centered at 975 nm. This band is accompanied by two prominent sub-peaks at 1002 nm and 1025 nm, along with a weaker emission peak around 1052 nm. The inset of Figure I-15 displays the deconvolution of the emission spectrum of NBSAZBYb10 glass within the spectral range of 990–1075 nm. Due to its low intensity, the emission peak at 1052 nm was not deconvoluted. All these emission characteristics are ascribed to the transition from the excited state $^2F_{5/2}$ to the ground state $^2F_{7/2}$, which is divided into three Stark sub-levels [30].

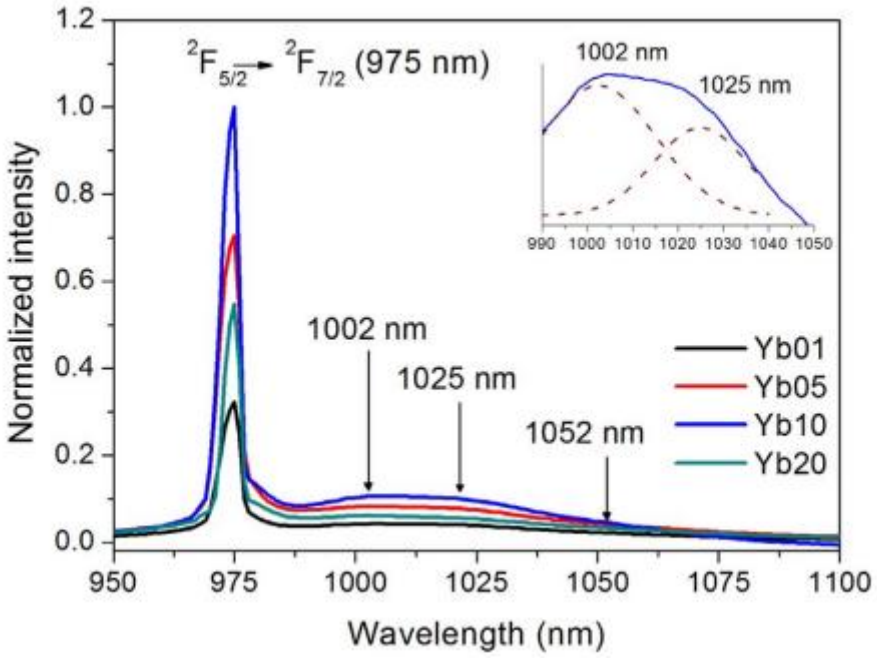


Figure I-15: Emission spectra of NBSAZBYb glasses. Inset shows the deconvolution of the emission spectrum in the spectral region from 990 nm to 1050 nm [28]

I-15-2. The ion Terbium (Tb^{3+})

a) Characteristics of the trivalent Terbium ion (Tb^{3+})

The trivalent Terbium ion (Tb^{3+}) has the electronic configuration [Xe] $4f^8$, which means it has 8 electrons in the active 4f layer. It belongs to the series of trivalent rare earths, where the 4f electrons are partially shielded by the outer layers ($5s^25p^6$), which makes its optical properties relatively insensitive to the host lattice, but sensitive to local symmetry.

The structure of the energy levels of the Tb^{3+} ion is complex. The ground term is $^7F_6$. The most important excited levels for luminescence are the $^5D_3$ and $^5D_4$ levels, from which radiative transitions to the ^7F_j multiplets (J = 0 – 6) occur [30, 31].

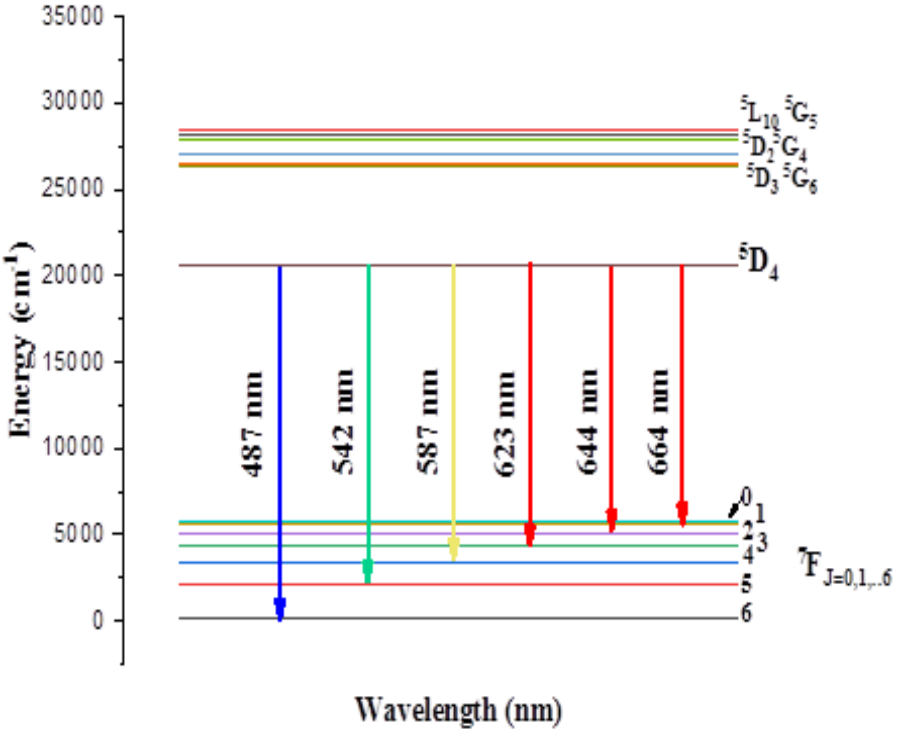


Figure I-16: Energy Level Diagram of Tb^{3+} Ion

In the case of optical absorption, and according to the results presented in the article by *H. Boubekri and al.*, titled "Synthesis and optical properties of Tb^{3+} doped CdF_2 single crystals," the UV-visible absorption spectrum of the 1% Tb^{3+} doped CdF_2 single crystal shows seven bands located at 316, 326, 341, 350, 368, 379, and 487 nm, corresponding respectively to the following transitions: $^7F_6 \rightarrow {}^5H_6$, $^5H_7 + {}^5D_0$, $^5L_9$, $^5G_4 + {}^5D_2 + {}^5G_5$, $^5L_{10}$, $^5G_6 + {}^5D_3$, and $^5D_4$ (Figure I-17a). The infrared range, on the other hand, presents three absorption bands located at 1815,
1890, and 2264 nm, attributed respectively to the transitions: $^7F_6 \rightarrow (^7F_0 + {}^7F_1)$, $^7F_2$, $^7F_3$ (Figure I-17b) [30, 31].

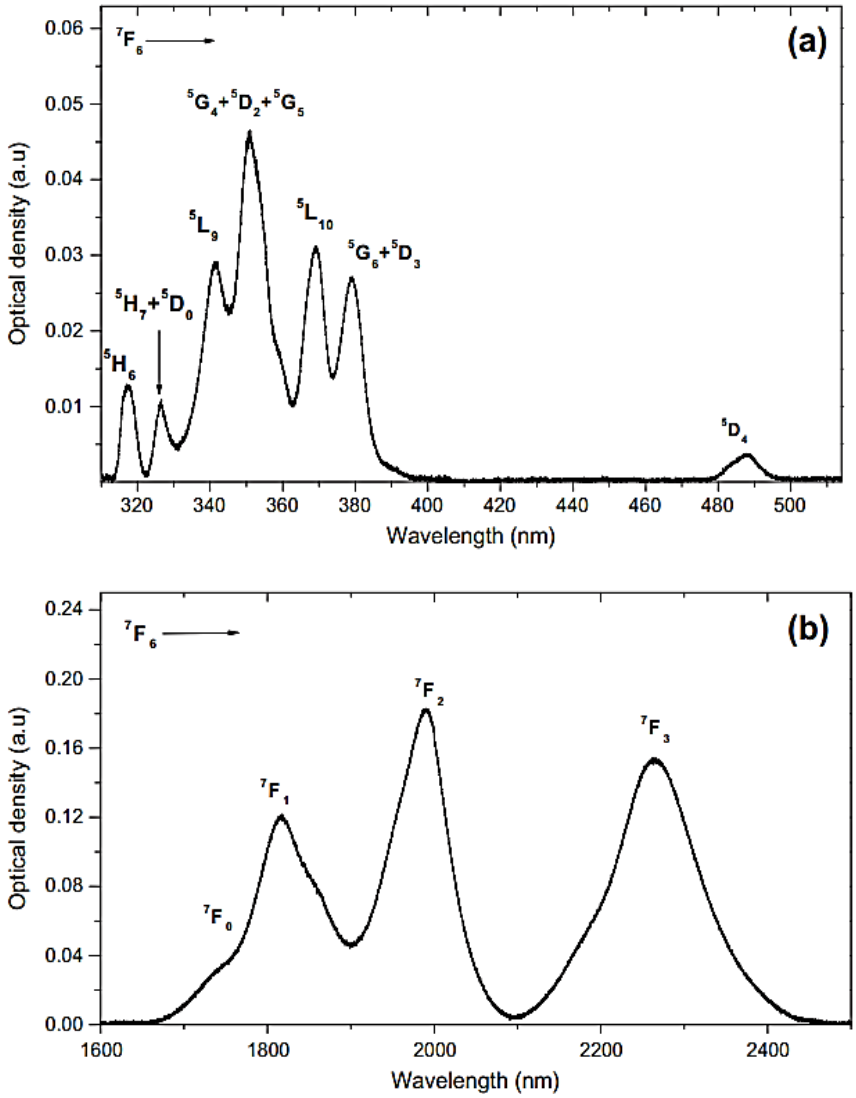


Figure I-17: Room temperature absorption spectra of Tb^{3+} doped CdF_2 single crystal (a) UV–Visible range, and (b) near infrared range [29, 30]

In the study conducted by H. Boubekri et al., the room-temperature excitation spectrum of CdF_2 single crystal doped with 1% Tb^{3+}, monitored at 532 nm (corresponding to the $^5D_4 \rightarrow {}^7F_5$ transition), displays several well-resolved peaks in the 200–550 nm range (Figure I-18). These are attributed to intra-configurational $4f^8 \rightarrow 4f^8$ transitions of the Tb^{3+} ion. Among them, the $^7F_6 \rightarrow {}^5D_2$ transition at 350 nm is the most prominent and was chosen as the excitation wavelength for recording the emission spectrum.

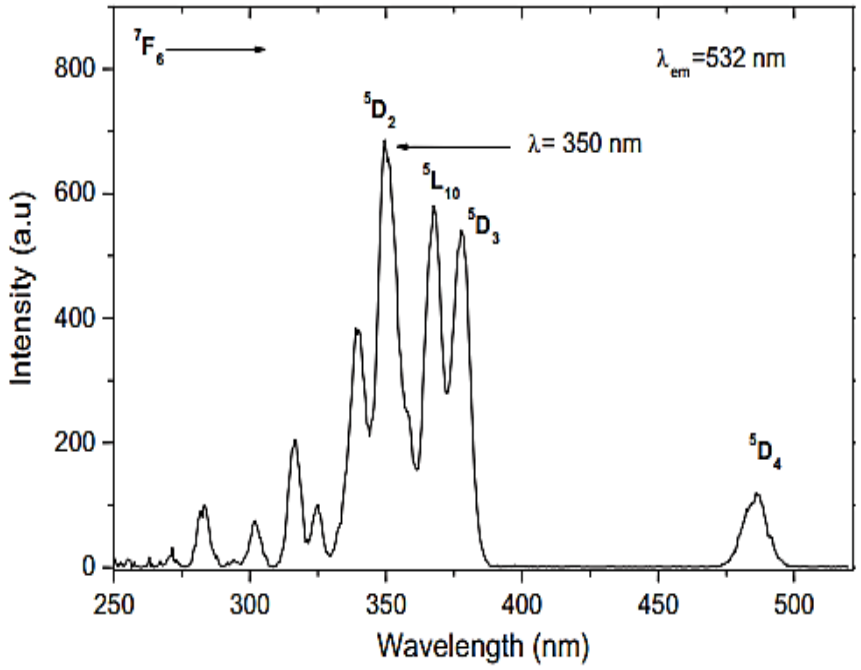


Figure I-18: Excitation spectrum of Tb^{3+}doped CdF2 single crystal recorded in the UV– Visible spectral range 250–525 nm [30]

The emission spectrum in Figure I-19, measured between 350 and 700 nm, reveals two distinct groups of emission lines:

- The first group, originating from the $^5D_3$ excited state, involves transitions to ^7F_j levels (J = 6, 5, 4, 3, 2), producing peaks at 370, 402, 424, 446, and 461 nm.
- The second group, derived from the $^5D_4$ state, pertains to transitions to ^7F_j (J = 6, 5, 4, 3), exhibiting emission peaks at 478, 532, 572, and 612 nm.

In both series, the $^5D_3 \rightarrow {}^7F_5$ and $^5D_4 \rightarrow {}^7F_5$ transitions are the most intense, emphasizing their crucial role in the characteristic green emission of Tb^{3+} in the CdF_2 host lattice [30, 32].

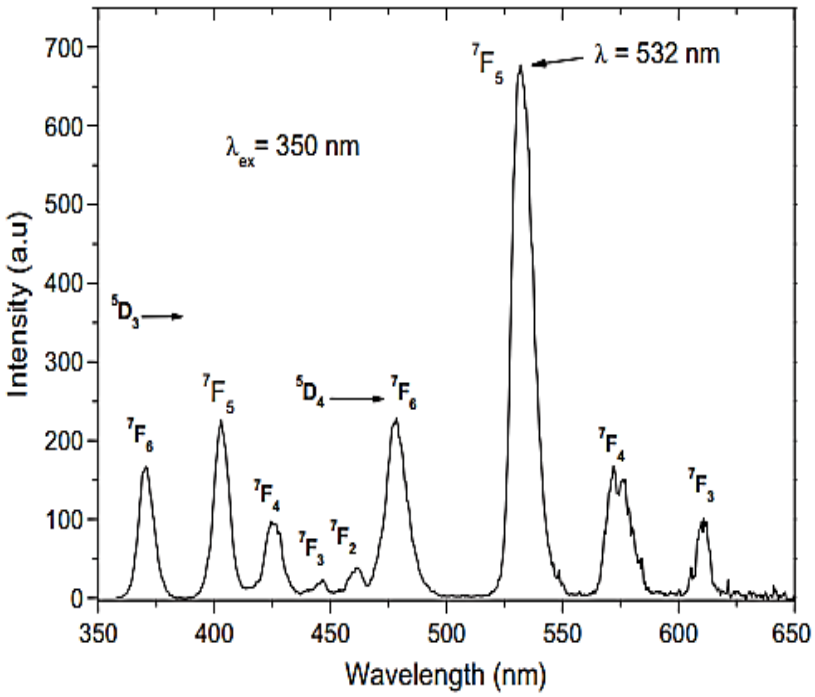


Figure I-19: Fluorescence spectrum of Tb^{3+}doped CdF_2 single crystal under excitation wavelength λ = 350 nm [28] [30]

I-15-3. The ion Erbium (Er^{3+})

The trivalent erbium ion (Er^{3+}) in its ground configuration possesses 11 optically active electrons in the 4f electronic subshell**.** This configuration leads to 12 doublets**:** [^{2}P, ^{2}D(1), ^{2}D(2), ^{2}F(1), ^{2}F(2), ^{2}G(1), ^{2}G(2), ^{2}H(1), ^{2}H(2), ^{2}I, ^{2}K, ^{2}L] and **5 quartets**: [^{4}S, ^{4}D, ^{4}F, ^{4}G, ^{4}I] [33], which give rise to 41 fine-structure energy levels distributed over an energy range of about 70 000 cm^{-1}**.**

The first energy levels from 0 to 35 000 cm^{-1} are presented in Figure I-20. In a low-symmetry crystal field, these 41 levels split into 182 Kramers doublets. In principle, 364 energy levels should appear; however, Kramers et al [34, 35] demonstrated that for ions with an odd number of electrons, the Stark levels remain doubly degenerate**.**

In 1996 [36], 16 transitions were identified for which laser action had been achieved between the energy levels of the erbium ion in oxides and fluorides. Current research mainly focuses on green and red spectral emissions ($^4S_{3/2}$, $^4F_{9/2} \rightarrow {}^4I_{15/2}$), which can occur through up conversion processes ($\lambda_{pump} > \lambda_{emission}$) [37, 38]. Other important

transitions are also studied, such as: $^4I_{13/2} \rightarrow {}^4I_{15/2}$ ($\lambda \approx 1.55$ µm), $^4I_{11/2} \rightarrow {}^4I_{13/2}$ ($\lambda \approx 2.8$ µm), $^4I_{11/2} \rightarrow {}^4I_{15/2}$ ($\lambda \approx 0.98$ µm).

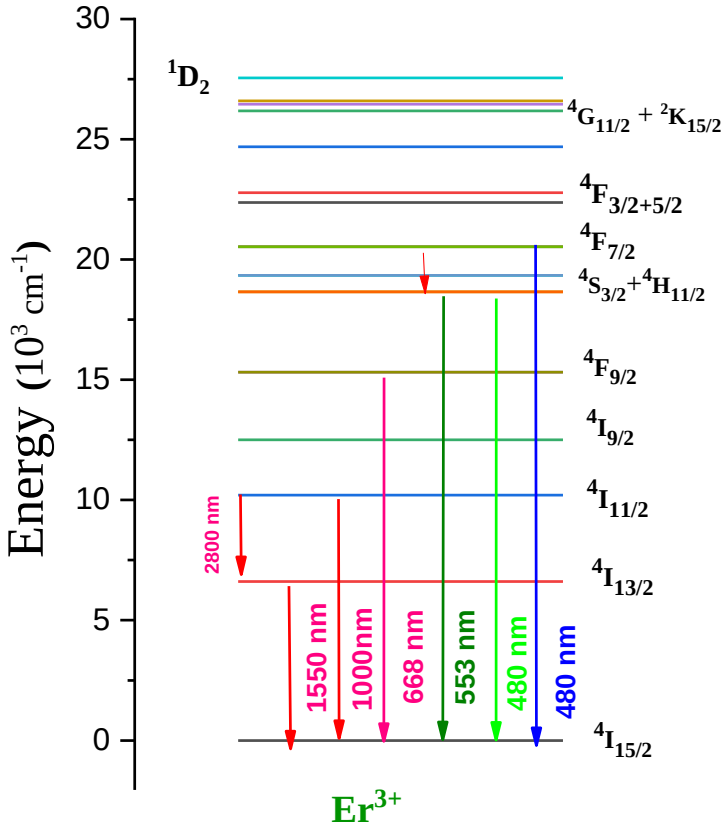


Figure I-20: Energy Level Diagram of Er^{3+} Ion

Bibliographic references

[1] A. J. Freeman,R. E.& Watson, Theoretical investigation of some magnetic and spectroscopic properties of rare-earth ions. Physical Review, 127(6)(1962)2058–2075. https://doi.org/10.1103/PhysRev.127.2058

[2] Periodic table of the elements, with rare earth metals (including scandium and yttrium) circled. (2025). http://tnahistoryoftechnology.com

[3] L. Smentek, Theoretical description of the spectroscopic properties of rare earth ions in crystals. Physics Reports, 297(3–4)(1998)155–233. https://doi.org/10.1016/S0370-1573(97)00067-7

[4] M. H. V. Werts, Making sense of lanthanide luminescence. Science Progress, 88(2)(2005)101–131. https://doi.org/10.3184/003685005783238435

[5] J. F. He et al., Application of rare earth elements in dual-modality molecular probes. RSC Advances, 14(32)(2024)18519–18532. https://doi.org/10.1039/D4RA02224J

[6] B. G. Wybourne, Spectroscopic properties of rare earths. Interscience Publishers, 1965.

[7] G. H. Dieke, Spectra and energy levels of rare earth ions in crystals. Interscience Publishers, 1968.

[8] G. H. Dieke & H. M. Crosswhite, The spectra and energy levels of rare earth ions in crystals. Applied Optics, 2(7)(1963)675–686. https://doi.org/10.1364/AO.2.000675

[9] L. A. Riseberg & M. J. Weber, Relaxation phenomena in rare earth luminescence. In E. Wolf (Ed.), Progress in Optics, vol. 14, pp. 1–95. North-Holland Publishing Company, 1976.

[10] A. A. Kaminskii, Laser Crystals, Their Physics and Properties. Springer-Verlag, Berlin, 1990.

[11] A. A. Kaminskii, Crystalline Lasers. CRC Press, 2000.

[12] B. M. Walsh, B. Di Bartolo, & O. Forte (Eds.), Advances in spectroscopy for lasers and sensing. Springer, 2006.

[13] E. U. Condon & G. H. Shortley, The Theory of Atomic Spectra. Cambridge University Press, 1959.

[14] J. H. Van Vleck, The puzzle of rare-earth spectra in solids. Journal of Physical Chemistry, 41(1)(1937)67–80. https://doi.org/10.1021/j150378a002

[15] B. R. Judd, Optical absorption intensities of rare-earth ions. Physical Review, 127(3)(1962)750–761. https://doi.org/10.1103/PhysRev.127.750

[16] G. S. Ofelt, Intensities of crystal spectra of rare-earth ions. The Journal of Chemical Physics, 37(3)(1962)511–520. https://doi.org/10.1063/1.1701366

[17] A. Cheddadi, Optical spectroscopic study of absorption and emission of optical materials doped with rare earth ions for photoconversion. Doctoral dissertation, Badji Mokhtar Annaba University, 2014.

[18] S. Hufner, Optical spectra of rare earth compounds. Academic Press, 1978.

[19] S. Jellab, Étude spectroscopique des matériaux vitreux dopés par des ions de terres rares. Doctoral dissertation, Université Annaba, 2014.

[20] L. Petit, Étude des propriétés optiques des verres dopés par des ions de terres rares. Doctoral dissertation, Université Bordeaux, 2002.

[21] F. Auzel, Spectroscopy and dynamics of collective excitations in solids. In D. Bartolo (Ed.), Spectroscopy of Solids, pp. 537–556. Plenum Press, 1997.

[22] R. T. Wegh, H. Donker, K. D. Oskam, & A. Meijerink, Visible quantum cutting in $LiGdF_4:Eu^{3+}$ through downconversion. Science, 283(5402)(1999)663–666. https://doi.org/10.1126/science.283.5402.663

[23] B. Liu, Y. Chen, C. Shi, H. Tang, & Y. Tao, Visible quantum cutting in BaF_2: Gd, Eu via downconversion. Journal of Luminescence, 101(2)(2003)155–159. https://doi.org/10.1016/S0022-2313(02)00455-7

[24] C. Lorbeer, J. Cybinska, & A.-V. Mudring, Facile preparation of quantum cutting $GdF_3:Eu^{3+}$ nanoparticles from ionic liquids. Chemical Communications, 46(4)(2010)571–573. https://doi.org/10.1039/B916348A

[25] C. Lorbeer, F. Behrends, J. Cybinska, H. Eckert, & A. V. Mudring, Charge compensation in RE^{3+} (RE = Eu, Gd) and M^+ (M = Li, Na, K) co-doped alkaline earth nanofluorides obtained by microwave reaction with reactive ionic liquids leading to improved optical properties. Journal of Materials Chemistry C, 2(44)(2014)9439–9448. https://doi.org/10.1039/C4TC01486A

[26] M. L. Falin, V. A. Latypov, A. M. Leushin, G. M. Safiullin, A. A. Shakirov, & A. A. Shavelev, EPR and optical spectroscopy of Yb^{3+} ions in $LiCaAlF_6$ single crystals. Journal of Alloys and Compounds, 813(2020)152147. https://doi.org/10.1016/j.jallcom.2019.152147

[27] G. Demirkhanyan, N. Babajanyan, N. Kokanyan, M. Aillerie, M. Bazzan, et al., Spectroscopic and up-conversion properties of Yb^{3+}/Ho^{3+}-codoped $LiNbO_3$ crystals. Condensed Matter, 10(1)(2025)23. https://doi.org/10.3390/condmat10010023

[28] M. Kochanowicz, D. Dorosz, J. Żmojda, & J. Dorosz, Spectroscopic properties of Yb^{3+}/Tb^{3+} doped germanate glasses. Acta Physica Polonica A, 124(3)(2013)472–475. http://przyrbwn.icm.edu.pl/APP/PDF/124/a124z3p24.pdf

[29] B. C. Jamalaiah, K. Rama Gopal, M. V. Vijaya Kumar, & G. V. Lokeswara

Reddy, Optical properties of Yb^{3+}-doped NBSAZB glasses for IR lasers. Journal of Luminescence, 187(2017)378–382. https://doi.org/10.1016/j.jlumin.2017.03.046

[30] Y.-C. Li, Y.-H. Chang, Y.-S. Chang, Y.-J. Lin, & C.-H. Laing, Luminescence and energy transfer properties of Gd^{3+} and Tb^{3+} in $LaAlGe_2O_7$. The Journal of Physical Chemistry C, 111(28)(2007)10682–10688. https://doi.org/10.1021/jp0719107

[31] H. Boubekri, M. Diaf, K. Labbaci, L. Guerbous, T. Duvaut, & J. P. Jouart, Synthesis and optical properties of Tb^{3+} doped CdF_2 single crystals. Journal of Alloys and Compounds, 575(2013)339–343. https://doi.org/10.1016/j.jallcom.2013.05.189

[32] W. T. Carnall, P. R. Fields, & K. Rajnak, Electronic energy levels in the trivalent lanthanide aquo ions. I. Pr^{3+}, Nd^{3+}, Pm^{3+}, Sm^{3+}, Dy^{3+}, Ho^{3+}, Er^{3+}, and Tm^{3+}. The Journal of Chemical Physics, 49(10)(1968)4424–4442. https://doi.org/10.1063/1.1669893

[33] S. Rai & S. Hazarika, Fluorescence dynamics of Tb^{3+} and Tb^{3+}/Ho^{3+} doped phosphate glasses. Optical Materials, 30(9)(2008)1343–1348. https://doi.org/10.1016/j.optmat.2007.06.016

[34] M. J. Weber, Relaxation processes for excited states of Eu^{3+} in LaF_3. Physical Review, 157(2)(1967)262–272. https://doi.org/10.1103/PhysRev.157.262

[35] H. A. Kramers, Théorie générale de la rotation paramagnétique dans les cristaux. Proceedings of the Amsterdam Academy, 33(1930)959–972.

[36] A. A. Kaplyanskii & R. M. McFarlane (Eds.), Modern problems in condensed matter sciences, vol. 21. North-Holland, 1987.

[37] A. A. Kaminskii, Crystalline lasers: Physical processes and operating schemes. CRC Press, 1996.

[38] F. Auzel, Coherent emission in rare earth materials. In K. A. Gschneidner, Jr. & L. Eyring (Eds.), Handbook on the Physics and Chemistry of Rare Earths, vol. 22, ch. 151, pp. 507–560. Elsevier, 1996.

[39] M. F. Joubert, Photon avalanche upconversion in rare earth ion materials. Optical Materials, 11(2-3)(1999)181–203. https://doi.org/10.1016/S0925-3467(98)00043-3

Chapter II: Glasses

Introduction

For thousands of years, glass has been an integral part of our daily lives, from simple windows to advanced technologies in communications and medicine. Today, glass, alongside ceramics, is classified within the family of amorphous or non-crystalline materials, which are characterized by a disordered atomic arrangement, unlike crystalline materials.

Amorphous materials are not a recent discovery; iron-rich glassy materials found on the surface of the moon date back billions of years, and humans have been producing glass, primarily based on silica, for millennia. What is new, however, is the tremendous surge in scientific research on glassy materials in recent decades, and the growing interest in developing new materials capable of adopting a glassy structure.

In this chapter, we will briefly review the history of glass and attempt to establish a precise definition of it. We shall examine the phenomenon of glass transition and categorize several varieties of glass.

II-1. History

Obsidian is the oldest natural volcanic glass used for making tools, cutting weapons, and jewelry. The first manufactured glasses originated in Mesopotamia around 4500 years before Christ [1], and it was by chance that humans discovered the spontaneous formation of glass. Then, with the mastery of the art of forming this material, the first objects were initially precious ornaments or containers. In Syria and Egypt 3000 years before Christ, the glasses found are opaque, green or blue in color, and it is now known, through an analysis of the cuneiform tablets from the library of King Ashurbanipal, that it was the Egyptians who manufactured soda glasses and held this monopoly. In 1500 B.C., glass became translucent thanks to the highest temperature furnace of that era, and hollow glass pieces appeared, shaped by the technique known as "core-formed" as well as enamel. The art of glassmaking completely shifted in the first century B.C. with the discovery of the blowpipe in Syria. This technique successively spread from Italy to Gaul and then to Spain. At the same time, transparent glass was invented in Sidon (Phoenicia) due to the purity of the sands and the presence of natron. The 1st century saw the birth of a strong hollow glass industry. From the 15th century, the Venetian glassworks (Murano) managed to eliminate the coloring elements through leaching and obtained a clear glass, the

cristallo, which ensured Venice's dominance in the glass market for two centuries. And then it was the Germans, in the region of Bohemia, who created at the end of the 15th century a new, thicker, and harder glass, based on Venetian glass, known as Bohemian crystal. In 1676, the English chemist George Ravenscroft invented crystal glass, whose brilliance is due to a high percentage of lead.

In the 18th century, technology evolved rapidly, and the first molds appeared in 1821, ending the blowing of glass for bottles and cups. The technology of flat glass improved in the following century; And so, controlled quantities of compressed air were sent to produce a large, regular cylinder, which was then cut lengthwise, reheated, and laid down to let it flatten out. The price of glass dropped, and it became commonplace in every home. At the same time, companies in France (Saint-Gobain), Belgium, and Germany monopolized the production of glass plates until the creation of the first American factory (Pittsburgh Plate Glass Company) in 1833.

In 1920, Turner from the University of Sheffield developed systematic measurements of the physical properties of various glasses, which advanced the scientific method in glass research. Thus, the notion of glass became generalized to refer to any non-crystalline solid, rather than just oxide glass. Ten years later, Tamman's work [2] is focused on the general understanding of the vitreous state considered as a state of matter aggregation. All recent progress has emerged thanks to a better physico-chemical understanding of glass, but even more so due to the use of glass in optics, whose development led to the introduction of new components into the composition. But it was after the Second World War that scientific research and glass technology came together to foster the flourishing of true glass science during the period 1950-1960 [3], when all modern physico-chemical methods were applied to the study of glass.

II-2. Definition of a glass

The term glass can have different interpretations. In everyday language, this term is often used to describe a material that is both fragile and transparent. In scientific terminology, the term "glass" covers a very broad spectrum, which makes its definition complex. The definition of glass can be approached in two ways:

According to the traditional definition by R. Haas [4], "glass is a supercooled liquid that has solidified." According to this definition, we end up neglecting an entire category of glasses that were never made from a liquid.

According to the ASTM (American Society for Testing Materials) definition [5], glass is described as: "an inorganic product that has been cooled after fusion under rigorous conditions, while preventing crystallization." According to the definition by ASTM (American Society for Testing Materials) [5], glass is described as: "an inorganic product that has been cooled after fusion under rigorous conditions, while preventing crystallization." This fundamentally means the same thing as the previous definition, as it does not take into account polymer glasses. It is therefore evident that a universal definition of glass cannot be established through the different manufacturing methods.
Another definition of glass is: a solid material that lacks long-range order. In other words, the arrangement does not exceed two to three times the dimensions of the glass's elementary structure. This definition is validated by experiments, whether through X-ray diffraction or transmission electron microscopy (TEM). However, it remains arbitrary as it is linked to the dimension of the base pattern [6].
As another option: "glass is a collection of tetrahedra sharing common vertices and lacking long-range order." This statement perfectly illustrates the idea of the glass network, and it is re levant for certain oxide glasses, particularly silicates [7].
The last option defines glass as "a non-crystalline solid that exhibits the glass transition," the physical state associated with this is called the glassy state. This definition imposes no constraints on how to obtain the vitreous material [3].

II-3. The glass transition

The conventional method for making glass involves rapidly cooling a molten material so that it solidifies before crystals can form. The thermal characteristics of glass are typically described by tracking changes in thermodynamic properties such as specific volume or enthalpy as the temperature varies.
During cooling, a liquid can reach a temperature below its melting point (T_m) and exist in a metastable supercooled state. For some substances, this supercooled state can persist over a wide temperature range. This phenomenon is particularly important in the study of glass-forming materials, as it highlights the delicate balance between kinetic and thermodynamic factors that govern the formation of amorphous solids.

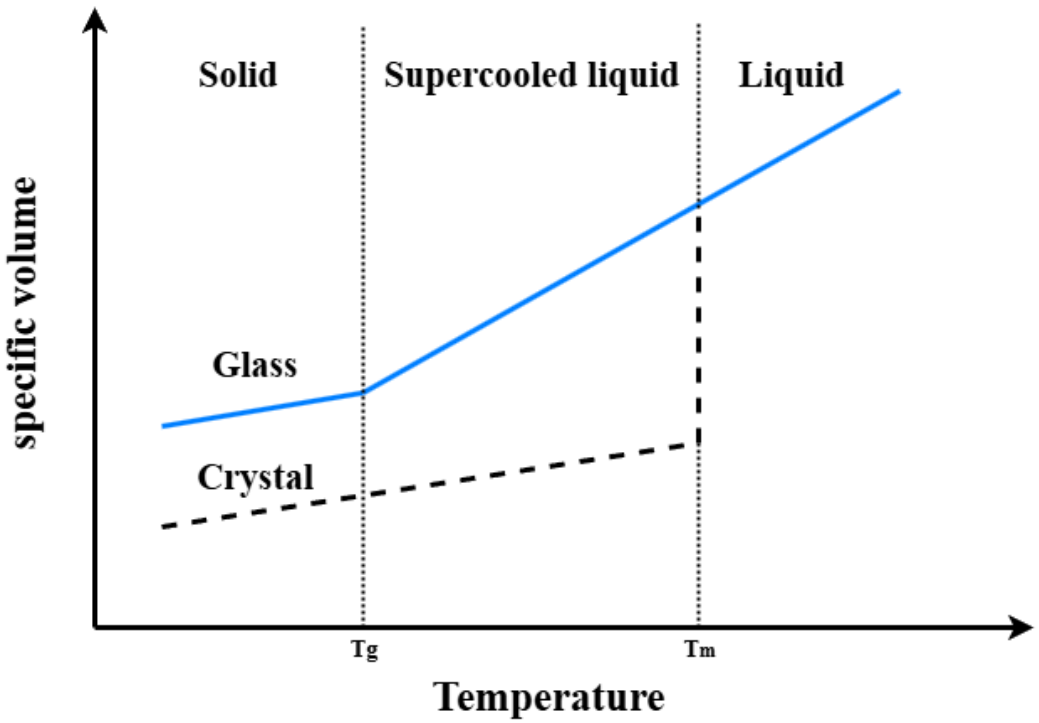


Figure II-1: Variation of the specific volume of glass and crystal as a function of temperature

When cooling from the high-temperature liquid phase, the molar volume V_M (or enthalpy H) decreases as the temperature decreases. If the liquid is kept below the melting point for a sufficiently long time, it transforms into a crystal with a much lower molar volume (or enthalpy) than that of the corresponding supercooled liquid. On the other hand, if the temperature drops quickly and continuously from a steady liquid state to very low temperatures, the liquid stays in a supercooled state. It is this metastable state that will gradually become rigid, giving rise to glass at room temperature. The continuous transition from supercooled liquid to glass is known as the transition domain.

This transformation is not a first-order phase transition like crystallization, but rather a gradual change in the material's structure and dynamics. As the viscosity of the supercooled liquid increases dramatically with decreasing temperature, the molecular motions slow down until the structure becomes essentially "frozen" in a disordered state.

The glass transition temperature T_g is practically defined as the temperature at which the extrapolated curves of the liquid and glass phases intersect. This transition spans a temperature range influenced by the nature of the glass and the cooling rate applied.

An increase in the cooling rate results in a higher temperature at which the glass transformation occurs. The opposite is true for slow cooling.

The change in the molar volume of glass as a function of temperature is continuous and almost linear. Thus, the linear coefficient of thermal expansion is nearly constant. This is one of the properties of glass. At room temperature (Figure II-1), glass has a higher molar volume than the corresponding crystal. Its open structure facilitates the diffusion of small chemical species.

The glass transition is a kinetic phenomenon rather than a thermodynamic one, meaning that the properties of the resultant glass can vary considerably based on the cooling history and the precise conditions of its formation. This underlines the diversity of glassy materials and the wide range of properties they can exhibit.

II-4. The major families of glasses

II-4-1. Oxide glasses

The oxides SiO_2, GeO_2, B_2O_3, P_2O_5, and As_2O_3 have the ability to create glasses, either individually or in combination with one or more other oxides. They are generally referred to as traditional glasses. These glasses represent the largest category of industrial glasses. They stand out for their remarkable thermomechanical properties and solid chemical durability. In optics, silica glasses are preferred for their exceptional purity and high-temperature resistance. However, they exhibit a limited transparency range in the infrared, extending only up to 3 μm.

II-4-2. Metallic glasses

The first metallic alloys, whose amorphous nature was confirmed by X-ray diffraction, were produced in thin layers, either through vapor condensation, chemical deposition, or electrodeposition. It was not until 1960 that the first production of glassy metal by liquid quenching was reported [8], and it was a Gold-Silicon alloy.

Metallic glasses are usually produced by an ultra-rapid quenching process that gives rise to ribbons or wires. The first bulk metallic glasses (Bulk Metallic Glasses) were developed in 1990, using La-Mg-Zr [9,10]. The first glassy composition based on iron, named Fe-Al-Ga-P-C-B [11], appeared in 1995.To ensure the stability of the supercooled metallic melt, three empirical rules must be followed [12,13]:

It is necessary to have systems with multiple components (at least three).
It is necessary that there is a notable difference between the atomic radii of the main

components (more than 12%). In the mixture, the elements should exhibit a negative heat.

Metallic glasses show short-range order, a scale that is significant for the analysis of metal-metalloid systems. However, a medium-range order (MRO) is present in most other situations. It is possible to describe this order scale (MRO) using polyhedral structural units. To organize themselves in three dimensions, they can connect through their: edges, faces, or vertices [14,15].

II-4-3. Halide glasses

Glasses made of halides (fluorides, chlorides, bromides, iodides) have a greater transmission capacity in the infrared range compared to oxide glasses. This spectral transparency limit is conditioned by the molecular vibration energies of the lattice. By substituting oxygen with heavier elements such as fluorine, chlorine, bromine, or iodine. In the majority of cases, halide glasses exhibit chemical instability. Only fluoride glasses possess satisfactory mechanical and chemical characteristics, such as resistance to fracture and thermal shock. Fluoride glasses, especially those based on ZBLAN (ZrF_4-BaF_2-LaF_3-AlF_3-NaF), are widely used in the fabrication of infrared optical fibers due to their low optical losses and relatively good mechanical stability [16]. These fibers are essential in applications like infrared spectroscopy, medical lasers, and thermal imaging, where transmission in the mid-infrared range is required. In contrast, other halide glasses (chlorides, bromides, iodides) are generally less stable and more sensitive to moisture, which limits their practical applications.
In the following section, particular attention will be given to fluoride and chloride glasses, with a detailed discussion of their specific properties and advantages.

- **Fluorinated glasses**

Fluorides represent a unique category of glassy materials due to their structure, which distinguishes them as non-tetrahedral mineral glasses, and thanks to their low phonon energy, which gives them exceptional optical characteristics. The low refractive index of fluorine is due to its reduced polarizability. Rare earths can be hosted in fluorinated glass matrices due to the ionic nature of the metal-fluorine bond. Indeed, interesting characteristics associated with energy levels are observed, such as fairly intense radiative transitions and prolonged lifetimes of excited levels in the context of doping fluorinated glasses with rare earth elements.

Optical systems greatly benefit from the use of fluorinated glasses. They exhibit much greater transparency than silica in the mid-infrared [17]. They have a transmission range that extends up to 6-7µm. Thanks to their low phonon energy, which is approximately 500 to 600 cm-1, they are excellent candidates for the implementation of an amplifier. Their theoretical minimum attenuation is also significantly lower than that of silica, which would allow for theoretical losses of around 0.05 dB/Km at 2.5-3µm.

The fluorinated glasses, known for a long time, trace their origin to BeF2 [18] (Goldschmidt, 1927). They are referred to as equivalents of silica. Their use has been restricted due to the toxicity of beryllium fluoride, as well as their ability to absorb moisture.

Heyne [19] was subsequently the pioneer in reporting the existence of beryllium fluoride glasses, resulting from the combination of BeF2 with alkali and alkaline earth fluorides. It was around 1945 that K.H. SUN [20] began to systematically study and develop these glasses, which led him to describe new compounds of aluminum, lead, and alkaline earth metal fluorides.

These studies were taken up by other authors who confirmed that replacing beryllium with aluminum tends to reduce issues related to moisture resistance and toxicity.

- **Chloride glasses**

Chloride glass, primarily based on $ZnCl_2$, which is the most widespread among chloride glasses [21], produces a tetrahedral glass similar to silica glass. More recent research [22] has shown that the configuration of vitreous $ZnCl_2$ can be represented by a compact disordered arrangement of Cl spheres, which associate with Zn^{2+} ions to form distorted tetrahedral ($ZnCl_4^{-2}$). These tetrahedra share the vertices, and the Zn-Cl bonds exhibit a covalent character. Chloride glasses were obtained in the ternary system $ThCl_4$-NaCl-KCl [23], which exhibit a structural analogy with fluorozirconate glasses. We also proceeded with the synthesis of other ternaries based on $CdCl_2$ ($CdCl_2$-$BaCl_2$-NaCl). These glasses have limited hygroscopicity and stability. They have little practical interest. However, the most stable compositions in $CdCl_2$ are generally obtained by combining fluorides and chlorides within polyhalogenated systems [24]. These constitute a new category of glasses potentially attractive for infrared transmission and for low-loss optical fibers.

Recent research [25, 26] has demonstrated the presence of stable systems, confirming the ability to vitrify cadmium polyhalides. In these devices, the integration of Pb has contributed to enhancing their chemical stability [25].

In order to expand infrared transparency, research has been conducted to discover chlorofluorinated compositions containing Cd [27, 28]. These studies demonstrate that the corrosion of glasses is sensitive to the presence of chloride ions. The process of water contamination occurs through an ion exchange between Cl- and OH- at the glass surface, which is then followed by the propagation of hydroxyl groups inside the glass.

II-4-4. Chalcogenide glasses

These oxygen-free glasses are based on elements from group VI (S, Se, Te). These components transform into glasses when combined with one or more elements from groups III (Ga, In), IV (Ge, Si), V (Sb, As), or VII (F, Cl, Br, or I). The emergence of these glasses, referred to as "chalcogenide glasses," dates back to the early 1950 s [29, 30]. A variety of glass systems made up of chalcogen elements are presently recognized, including: As-S, Ge-S, As-Se, Ge-Se, Ge-As-Se, GePS, La-Ga-Ge-Se, Ge-Sb-Se, Ge-Se-Te, As-Ge-Se-Te, and As-Se-Te. These substances demonstrate weaker bonds compared to those found in oxides, which can contain both homopolar and heteropolar bonds concurrently.

The electronic configuration of chalcogen elements is $s^2 p^4$, where two p electrons are capable of forming bonds with two neighbors.

The valence band groups the unpaired p electrons, while the conduction band encompasses the anti-bonding states of the covalent bonds. These glasses, incorporating heavier components such as sulfur (S), selenium (Se), and tellurium (Te), exhibit a higher density than oxidized glasses. The coordination number, bond forces, and bond angles exhibit a short-range ordered structure (up to the second nearest neighbor), similar to the corresponding crystal. However, the medium-range structure is subject to controversy: one can consider a distorted quasi-crystalline structure or a Continuous Random Network Structure.

One of the main interests in working with chalcogenide glasses is their ability to be transparent in the infrared (IR) range [29, 31, 32]. Applications in this sector can be classified into two types: active optics and passive optics.

In the field of active optics, chalcogenide glasses, thanks to their low phonon energy which allows for a significant quantum yield for rare earths, are relevant for use as

optical amplifiers [33]. Moreover, their high nonlinear refractive index (approximately 500 times that of silica) demonstrates their significant potential in nonlinear optics [34]. Passive applications, on the other hand, are associated with the remarkable transparency of these materials in the near-infrared (NIR), such as for the manufacture of lenses intended for night vision cameras, planar waveguides for integrated optics [35], or even infrared sensors [36, 37].

II-4-5. Oxyfluoride glasses

Oxyfluoride glasses constitute a hybrid class of amorphous materials combining characteristics of fluoride glasses and oxide glasses. Introduced as subjects of in-depth study starting in the 1970s, particularly after the discovery of ZrF_4-based glasses by Poulain [38], these glasses have garnered increasing interest for their unique optical properties and their potential in photonics, optical fibers, lasers, and even quantum electronics. Unlike purely fluorinated glasses, which have a low phonon energy favorable to luminescence, oxyfluoride glasses benefit from better chemical and thermal stability due to the presence of oxygen, while maintaining good transparency in the UV and IR [38–41].

The controlled introduction of oxygen into fluorinated matrices, or conversely of fluorine into oxide matrices, modifies the connectivity of the vitreous network while affecting the crystallization rate. It has been demonstrated that certain oxides such as P_2O_5, TeO_2, MoO_3, or GeO_2 play a stabilizing role in the glassy state, despite the potential volatilization of certain compounds like SiF_4 or GeF_4 [40]. This makes these materials suitable for controlled thermal treatments for the formation of glass-ceramics, where phases like β-PbF_2 can be locally crystallized to enhance the luminescence of rare earth ions. From a performance perspective, oxyfluoride glasses can host high concentrations of luminescent ions (up to > 60 mol%), far exceeding those of conventional oxide matrices (limited to ~30 mol%) [42, 43]. This leads to an increase in the refractive index, an improvement in quantum efficiency, and effects such as upconversion, which are essential for optical thermal sensors and stimulated emission lasers [44]. Moreover, their extended transparency (from near-UV to mid-infrared) and their potential for transformation into photonic glass-ceramics make them multifunctional materials for advanced devices.

- **Importance of oxyfluoride glasses for up-conversion applications**

Oxyfluoride glasses are particularly attractive matrices for up-conversion applications due to their ability to combine the low phonon energy of fluoride glasses with the superior chemical and thermal stability of oxide glasses. This unique balance allows efficient radiative transitions of rare earth ions while minimizing non-radiative losses. In addition, the homogeneous distribution of dopant ions and the possibility of controlled crystallization into transparent glass-ceramics provide an effective route to enhance up-conversion efficiency. These advantages make oxyfluoride glasses promising candidates for advanced photonic devices, which motivates their selection in the present work.

II-5. Properties of glasses

One of the most adaptable materials in terms of composition and structure is glass, whose physical and chemical characteristics may be greatly adjusted by carefully regulating its primary ingredients and manufacturing conditions. Its amorphous structure, in which the atoms lack long-range periodic order, gives it this flexibility and gives it isotropy and distinctive behavior in mechanical and optical settings. High transparency in a wide spectral range, from ultraviolet to near-infrared, is one of glass's most notable qualities. This makes it essential for applications like advanced photonic components, high-performance windows, and optical fibers. Furthermore, glass is easily shaped and its chemical composition can be altered to create materials with specific qualities, like improved chemical resistance or advanced optical characteristics, by adding different oxides, fluorides, or even transition metal and rare-earth ions. As our understanding of glass's structure and processing continues to grow, glass's variety of applications has expanded significantly, making it a crucial material in many industries and scientific advancements. In the following, we will briefly highlight the main thermal and optical properties that distinguish glass from other materials.

- **Optical properties**

The refractive index, along with the related concepts of transmission and reflection, represents the most common optical properties. When absorption, scattering, and

dispersion of light are taken into account, it is evident that the optical properties of glasses are fundamentally rooted in the interaction between the material and the energy of electromagnetic waves.

The most recognized property of glass is, in fact, an optical one-namely, its ability to transmit light.

The exceptional transparency of glass over a wide spectral range, from ultraviolet to near-infrared, is mainly attributed to its amorphous structure and the absence of micron-sized defects, which minimizes light scattering and maximizes optical transmission. This property makes glass indispensable in the manufacturing of optical fibers, optical windows, and modern photonic components [45].

Adjusting the chemical composition of glass allows for the modulation of its optical properties. For example, the incorporation of specific oxides or fluorides influences transparency, corrosion resistance, and refractive index, which is crucial for adapting the material to advanced applications. The addition of transition metal or rare earth ions (such as Nd^{3+}, Er^{3+}, Tm^{3+}) into the glass matrix introduces specific absorption and emission bands, resulting from electronic transitions within these ions. This characteristic allows for the production of colored or luminescent glasses, used in lasers, optical amplifiers, and photoluminescence devices [46]. In doped glasses, the random distribution of rare earth ions in the amorphous matrix causes an inhomogeneous broadening of the spectral bands, which is particularly advantageous for applications requiring wide absorption and emission bands, such as tunable lasers or ultrafast pulse devices. Moreover, the vitreous matrix allows for a homogeneous and stable incorporation of dopant ions, without segregation or precipitation, unlike what can be observed in crystalline matrices [47]. To get the best optical performance, especially in telecommunications optical cables and next-generation photonic devices, the glass must be chemically pure, the melting process must be carefully controlled, and the structure must be free of flaws [48].

- **Applications of up-conversion**

Up-conversion is a nonlinear optical process in which the sequential absorption of two or more low-energy photons results in the emission of a single photon with higher

energy. This phenomenon is particularly efficient in rare-earth-doped glasses with low phonon energy, such as fluoride, oxyfluoride, and chalcogenide glasses.

Up-conversion materials find important applications in solid-state lasers and optical amplifiers, where they enable frequency conversion from infrared to visible or near-infrared wavelengths. They are also widely used in infrared detectors, temperature sensors, and optical thermometry, owing to the strong temperature dependence of up-conversion emission intensities.

In recent years, up-conversion glasses have attracted significant interest in biomedical imaging and security marking, due to their ability to produce visible emission under infrared excitation, which minimizes background fluorescence and improves signal-to-noise ratios. Furthermore, up-conversion processes are exploited in photovoltaics to enhance solar cell efficiency by converting sub-bandgap infrared photons into usable visible light.

a) Transmission of light

It is defined by the factor:

$$T = I/I_0 \qquad \text{(Eq. II-1)}$$

I_0 represents the intensity of the incident light, while I denotes the intensity captured after passing through the material [49].

The Beer-Lambert law [50], which describes the absorption of light, states that the intensity of electromagnetic radiation passing through a material is exponentially reduced based on the thickness and concentration of the absorbing species:

$$I\ (\lambda, X) = I_0\ (\lambda).e^{-\alpha x} \qquad \text{(Eq. II-2)}$$

I_0 : is the intensity of the incident light.
I : is the intensity of the outgoing light.
α : is the absorption coefficient
X : is the optical path length.
Indeed, the commonly used glasses transmit visible light ($400 \leq \lambda \leq 700$ nm). This same structure is the source of this transparency.

b) Refractive index and dispersion

The refractive index is equal to the ratio of the speed C of light in a vacuum to that $\boldsymbol{v}$ in the material:

$$n = \frac{C}{v} \qquad \text{(Eq. II-3)}$$

In a vacuum, light propagates at a constant speed regardless of its wavelength, but this proposition is not necessarily valid in all other media. Therefore, the refractive index depends on the wavelength and, commonly, it decreases as the wavelength λ increases. This variation is referred to as dispersion, a concept defined by relation [51].

$$D = \frac{dn}{d\lambda} \qquad \text{(Eq. II-4)}$$

c) Refractive index of a composite glass

The determination of the refractive index of a composite glass is done by considering each component individually, given that the influence of each element is additive.

Huggins, Sun, and Davis established the link between density and refractive index, this index being described by the following formula:

$$n_s = 1 + \left(\frac{\sum \alpha_M N_M}{V}\right) \qquad \text{(Eq. II-5)}$$

Where

n_s : Refractive index

α_M : Refractive index of the species M.

N_M: Number of m ions per oxygen atom (glass compounds being of the form Mm ON).

V: volume occupied by the oxygen atoms.

The atomic radius of oxygen exceeds that of cations, indicating that the volume of the glass corresponds to the volume occupied by the oxygen atoms. The refractive index is higher because the polarizability is greater, and the molar volume is lower (denser structure) [52].

➢ Thermal Properties

Temperature variations are directly associated with the thermal characteristics of glasses. We generally examine three characteristics:

a) Specific heat (C_P)

This measurement quantifies the amount of thermal energy required to change the temperature of a unit mass of an object. At room temperature, the C_P values for glasses are around $4.54x10^{-2}$ Joule $g^{-1}deg^{-1}$ [53].

b) Thermal conductivity (K)

In glasses, heat transfer can occur by conduction or by radiation. At low temperatures, the first process dominates, while at high temperatures, the second one does. Conductivity (also called thermal conductivity) is the ability to dissipate thermal energy. It defines the relationship between the thermal flux per unit area and the temperature variation.

Generally, the thermal conductivity of glasses is quite low, around 0.8 $w.m^{-1}.K^{-1}$ for oxide glasses and 0.5 $w.m^{-1}.K^{-1}$ for fluoride glasses [54]. In a glass, the absence of phonons and thus long-range order makes it difficult for the lattice vibrations to disperse, and the heat dissipation is inefficient, which can lead to the degradation of the glasses [55].

c) The coefficient of thermal expansion (α)

Such a coefficient indicates the thermal energy constraint. It is also the ratio established between the elongation and the increase in temperature over a unit length. When this coefficient increases, the resistance to thermal shock decreases. The coefficient of glass ranges between 1.10^{-6} and 20.10^{-6} K^{-1} [56].

Bibliographic references

[1] R. W. Douglas & S. Frank, *A history of glassmaking*, Foulis Co. (1972).

[2] G. Tammann, *Der Glaszustand*, Voss (1933).

[3] J. Zarzycki, *Les verres et l'état vitreux*, Masson (1982).

[4] R. Haase, *Termodynamik der Mischphasen*, Springer (1956).

[5] H. Scholze, *Le verre: Nature, structure et propriété*, 2nd ed., Institut du Verre (1980).

[6] B. G. Wybourne, *Spectroscopic properties of rare earths*, Interscience Publishers (1965).

[7] C. B. Carter & M. G. Norton, *Ceramic materials science and engineering*, Springer (2007).

[8] W. Klement, R. H. Willens & P. Duwez, Non-crystalline structure in solidified gold–silicon alloys, *Nature*, 187 (1960) 869–870.

[9] S. Aashamd *et al.*, *J. Non-Cryst. Solids*, 213–214 (1997) 341–344.

[10] A. Peker & W. L. Johnson, A highly processable metallic glass: $Zr_{41.2}Ti_{13.8}Cu_{12.5}Ni_{10.0}Be_{22.5}$, *Appl. Phys. Lett.*, 63(17) (1993) 2342–2344.

[11] A. Inoue, T. Y. Shinohara & J. S. Gook, *Mater. Trans. JIM*, 36(12) (1995) 1427–1433.

[12] A. Inoue, *Mater. Trans. JIM*, 36(7) (1995) 866–875.

[13] A. Inoue, *Mater. Sci. Eng. A*, 304–306 (2001) 1–10.

[14] D. B. Miracle, The efficient cluster packing model—An atomic structural model for metallic glasses, *Nat. Mater.*, 3(10) (2004) 697–702.

[15] H. W. Sheng *et al.*, Atomic packing and short-to-medium-range order in metallic glasses, *Nature*, 439 (2006) 419–425.

[16] V. Trnovcová, R. M. Zakalyukin, N. I. Sorokin, D. Ležal, P. P. Fedorov, E. Illeková, A. Škubla & M. Kadlečíková, Physical properties of fluoride glasses for ionics, *Mater. Sci. Forum*, 480–481 (2005) 299–304. https://doi.org/10.4028/www.scientific.net/MSF.480-481.299

[17] S. Hüfner, *Optical spectra of rare earth compounds*, Academic Press (1978).

[18] H. Rawson, *Glass*, Vol. 2, Academic Press (1967).

[19] G. Heyne, The preparation and properties of some beryllium fluoride glasses, *Angew. Chem.*, 46 (1933) 473–477.

[20] K. H. Sun, *Fluoride glass*, U.S. Patent 2,466,509 (1949).

[21] H. Rawson, *Inorganic glass-forming systems*, Academic Press, New York (1976).

[22] J. A. E. Desa, A. C. Wright, J. Wong & R. N. Sinclair, *J. Non-Cryst. Solids*, 51(1) (1982) 57–86.

[23] H. Hu & J. D. Mackenzie, *J. Non-Cryst. Solids*, 51(2) (1982) 269–272.

[24] M. Matecki & M. Poulain, *J. Non-Cryst. Solids*, 56(1–3) (1983) 81–86.

[25] M. Matecki & M. Poulain, *Mater. Sci. Forum*, 32–33 (1988) 167–172.

[26] A. Jha & J. M. Parker, *Phys. Chem. Glasses*, 32(1) (1991) 1–12.

[27] M. Matecki & M. Poulain, *J. Non-Cryst. Solids*, 140(1–3) (1992) 82–86.

[28] J. L. Adam, C. Ricordel & B. Boulard, *Eur. J. Solid State Inorg. Chem.*, 35(6–7) (1998) 509–518.

[29] A. R. Hilton, *Appl. Opt.*, 5(12) (1966) 1877.

[30] J. A. Savage & S. Nielsen, *Infrared Phys.*, 5(4) (1965) 195.

[31] R. K. Watts, M. de Wit & W. C. Holton, *Appl. Opt.*, 13 (1974) 2329–2932.

[32] J. Zarzycki, *Mater. Sci. Technol.*, 9 (1991).

[33] V. Nazabal, P. Nemeč, J. Jedelský, C. Duverger, J. Le Person, J. L. Adam & M. Frumar, *Opt. Mater.*, 29 (2006) 273–278.

[34] Q. Liu, X. Zhao, K. Tanaka, A. Narazaki, K. Hirao & F. Gan, *Opt. Commun.*, 198 (2001) 187.

[35] V. Balan, *Verres chalcogénures pour l'optique intégrée*, PhD Thesis, Université de Montpellier II (2003).

[36] J. Keirsse, *Mise au point d'un biocapteur...*, PhD Thesis, Université de Rennes 1 (2003).

[37] K. Michel, *Capteur optique à fibre infrarouge...*, PhD Thesis, Université de Rennes 1 (2003).

[38] I. D. Aggarawal & G. Lu (Eds.), *Fluoride glass fiber optics*, Academic (1991).

[39] J. Lucas, Review of fluoride glasses, *J. Mater. Sci.*, 24(1) (1989) 1–13.

[40] R. ElMallawany *et al.*, Some physical properties of new oxyfluoride glasses, *J. Non-Cryst. Solids*, 184 (1995) 141–146.

[41] J. L. Adam, Fluoride glass research in France, *J. Fluorine Chem.*, 107 (2001) 265–270.

[42] Y. Rault, J. L. Adam, F. Smektala & J. Lucas, *J. Fluorine Chem.*, 110 (2001) 165–173.

[43] S. Yonezawa *et al.*, *J. Fluorine Chem.*, 128 (2007) 438–447.

[44] S. Nishibu, S. Yonezawa & M. Takashima, *J. Non-Cryst. Solids*, 351 (2005) 1239–1245.

[45] Y. Yang *et al.*, Progress in oxyfluoride glass and glass-ceramics for photonic devices, *Mater. Today Phys.*, 35 (2024) 101234. https://doi.org/10.1016/j.mtphys.2024.101234

[46] X. Yan *et al.*, Broadband emission in rare-earth-doped glasses: mechanisms and applications, *Opt. Mater. Express*, 12(6) (2022) 2345–2358. https://doi.org/10.1364/OME.448051

[47] J. Yu *et al.*, *Inorg. Chem.*, 60(5) (2021) 3243–3251. https://doi.org/10.1021/acs.inorgchem.0c03503

[48] S. Zhao *et al.*, Ultra-pure glass fibers for next-generation optical communications, *Adv. Opt. Mater.*, 10(3) (2022) 2101958. https://doi.org/10.1002/adom.202101958

[49] M. Poulain & J. Lucas, *Mater. Res. Bull.*, 10(4) (1975) 243.

[50] M. J. Dejneka, *J. Non-Cryst. Solids*, 239 (1998) 149.

[51] F. Ehouma, *Structural study of phosphate-based glasses*, PhD Thesis, INP Grenoble (1994).

[52] S. Salaün *et al.*, *J. Phys.: Condens. Matter*, 5 (1993).

[53] H. Scholze, *Glass*, Institut du Verre (1974).

[54] J. Zarzycki, *Materials science and technology*, Vol. 9, VCH (1991).

[55] J. Zarzycki, *Glasses and vitreous condition*, Masson (1982).

[56] M. J. Weber, *Handbook of optical materials*, CRC Press (2003).

Chapter III: Glass synthesis and characterization techniques

Introduction

In this chapter, we present the steps involved in the preparation of a new glass matrix with the composition GeO_2-PbO-PbF_2, doped with Yb^{3+} and Tb^{3+} ions, aiming at the development of materials with enhanced optical and physical properties. This glass system was selected due to its combination of infrared transparency, high thermal stability, and improved luminescent behavior resulting from the presence of PbF_2 and its low phonon energy.

The first part of the chapter focuses on the synthesis method used in the laboratory, highlighting key procedures such as the selection of raw materials, mixing ratios, melting and quenching conditions, and factors influencing the homogeneity and transparency of the final samples.

The second part provides a brief overview of the main characterization techniques employed to study the structural, thermal, and optical properties of the materials. These include:

– X-ray diffraction (XRD), to assess the glassy nature and ensure the absence of undesired crystalline phases;

– Differential thermal analysis (DTA), to determine the glass transition temperature and thermal stability;

– Absorption and emission spectroscopy, to analyze optical transitions and the behavior of Yb^{3+} and Tb^{3+} dopants within the matrix;

– Density measurements, as an indicator of the structural quality and compactness of the glass network.

These procedures provide a comprehensive understanding of the relationship between the glass structure and its corresponding physical and optical properties, supporting the evaluation of these materials for potential applications in photonics and optoelectronics.

III-1. Synthesis of glasses

III-1-1. Composition of the glass to be developed

The pure fluorogermanate glass was developed according to the following

composition:

50% GeO_2 + 30% PbO + 20% PbF_2 hereafter referred to as GPF glass.

a) Physical properties of the studied glass

The physical properties of this glass identified from the literature are presented in Table III-1.

Table III-1: Physical Characteristics of the Studied GPF Matrix

Characteristics	Glass GPF : $50GeO_2$-30PbO-$20PbF_2$
Structure	Amorphous
Melting temperature (°C)	1055 [1]
Crystallization temperature (°C)	415 [3]
Glass transition temperature (°C)	350 [1, 3]
Cut-off frequency (cm^{-1})	337 [1]
Refractive index	n = 1.65 [4, 5] for λ= 643.8nm
Optical transparency range (nm)	200-6000 (considered ultra transparent) [6]
Maximum phonon energy (cm^{-1})	500-600 [1]

b) Molar composition of the developed glass

G. Dantelle, in his Doctoral thesis [1], describes this chemical composition, which is characterized by its stability. It allows the production of this oxyfluoride glass, provided that the elements are weighed precisely and the thermal treatment indicated in the same reference and that of C. Bensalem [2] is followed.

This matrix is doped with rare earth ions, particularly Yb^{3+} and Tb^{3+}, in the form of rare earth trifluorides (RE) with the chemical formula RE3F3 or rare earth oxides RE2O3. In our case, we used oxides since the available fluorides come from an old stock and have certainly transformed into oxides. The glass is to be synthesized according to the following chemical reaction whose composition has been indicated in Table III-2

$$50GeO_2 + 30PbO + (20-x-y)\,PbF_2 + xYb_2O_3 + yTb_2O_3 \rightarrow GPF \qquad \text{(Eq. III-1)}$$

Table III-2: Molar compositions in % of the GPF matrix

Chemical component	GeO_2	PbO	PbF_2	Yb_2O_3	Tb_2O_3
Molar composition in %	50	30	15	x = 4	y = 1

III-1-2. Synthesis Process

a) Weighing of the different constituents according to the concentration of the dopants

The first step of the synthesis protocol involves selecting components of exceptional purity, at least 2N as indicated in Table III-3, and then weighing them using an ultra-precise balance, from the METTLER brand, capable of measuring up to the thousandth of a gram.

Table III-3 below describes the purity of the powders composing the glass

Initial powder	Purity	Manufacturer
GeO_2	99.999 (5N)	Aldrich
PbO	99.99 (2N)	Penox
PbF_2	99.999 (4N)	Hegeer
Yb_2O_3	99.999 (5N)	Heeger
Tb_2O_3	99.999 (5N)	Funcmater

From the mixture of reagents in stoichiometric proportions defined by reaction (III-1), the glass samples were prepared. A charge of 5 g was used in the crucible, while the masses of the components of the GPF glass co-doped with Yb^{3+} and Tb^{3+} are detailed in Table III-4.

Table III-4: Weights of the different chemical components of GPF glass co-doped with Yb_2O_3 (4% mol) and Tb_2O_3 (1% mol)

Matrix	50%GeO_2 +30%PbO+15%PbF_2 +4% Yb_2O_3 +1%Tb_2O_3				
Chemical components	GeO_2	PbO	PbF_2	Yb_2O_3	Tb_2O_3
% molar	50	30	20-x-y=5	x = 4	y = 1
Molar masses (g/mol)	104.6088	223.1994	245.1968064	394.1062	365.84890
n (mol)	0,2997	0,3816	0,2096	0,08984	0,02085
m (g) weighed	1,4985	1,908	1,048	0,4492	0.10425

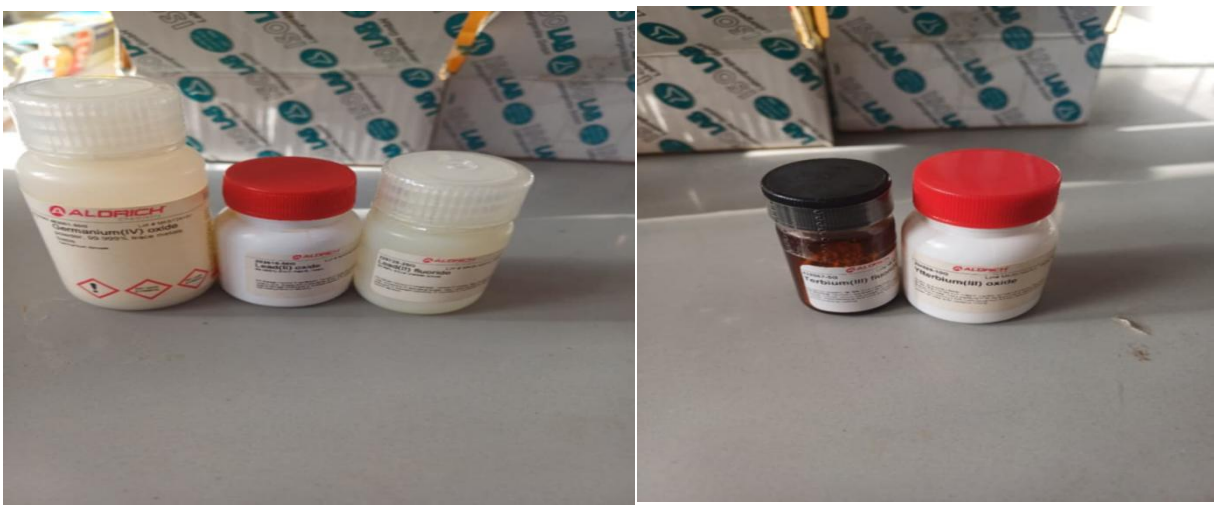


Figure III-1: Powders used in the experiment

b) Description of the crucible

We used a porcelain crucible from ISOLAB (Figure III.2). This crucible is manufactured from high-purity raw materials and is distinguished by its consistent quality, rigid structure, and impermeability to gases. The material is characterized by remarkable mechanical and chemical strength, as well as high resistance to acids and thermal shock, allowing it to withstand extreme conditions without breaking, exploding, or deforming. It supports temperatures reaching 1200 °C, with chemical compatibility surpassing that of glass



Figure III-2: Photograph of a porcelain crucible (high form) without a lid Used in the synthesis step

c) Grinding and mixing of powders

The starting materials, carefully weighed, are finely ground and mixed in an agate mortar, then transferred to the crucible before it is placed in the Nabertherm synthesis furnace (Figure III-3)



Figure III-3: Photograph of the agate mortar used for grinding, the porcelain crucible, and the chamber furnace in which the crucible is placed

Once the powder mixture is placed in the porcelain crucible, we put it in the chamber of a Nabertherm muffle furnace, which can reach a temperature of 1200 °C.

d) Furnace heating program and quenching of the molten bath

We then proceed to heat the furnace according to the program presented in Figure III-4. This program consists of three sections. The first section involves reaching the melting temperature of the mixture within 15 minutes, followed by a melting stage lasting twenty minutes to ensure a well-melted and homogeneous bath

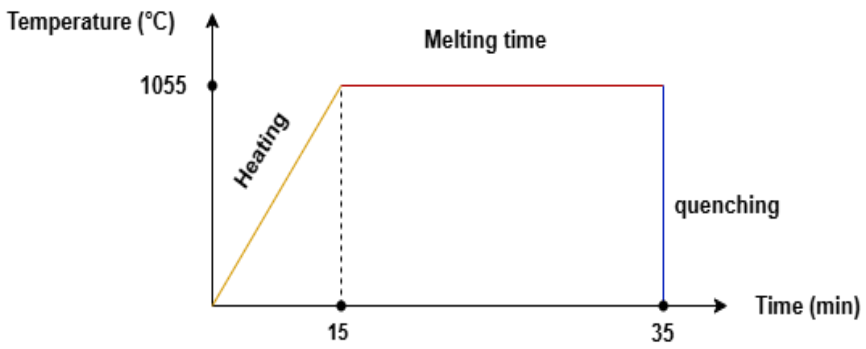


Figure III-4: Diagram of the thermal treatment to be followed during glass production GPF

This thermal protocol is based on the work of G. Dantelle and C. Bensalem [1, 2]. Subsequently, we perform a rapid and skillful pouring of the liquid (commonly referred to as quenching1) onto a steel block preheated to 150 °C in a furnace, which provides forced airflow and perfect temperature uniformity. Immediately after the quenching, we place a second steel plate, also heated to 150 °C [1], on the cast product to flatten the top of the glass "ball" that has formed. All these steps are presented in Figure III-5.



Figure III-5: Stages of glass synthesis

e) Glass solidification by annealing

Note that the obtained glass is fragile due to the internal thermal stresses caused by quenching. A solidification step for this glass is necessary through prolonged annealing at an appropriate temperature to achieve the release of these stresses. We performed an annealing at 300 °C for 2 hours in a programmable tubular furnace from the brand

Nabertherm, capable of operating between ambient temperature and 1200 °C (Figure III-6).

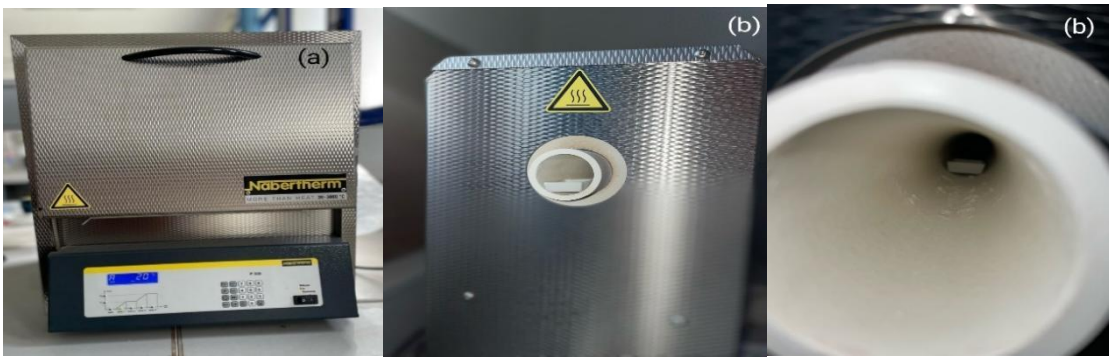


Figure III-6: (a) Photograph of the Nabertherm brand tubular furnace used for annealing, (b) Glass placed in a porcelain tray inside the tubular furnace heated to 300°C

We followed the heat treatment program presented in Figure III-7. Cooling begins when the furnace is turned off at 300 °C.

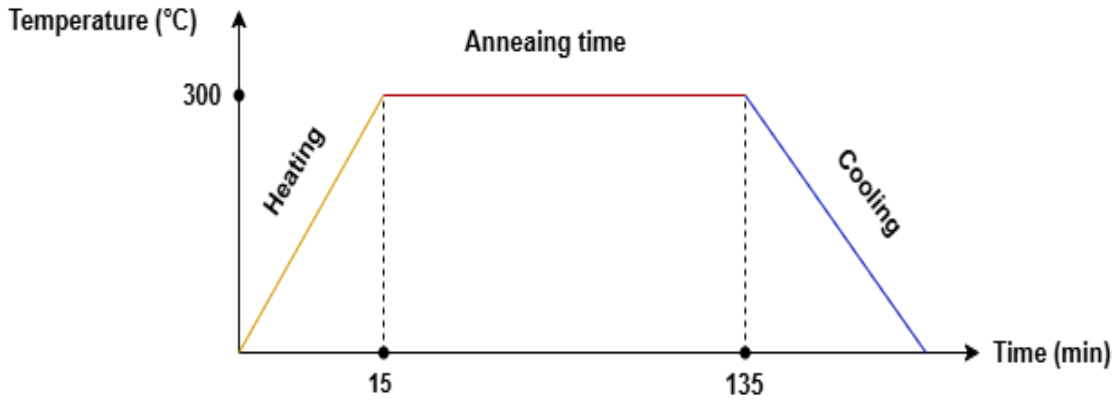


Figure III-7: Diagram representing the stages of the annealing program

f) Polishing the glass to obtain two parallel surfaces

Polishing the glass is an essential step in preparing samples for spectroscopic measurements, which require precise knowledge of the sample thickness and parallelism of its faces to ensure accurate and reliable results. To achieve this, we used a Metkon Forcipol 1V polishing machine (see Figure III-8). The polishing process

began with abrasive papers of progressively finer grit sizes: 600, 1200, and 1600, which effectively removed surface scratches and gradually leveled the glass.

After completing the sanding stages, the process proceeded to final polishing using specialized velvet polishing cloths appropriate for the sample type and specific analytical requirements (Figure III-9b). These cloths were impregnated with diamond paste of varying particle sizes (Figure III-9a) to achieve an ultra-smooth surface and eliminate even the finest surface defects. The polishing precision, choice of cloth, and diamond paste grit were tailored based on the material properties and the intended spectroscopic analysis.

The sanding and polishing steps were carefully repeated until a glass sample with two perfectly parallel and uniformly thick faces was obtained. This preparation ensures accurate measurement of sample thickness and optimal light transmission during spectroscopic analysis. The procedure yields high-quality samples that meet laboratory standards and provide consistent, reproducible results.



Figure III-8: Photograph of the Metkon Forcipol 1V polishing machine

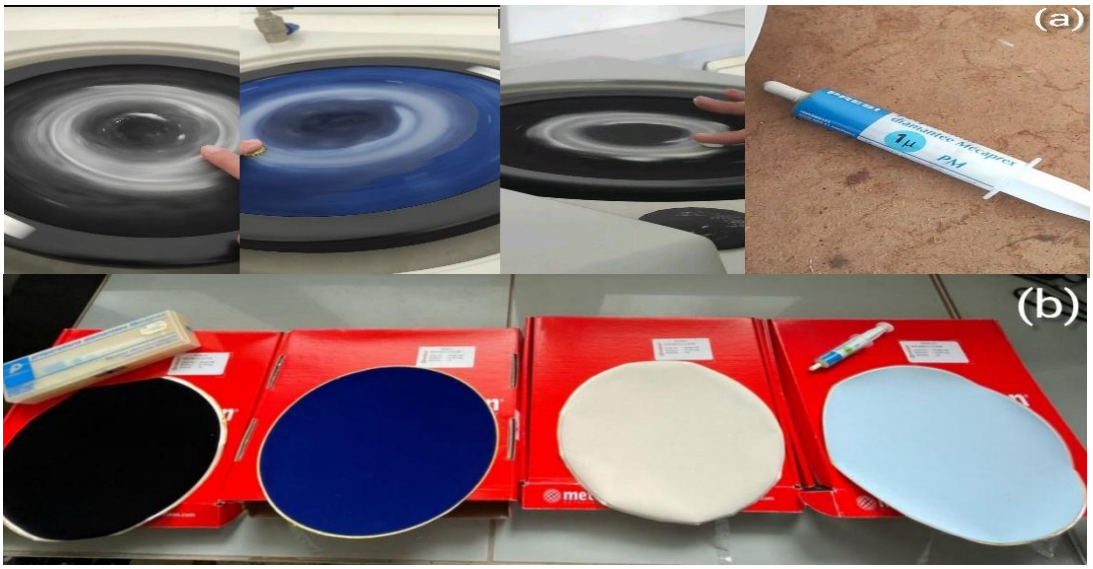


Figure III-9: (a) Photograph of the polisher fed by a cloth on which diamond paste is applied, (b) different cloths used

In addition to the GeO_2–PbO–PbF_2 glass matrix co-doped with Yb^{3+} and Tb^{3+} ions, The GPF glass [7], with a molar composition of $60GeO_2$-20PbO-$9PbF_2$-$9CdF_2$-$2ErF_3$, was synthesized via the conventional melt-quenching technique.

High-purity anhydrous oxides and fluoride precursors (reagent grade) were employed as starting materials. For each batch, 6 g of the precursor mixture was homogenized by vigorous grinding in an agate mortar to ensure chemical uniformity. The resulting powder was transferred into a porcelain crucible and heated at 950 °C for a duration of 10 minutes to achieve a complete and clear melt.

The molten phase was subsequently cast onto a highly polished steel plate to yield glass slabs with a nominal thickness of approximately 3 mm. To relieve internal mechanical stresses, the samples underwent an in-situ annealing process near the glass transition temperature (Tg) for 15 minutes, followed by a controlled inertial cooling to room temperature within the furnace. The fabricated specimen exhibited excellent optical transparency and showed no macroscopic signs of crystallite formation or devitrification Table III-5.

Table III-5: Specific preparation parameters of the Er^{3+}-doped GeO_2–PbO–PbF_2–CdF_2 glass

Characteristic	**Er^{3+}-doped GeO_2 PbO–PbF_2–CdF_2 glass [7]**
Er^{3+} concentration	Low concentration (≤ 2 mol%)
Purity of raw materials	GeO_2 (99.99%), PbO (99.99%), PbF_2 (99.99%), CdF_2 (99.99%),Er_2O_3 (99.99%)
Melting temperature (°C)	~ 950 °C [7]
Melting duration	~ 10 min [7]

Table III-6: Weights of the different chemical components of GPFC glass co-dopedwith Er_2O_3 (2% mol.).

Matrix	60%GeO_2 +20%PbO+9%PbF_2 +9% Cd_2F_2 +2%Er_2O_3				
Chemical components	GeO_2	PbO	PbF_2	CdF_2	Er_2O_3
% molar	60	20	10-x/2 =9	10-x/2 =9	X = 2
Molar masses (g/mol)	104.6088	223.1994	245.1968064	150.4100	382.5162
n (mol)	0.0238	0.0079	0.0035	0.0035	0.0008
m (g) weighed	2.5034	1.7777	0.8780	0.5390	0.3047

III-2. Characterization techniques

III-2-1. Structural characterization by X-ray diffraction

a) Overview of X-ray Diffraction (XRD)

X-rays are electromagnetic waves characterized by a typical wavelength of approximately 0.1 nm. In crystallography, X-ray diffraction is a non-destructive structural characterization technique used to identify the crystalline phases formed

during the processing of a material. This method is based on Bragg's law (Eq. III.5), which states that an incident X-ray beam strikes the surface of the sample at a specific angle, known as the Bragg angle (θ). The beam is then diffracted at the same angle by various families of crystal planes (hkl), producing a detectable signal. This signal is recorded by a detector and displayed as a curve (diffractogram), with distinct peaks appearing at characteristic diffraction angles (see Figure III-10).

$$2\ d\ \sin\ \theta = n\lambda \qquad \text{(Eq. III-5)}$$

The variables in Bragg's law are:

d: the interplanar spacing between two successive parallel planes of the same {hkl} family,

θ: the diffraction angle,

n: the order of diffraction (an integer),

λ: the wavelength of the incident beam.

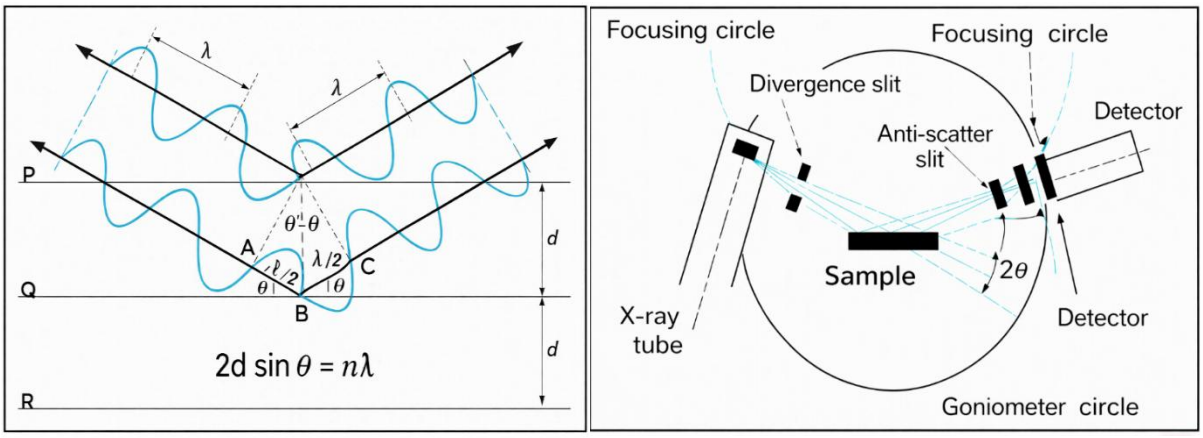


Figure III-10: Illustration of X-ray reflection in accordance with Bragg's Law

b) Bragg-Brentano Geometry

Several instrumental setups are available for X-ray diffraction (XRD) analysis. The Bragg-Brentano geometry is the most widely used, with two main configurations [8]:

- θ – θ mode: in this configuration, the X-ray tube and the detector rotate simultaneously at the same angular speed, while the sample remains stationary.

- θ – 2θ mode: the sample rotates at an angle θ, and the detector moves at an angle 2θ, while the X-ray tube remains fixed.

Both setups include the following standard components:

- An X-ray tube to generate the incident beam.
- Soller slits (also known as divergence and anti-scatter slits), which limit the axial or vertical divergence of the X-ray beam.
- A filter to eliminate background noise caused by fluorescence,
- A detector to measure the reflected signal.

The system typically operates in a fully automated θ – 2θ geometry (see Figure III-11), controlled by specialized software. The sample is mounted on a sample holder and rotates uniformly at an angular velocity ω around a vertical axis. The monochromatic X-ray beam emitted by the source interacts with the sample and is diffracted. The diffracted rays are collected by a detector, whose receiving slit is aligned at the focal point. The detector rotates around the sample at a speed of 2ω and sends the signal to a counter [9].

The angle of incidence is varied step-by-step. At each increment, the counter records the intensity of the reflected ray. When Bragg's condition is fulfilled, the detector records a significant increase in the diffracted intensity [10].

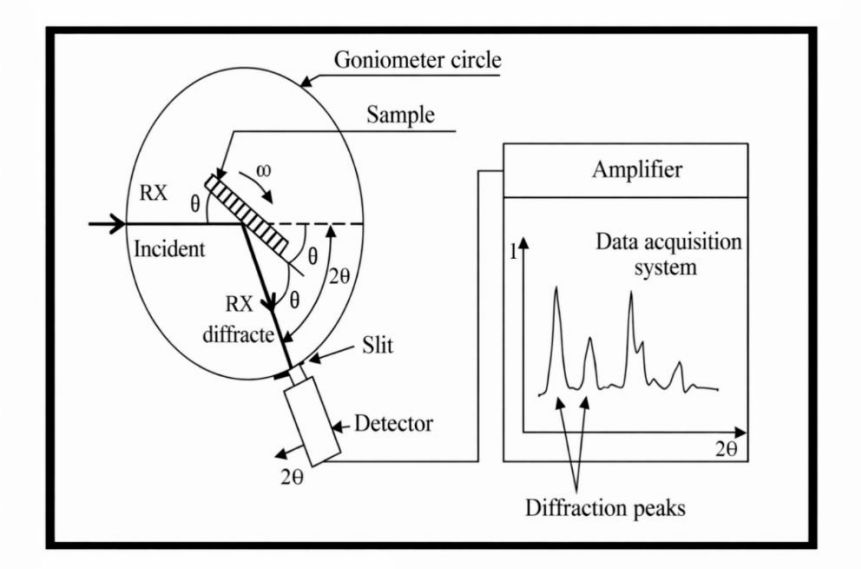


Figure III-11: The geometry of the Bragg-Brentano setup [11]

c) Description of the experimental setup

X-ray diffraction measurements were performed using a Panalytical Empyrean diffractometer (Almelo, The Netherlands) operating in the Bragg–Brentano (θ–2θ) configuration with Cu Kα radiation (λ = 1.5406 Å) (Figure III-12) . The diffraction patterns were recorded on powdered glass samples in order to investigate the structural nature of the synthesized materials and to verify their amorphous character. The obtained diffraction data were subsequently analyzed and discussed in Chapter IV.



Figure III-12: Photograph of the Panalytical Empyrean X-ray diffractometer (7602 EA, Almelo, The Netherlands)

III-2-2. Thermal characterization by differential thermal analysis (DTA)

a) Principle of operation

Differential Thermal Analysis (DTA) is a technique that allows for the observation and comparison of the thermal behavior of a material relative to a thermally inert reference substance, both being subjected simultaneously to the same temperature variations. This technique is particularly useful for identifying various thermal transitions such as the glass transition (Tg), crystallization (Tc), and melting (T_f) of the investigated material.

During controlled heating (or cooling) of a sample and the reference within a furnace, the respective temperatures of the tested material (TE) and the reference (TR) are recorded, as well as the difference between them (ΔT = TR - TE). The thermal behavior

of the reference is linear with respect to the furnace temperature, whereas the investigated material displays deviations due to phase or state transitions. On the ΔT = f(T) curve, these transitions appear as peaks, with the area under each peak proportional to the energy involved; the direction of the peak indicates whether the phenomenon is endothermic or exothermic.

DTA analysis can be effectively complemented by thermogravimetric analysis (TGA), which provides information about the mass variation of the sample as a function of temperature (Δm = f(T)). Additionally, the sensitivity of DTA enables the identification, on a single curve, of the glass transition (endothermic step), crystallization (exothermic peak), and melting (endothermic peak), with each thermal event corresponding to a specific signature based on the atomic structure and mobility of the constituents in the glass.

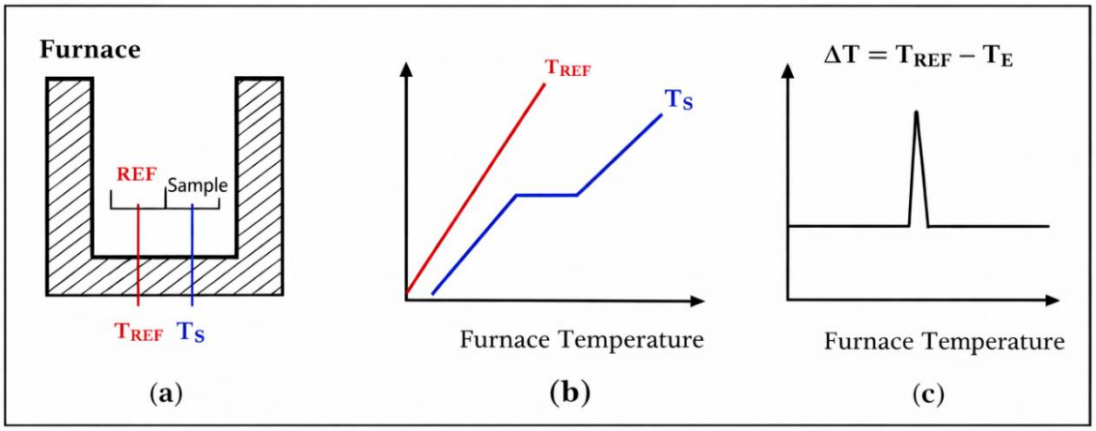


Figure III-13: (a) Principle diagram of the DTA. (b) Deviation from the heating law. (c) DTA curve [2]

b) Description of the equipment

For these measurements, we used a symmetric differential thermal analyzer Setaram (TAG 24) (see Figure III-14), which allows simultaneous thermal and thermogravimetric measurements. The glass samples were ground and sieved beforehand to ensure uniform particle size, as the reproducibility and comparability of DTA results depend strongly on the size of the powder particles studied.

The reference material used was calcined alumina, which is thermally stable in the range 20–900 °C. For each test, approximately 60 mg of sample powder was placed in an alumina crucible, positioned beside another crucible containing the reference

substance. Both crucibles were subjected to a programmed heating up to 850 °C starting from room temperature, at a rate of 10 °C/min under a flow of argon. All relevant thermal phenomena for the glass samples occur below this temperature.

On the resulting thermogram, the baseline corresponds to the thermal response of the reference without any transition. When a transition occurs in the sample (such as T_g, T_c, or T_f), a marked deviation is observed, corresponding to energy absorption or release. The position, shape, and area beneath each peak or plateau allow for the identification of different thermal events:

T_g (glass transition): Endothermic deviation indicating the transition from the glassy state to a more mobile/rubbery state.

T_c (onset of crystallization): Exothermic peak, corresponding to the formation of crystalline phases from the amorphous matrix.

T_f (melting): Endothermic peak associated with the absorption of heat during the melting of the crystalline network.

A proper interpretation of DTA results relies on the clear distinction of the various peaks and plateaus and the precise determination of characteristic temperatures, which requires careful sample preparation and strict control of experimental conditions.



Figure III-14: A symmetric Setaram analyzer (TAG 24)

III-2-3. Recording of absorption and emission spectra

III-2-3-1. Recording of absorption spectra

a) Absorption spectra at room temperature

We recorded the room temperature absorption spectrum of the GPF glass matrix co-doped with Terbium and Ytterbium using a double-beam spectrophotometer, which operates in the three spectral ranges - UV, visible, and near-infrared. This instrument covers the spectral range from 200 to 3200 nm and is of the SHIMADZU UV-3600 PLUS brand (Figure III-15), provided by ENSET Azzaba Skikda.



Figure III-15: Photograph of the SHIMADZU UV-3600 PLUS spectrophotometer

b) Description of the SHIMADZU UV-3600 PLUS spectrophotometer

The SHIMADZU UV-3600 PLUS spectrophotometer operates by measuring the absorbance or transmittance of a sample over a wide spectral range, from ultraviolet (UV) to near infrared (NIR), typically from 185 to 3300 nm. It uses a double beam system with three separate detectors: a photomultiplier for UV-visible, an InGaAs for near-infrared, and a PbS for the longest wavelengths of the NIR, ensuring high sensitivity and a wide dynamic range. The light from a source (deuterium lamp for UV and halogen for visible/NIR) passes through a grating monochromator that selects a specific wavelength. The beam is then split: one passes through the sample, the other through a reference blank. The transmitted intensities are compared, allowing the absorbance to be calculated according to Beer-Lambert's law. The instrument is often

used in scan mode to obtain spectra, or in fixed mode to measure at one or several specific wavelengths [13].

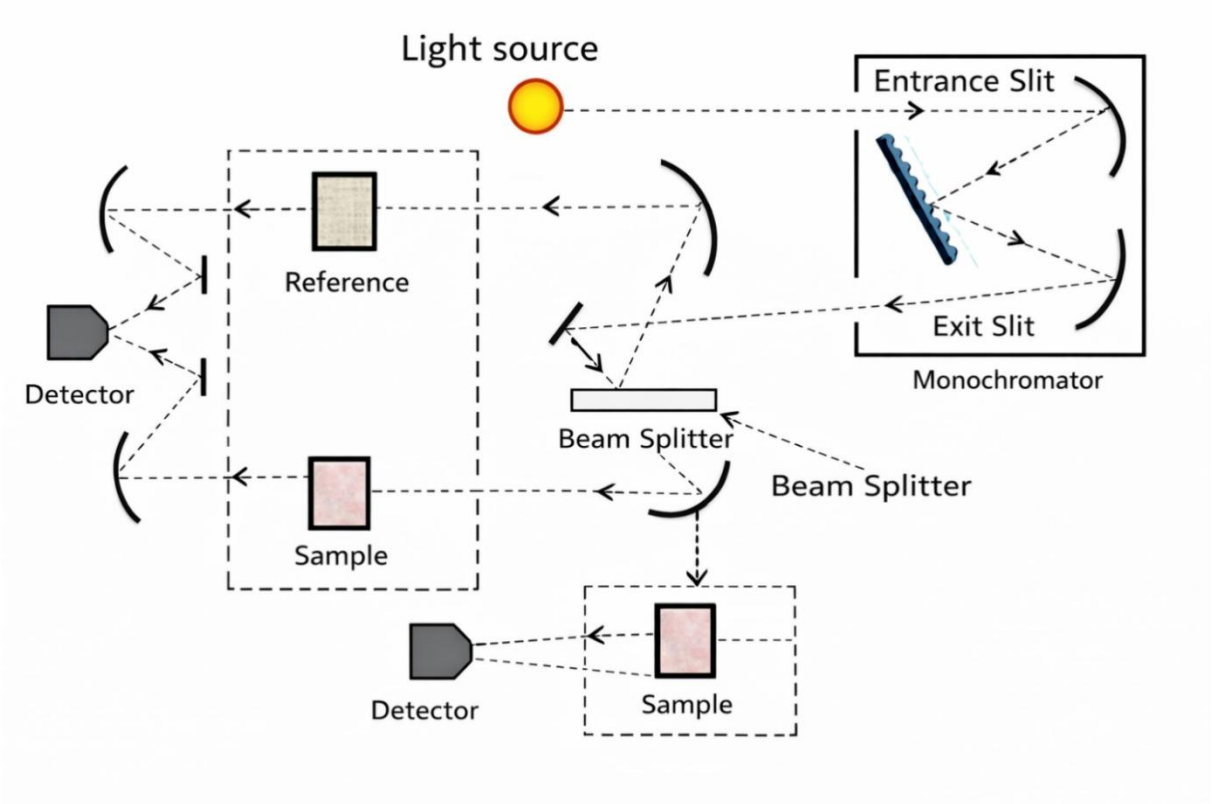


Figure III-16: Principle diagram of a double-beam spectrophotometer [14]

III-2-3-2. Recording of emission spectra

a) Emission spectra at room temperature

To record the emission spectra, we used a Fluoromax-4 luminescence spectrofluorometer, designed by Horiba, with a spectral range from 200 to 900 nm. These fluorescence analyses were conducted at the LAPLASO laboratory of Badji Mokhtar University Annaba.

b) Description of the Horiba Fluoromax-4 spectrofluorometer

An excitation monochromator is illuminated by a continuous light source, which selects a specific range of wavelengths. A sample that produces luminescence is illuminated by this monochromatic excitation light. The luminescence is directed towards a second emission monochromator which selects

a range of wavelengths and disperses them onto a detector. The signal from the detector is sent to a system controller and a host computer, where this information can be processed and displayed via specific software.



Figure III-17: Photograph of the Horiba brand spectrofluorometer, model Fluoromax-4, available at the LAPLASO laboratory of the University of Annaba

c) Optical arrangement

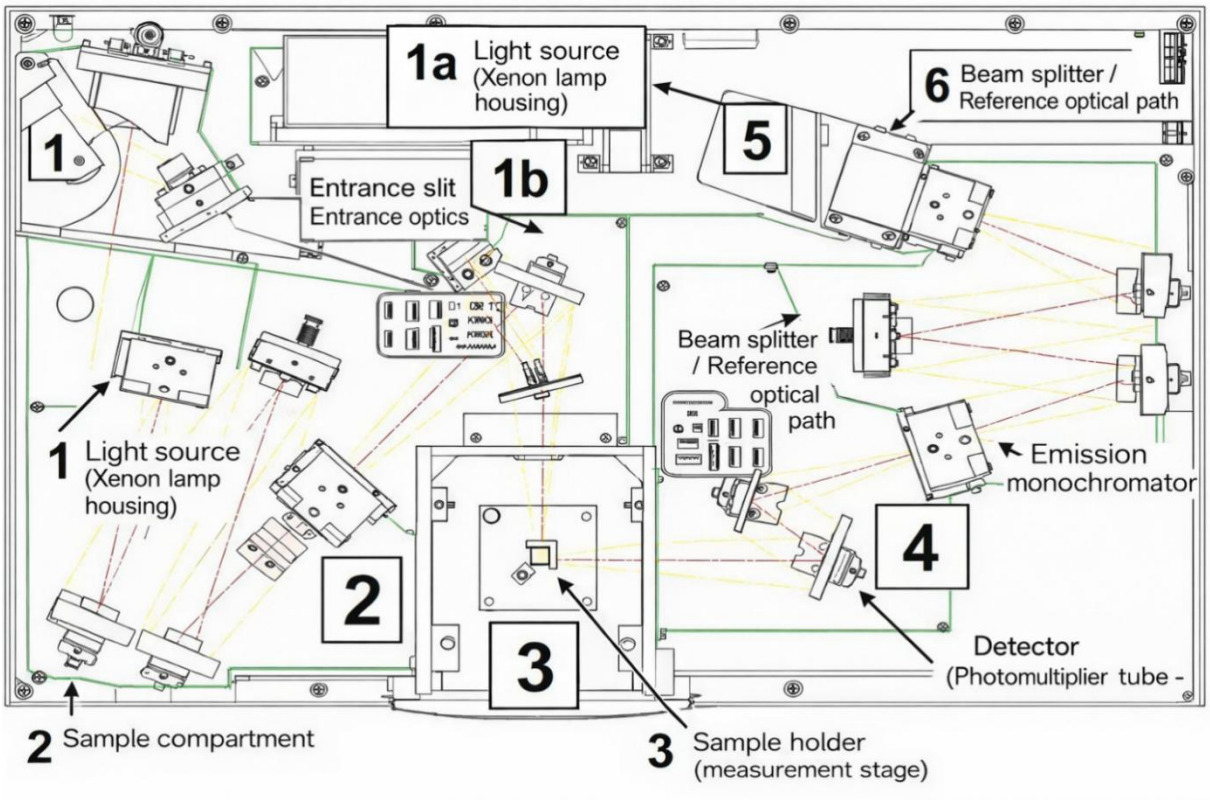


Figure III-18: Descriptive diagram of the Horiba Fluoromax-4 spectrofluorometer

1) Xenon arc lamp and lamp housing

a) The xenon lamp is powered by a 150 W source, operating without ozone and using a xenon arc. A diamond-polished elliptical mirror captures the light from the lamp, which is then focused onto the entrance aperture of the excitation monochromator. The lamp housing is separate from the excitation monochromator by a quartz glass.

b) A xenon flash lamp (Fluoro-Max®-4P) is also offered. This lamp operates thanks to a speed-controlled motor managed by Fluor-Essence™, which rotates the mirror in the illumination zone, thus allowing the transition from the CW source to the flash lamp.

2) Excitation monochromator

3) Sample compartment

4) Emission monochromator

5) Signal detector (composed of a photomultiplier tube and a housing)

6) Reference detector (including a photodiode and a current acquisition module)

III-2-3-3. Photoluminescence measurements

Photoluminescence measurements were performed at room temperature to investigate the down-conversion and up-conversion emission properties of GeO_2–PbO–PbF_2 glass samples codoped with 1 mol% Tb^{3+} and 4 mol% Yb^{3+} ions. Down-conversion emission spectra were recorded under ultraviolet excitation at 375 nm using a Horiba spectrofluorometer (Fluoromax-4 model), equipped with a xenon arc lamp as the excitation source, a double-grating monochromator for wavelength selection, and a photomultiplier tube (PMT) detector optimized for the ultraviolet–visible spectral range. The excitation and emission slit widths were set to typical values of 2–5 nm in order to achieve a suitable compromise between spectral resolution and signal-to-noise ratio. This commercial spectrofluorometer was selected for steady-state measurements due to its high spectral stability, reproducibility, and accurate intensity calibration, which are essential for reliable comparison of emission intensities and spectral line shapes.

Up-conversion (UC) luminescence experiments were carried out using a homemade optical spectroscopy setup under near-infrared excitation provided by continuous-wave diode lasers operating at 976 nm and 940 nm. The excitation power was varied up to several hundred milliwatts to probe power-dependent UC behavior. The excitation

beam was focused onto the polished surface of the samples, and the emitted luminescence was collected in a front-face geometry to minimize reabsorption and waveguiding effects in the bulk glass. The collected emission was dispersed by a monochromator equipped with a diffraction grating optimized for the visible spectral range and detected using a photomultiplier tube. All steady-state emission spectra were corrected for the wavelength-dependent instrumental response of the detection system and normalized with respect to the incident excitation power to ensure quantitative comparison of emission intensities and accurate analysis of up-conversion efficiency.

III-2-3-4. Time-resolved photoluminescence measurements

Time-resolved photoluminescence measurements were conducted at room temperature to investigate the luminescence dynamics and energy transfer mechanisms in the codoped glass system. Pulsed excitation at 976 nm was provided by an optical parametric oscillator (OPO) laser delivering pulses with a duration of 5 ns at a repetition rate of 10 Hz. This excitation wavelength was chosen to selectively excite Yb^{3+} ions and thereby probe the $Yb^{3+} \rightarrow Tb^{3+}$ energy transfer process. Time-resolved emission spectra were recorded over the spectral range of 420–680 nm.

Fluorescence decay curves were measured at selected emission wavelengths of 490, 545, 580, and 621 nm, corresponding to the $^5D_4 \rightarrow 7F_J$ (J = 6, 5, 4, and 3) transitions of Tb^{3+} ions, respectively. The emitted signal was detected using a fast photomultiplier tube coupled to a time-correlated detection system. To account for the finite temporal resolution of the experimental setup, the measured decay profiles were deconvoluted with the instrument response function (IRF), which was independently determined using the scattered excitation pulse. The corrected decay curves were subsequently analyzed using least-squares fitting procedures based on single-exponential or multi-exponential decay models, depending on the emission channel. This approach enables accurate determination of fluorescence lifetimes and provides insight into the radiative and non-radiative relaxation processes, as well as the efficiency of energy transfer mechanisms between Yb^{3+} sensitizers and Tb^{3+} activator ions.

Bibliographic references

[1] G. Dantelle, *Thèse de doctorat*, Université Pierre et Marie Curie (Paris VI) (2006).

[2] C. Bensalem, *Thèse de doctorat*, Université Badji Mokhtar, Annaba (2010).

[3] G. Dominiak-Dzik, B. Klimesz & B. Ryba-Romanowski, Optical properties of rare-earth doped materials, *Opt. Appl.*, 40(2) (2010).

[4] M. Mortier & F. Auzel, Rare-earth doped glasses, *J. Non-Cryst. Solids*, 361 (1999) 256.

[5] B. Klimesz, G. Dominiak-Dzik, P. Solarz, M. Żelechower & W. Ryba-Romanowski, Spectroscopic investigation of rare-earth doped glass, *J. Alloys Compd.*, 403(1–2) (2005) 76.

[6] L. A. Bueno, P. Melnikov, Y. Messaddeq & S. G. L. Ribeiro, Structural and optical studies on rare-earth doped glasses, *J. Non-Cryst. Solids*, 247 (1999) 87.

[7] Z. Pan, A. Ueda, S. H. Morgan & R. Mu, Luminescence of Er^{3+} in oxyfluoride transparent glass-ceramics, *J. Rare Earths*, 24(6) (2006) 699–705. https://doi.org/10.1016/S1002-0721(07)60012-X

[8] F. Hamzaoui & N. Bettahar, *Cristallographie: cours et exercices*, Elbayane (2001).

[9] F. Serna, J. Lagneau & J. M. Carpentier, La diffraction des rayons X: une technique puissante pour résoudre certains problèmes industriels et technologiques, *Chim. Nouv.*, (2014) 1–12.

[10] P. L. Hauff & G. VanTrump Jr., Laboratory manual mineral X-ray diffraction data retrieval/plot computer program (76-407), U.S. Geological Survey (1976).

[11] OpenStax College, *College Physics*, Chapter 11.7: Archimedes' Principle and Density Measurements, Lumen Learning (2016). https://courses.lumenlearning.com/suny-physics/chapter/11-7-archimedes-principle/

[12] D. A. Skoog, D. M. West, F. J. Holler & S. R. Crouch, *Fundamentals of analytical chemistry*, 9th ed., Brooks/Cole, Cengage Learning (2013).

[13] L'Usine Nouvelle Expo, UV-Visible-NIR Spectrophotometer, consulted June 2025. https://www.usinenouvelle.com/expo/spectrophotometre-uv-visible-nir-3-det-p65983723.html

[14] Djellab-Sihem, *Doctoral thesis*, Badji Mokhtar University, Annaba (2014).

Chapter IV: Results and Interpretations

Introduction

This chapter presents the experimental results obtained for rare-earth-doped oxyfluoride glass systems, with the objective of establishing correlations between their structural, thermal, and optical properties and the resulting luminescent behavior. Particular emphasis is placed on the investigation of near-infrared-excited up-conversion luminescence in Tb^{3+}/Yb^{3+} co-doped GeO_2–PbO–PbF_2 glass, including the analysis of excitation power dependence, $Yb^{3+} \rightarrow Tb^{3+}$ energy-transfer mechanisms, and relaxation dynamics investigated through time-resolved photoluminescence measurements. Optical absorption spectroscopy is also employed to determine the characteristic absorption features of the dopant ions and the optical band gap of the host matrix.

In addition, chromaticity analysis based on the CIE 1931 color coordinates is carried out to evaluate the emission color characteristics and stability of the up-conversion emission. Finally, a Judd–Ofelt spectroscopic analysis of the Er^{3+}-doped oxyfluoride glass is performed to determine the intensity parameters, radiative transition probabilities, branching ratios, and radiative lifetimes, providing further insight into the spectroscopic performance, laser potential, and photonic applicability of the investigated materials.

IV-1. Physical properties of Tb^{3+}/Yb^{3+} co-doped GPF oxyfluoride glass

The density of the glass at room temperature was determined using Archimedes' principle, which is a widely used and reliable method for dense and irregularly shaped solid materials such as glasses. In this technique, the density is obtained by comparing the weight of the sample measured in air with its apparent weight when immersed in a liquid of known density. Ethanol, with a density of $\rho_b = 0{,}78592 g/cm^3$, was selected as the immersion liquid in order to ensure good wetting of the glass surface and to minimize measurement uncertainties.

The density ρ of the glass was calculated using the relation [1]:

$$\rho = \frac{(\rho_b w_a)}{w_a - w_b} \qquad \text{(Eq. IV-1)}$$

Where: w_a is the weight of the glass in air, $w_b$is the weight of the glass in distilled water and ρ_b is the density of ethanol, respectively. Using this method, the density of the Tb^{3+}/Yb^{3+} co-doped GeO_2–PbO–PbF_2 oxyfluoride glass was found to be $\rho = 5.681\ g/cm^3$.

This relatively high density is mainly related to the presence of heavy metal components, particularly PbO and PbF_2, in the glass composition. The measured density value was subsequently used to calculate the molar volume (V_m), which provides useful information on the compactness of the glass network. The molar volume was determined using the expression [1]:

$$V_m = \frac{M_g}{\rho} \qquad \text{(Eq. IV-2)}$$

Where: M_g is the molar mass of the glass, computed from the weighted sum of the molar masses of the individual constituents according to:

$$M_g = \sum \chi i Mi \qquad \text{(Eq. IV-3)}$$

in which χ_i and Mi representing the molar fraction and molar mass of each constituent, respectively. The computed molar mass was $Mg = 184.042\ g/mol$ leading to a molar volume of $V_m = 32.395\ cm^3/mol$. This value reflects a relatively compact glass structure, consistent with the heavy-metal-rich nature of the oxyfluoride host.

In addition, the concentration of terbium ions in the glass was estimated in order to provide a quantitative description of the rare-earth content. The ion concentration was calculated using the following relation [1]:

$$N_{ions} = \frac{x\rho N_A}{M_g} \qquad \text{(Eq. IV-4)}$$

where x represents the mole fraction of Tb^{3+} ions and N_A is Avogadro's number. The resulting terbium ion concentration was found to be $N = 7.34x10^{20} ion/cm^3$

This value gives an estimate of the average number of optically active Tb^{3+} ions per unit volume and is useful for interpreting the luminescence and energy transfer processes discussed in the following sections.

IV-2. Structural characterization of Tb^{3+}/Yb^{3+} co-doped GPF oxyfluoride glass

As detailed in Chapter III (Experimental Methods), X-ray diffraction (XRD) was employed to investigate the structural nature of the synthesized $50GeO_2$–$30PbO$–$20PbF_2$ oxyfluoride glass co-doped with Tb^{3+} and Yb^{3+} ions. The X-ray diffraction pattern of the powdered glass sample was recorded at the Laboratory of Magnetism and Solid-State Spectroscopy (LM2S), University of Annaba, and is presented in Figure IV-1.

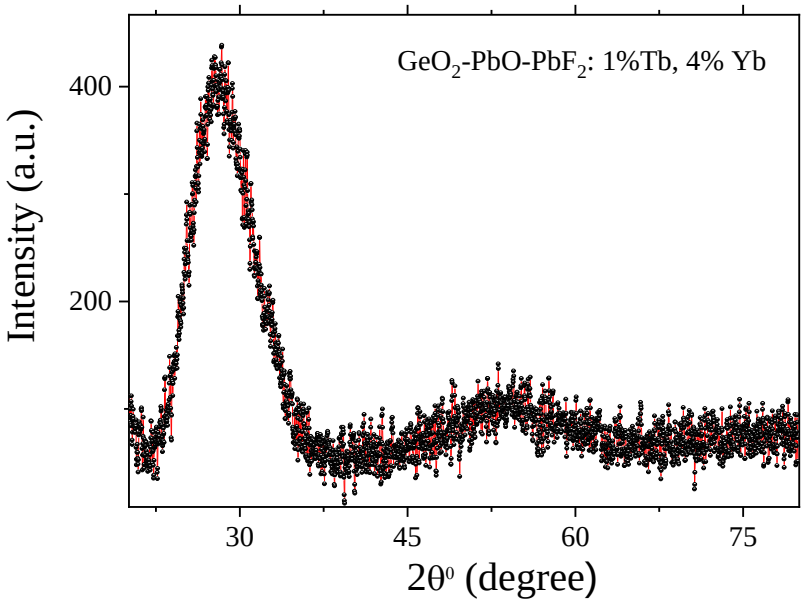


Figure IV-1: XRD spectrum of Tb^{3+}–Yb^{3+} co-doped GeO_2–PbO–PbF_2 oxyfluoride glass

The diffractogram does not exhibit any sharp or well-defined Bragg reflections, but instead shows two broad diffuse halos centered approximately at $2\theta \approx 33°$ and $2\theta \approx 55°$. These diffuse features are characteristic of amorphous materials and indicate the absence of long-range crystalline order in the glass sample.

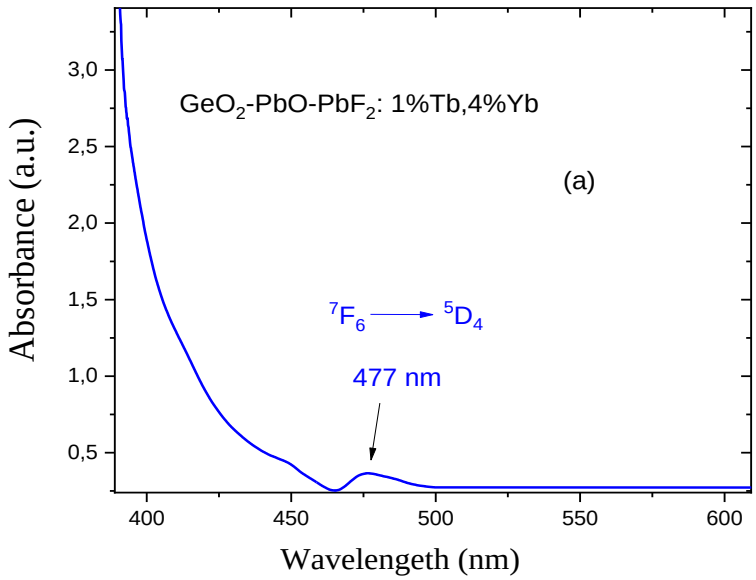
The absence of crystalline peaks confirms that the incorporation of Tb^{3+} and Yb^{3+} ions does not induce crystallization or phase separation within the GeO_2–PbO–PbF_2 glass matrix. This result shows that the selected synthesis conditions and dopant concentrations are suitable for maintaining a stable amorphous structure, even with a

relatively high Yb^{3+} content. Similar amorphous XRD patterns have been reported for rare-earth-doped GeO_2–PbO–PbF_2 and related oxyfluoride glasses [2].

From an optical point of view, preserving the amorphous structure is advantageous because it ensures a homogeneous distribution of rare-earth ions and limits light scattering losses. This structural homogeneity is beneficial for the luminescence and up-conversion properties discussed in the following sections.

IV-3. Optical absorption spectroscopy of Tb^{3+}/Yb^{3+} co-doped GPF oxyfluoride glass

Optical absorption spectroscopy was employed to investigate the electronic transitions associated with the rare-earth ions incorporated into the GeO_2–PbO–PbF_2 oxyfluoride glass and to assess the optical transparency of the host matrix. The absorption spectrum of the Tb^{3+}/Yb^{3+} co-doped glass was recorded at room temperature over the ultraviolet, visible, and near-infrared spectral regions, following the experimental procedure described in Chapter III. The resulting absorption spectrum is presented in Figure IV-2.



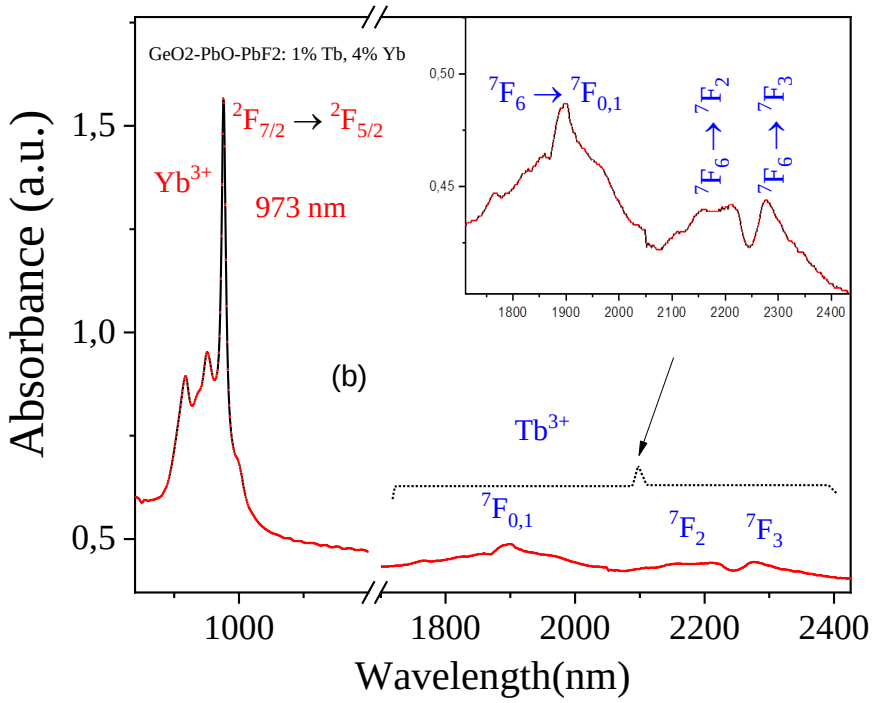


Figure IV-2: Absorption spectrum of Tb^{3+}–Yb^{3+} co-doped GeO_2–PbO–PbF_2 oxyfluoride glass: (a) visible range, (b) infrared (IR) range

In the ultraviolet and visible regions, shown in Figure IV-2a and spanning from 320 to 500 nm, the absorption spectrum exhibits several weak and narrow bands attributed to intra-4f electronic transitions of Tb^{3+} ions originating from the $^7F_6$ ground state. Such weak absorption features are characteristic of Tb^{3+}-doped glass systems and are commonly observed in oxide and oxyfluoride hosts. Among these transitions, a weak absorption band located around 477 nm is assigned to the $^7F_6 \rightarrow {}^5D_4$ transition of Tb^{3+} ions. The presence of this band confirms the successful incorporation of optically active Tb^{3+} centers within the GeO_2–PbO–PbF_2 glass matrix. Similar absorption features associated with Tb^{3+} ions, with comparable spectral positions and intensities, have been widely reported in Tb^{3+}-doped and Tb^{3+}/Yb^{3+} co-doped oxide and oxyfluoride glass systems [3].

In contrast, the near-infrared region of the absorption spectrum, shown in Figure IV-2b, is dominated by a strong and well-defined absorption band centered around 973–976 nm. This intense band is attributed to the $^2F_{7/2} \rightarrow {}^2F_{5/2}$ transition of Yb^{3+} ions and represents the characteristic absorption fingerprint of this ion. The high intensity of this band reflects the strong absorption capability of Yb^{3+} ions in the near-infrared region and confirms their effective incorporation into the GeO_2–PbO–PbF_2 glass matrix.

Similar intense Yb^{3+} absorption bands near 980 nm, corresponding to the $^2F_{7/2} \rightarrow {}^2F_{5/2}$ transition, have been widely reported in Yb^{3+}-doped and Tb^{3+}/Yb^{3+} co-doped systems and are known to play a crucial role in near-infrared excitation and energy transfer processes [4-6].

The coexistence of weak Tb^{3+} absorption bands in the ultraviolet–visible region and a strong Yb^{3+} absorption band in the near-infrared region is of particular importance for the optical performance of the studied glass. This complementary absorption behavior allows both direct excitation of Tb^{3+} ions under ultraviolet or visible irradiation and indirect excitation through Yb^{3+} sensitization under near-infrared excitation. Such excitation pathways form the basis for the $Yb^{3+} \rightarrow Tb^{3+}$ energy transfer and up-conversion luminescence mechanisms discussed in the subsequent sections.

In addition, the absorption edge of the GeO_2–PbO–PbF_2 host matrix shows a sharp increase in the ultraviolet region, corresponding to intrinsic absorption of the glass network. This behavior, together with the wide transparency window extending from the visible to the near-infrared region, is consistent with previous reports on similar oxyfluoride glass systems and confirms the suitability of this material for photonic applications requiring low optical losses [7].

IV-4. Optical energy gap of Tb^{3+}/Yb^{3+} co-doped GeO_2–PbO–PbF_2 oxyfluoride glass

The absorption spectrum was employed to investigate the optical transitions and the electronic band structure of the Tb^{3+}/Yb^{3+} co-doped GeO_2–PbO–PbF_2 oxyfluoride glass. According to the Davis and Mott theory [8], the optical band gap energy of amorphous materials can be determined by analyzing the absorption edge associated with direct and indirect allowed transitions.

The absorption coefficient α(ν) was calculated from the measured absorbance A using the following relation [9-11].

$$\alpha(\nu) = A\, ln(10) / l \qquad \text{(Eq. IV-5)}$$

where A is the absorbance and l represents the thickness of the glass sample. In general, the relationship between the absorption coefficient $\alpha(\nu)$ and the photon energy of the incident radiation $h\nu$ is described by the Tauc expression [9-11]:

$$\alpha h\upsilon = A\,(h\nu - Eg)^n \qquad \text{(Eq. IV-6)}$$

where $h\nu$ is the photon energy, Eg is the optical band gap, and n is a parameter that depends on the nature of the electronic transition, with $n = 1/2$ and $n = 2$ corresponding to allowed direct and allowed indirect transitions, respectively.

Figure IV.3 illustrates the plots of $(\alpha h\upsilon)^2$ versus $h\nu$ for the GeO_2–PbO–PbF_2 glass doped with 1% Tb^{3+} and 4% Yb^{3+}. The extrapolation of the linear region of the curve to $(\alpha h\nu)^2 = 0$ yields the value of the direct optical band gap. Based on this analysis, the direct band gap energy (E_g^d) was estimated to be approximately 2.95 eV, while the indirect band gap (E_g^{ind}) was found to be around 2.45 eV, as determined from the $(\alpha h\upsilon)^{1/2} = 0$ versus $h\nu$ plot.

These values confirm that the investigated material behaves as a wide band gap semiconductor, characterized by strong absorption in the ultraviolet region. Such a wide optical band gap, combined with the efficient visible and near-infrared luminescence discussed in the previous sections, makes the Tb^{3+}/Yb^{3+} co-doped GeO_2–PbO–PbF_2 oxyfluoride glass a promising candidate for ultraviolet and infrared detection, optoelectronic devices, and energy conversion technologies [12].

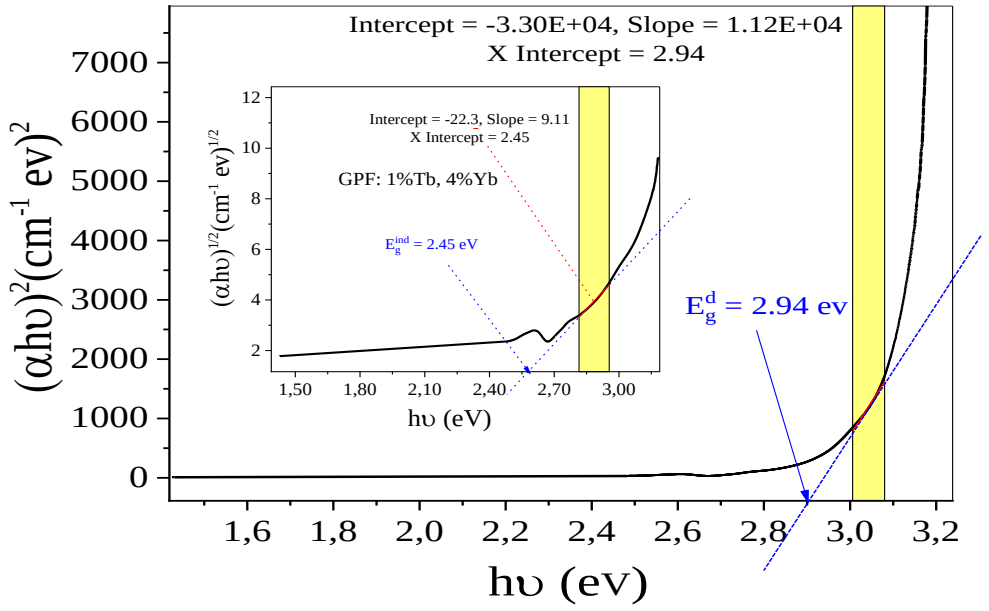


Figure IV-3: Tauc plots of Tb^{3+}–Yb^{3+} co-doped GeO_2–PbO–PbF_2 oxyfluoride glass. In insert, indirect band gap (E_g^{ind})

IV-5. Excitation spectroscopy of Tb^{3+}/Yb^{3+} co-doped GeO_2–PbO–PbF_2 oxyfluoride glass

The excitation spectrum of the Tb^{3+}/Yb^{3+} co-doped GeO_2–PbO–PbF_2 oxyfluoride glass was recorded at room temperature in the 200–550 nm spectral range while monitoring the characteristic green emission of Tb^{3+} ions at 545 nm, corresponding to the $^5D_4 \rightarrow {}^7F_5$ transition (Figure IV-3). This measurement configuration allows selective probing of the excitation channels that effectively populate the emitting levels of Tb^{3+} ions in the investigated glass matrix.

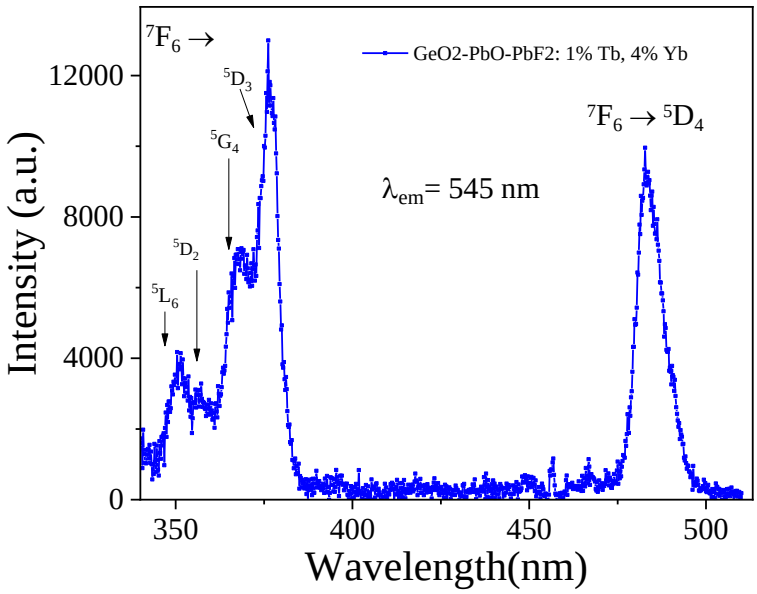


Figure IV-4: Excitation Spectrum of Tb^{3+}–Yb^{3+} co-doped GeO_2–PbO–PbF_2 oxyfluoride glass

The excitation spectrum exhibits several narrow and well-resolved peaks, which are attributed to intra-configurational $4f^8 \rightarrow 4f^8$ electronic transitions of Tb^{3+} ions originating from the $^7F_6$ ground state toward higher-lying excited states. These transitions include the $^7F_6 \rightarrow {}^5L_6$, $^5D_2$, $^5G_4$, $^5D_3$, and $^5D_4$ manifolds. The presence of these well-defined excitation bands reflects the characteristic excitation behavior of Tb^{3+} ions in glassy hosts and is consistent with excitation spectra reported for Tb^{3+}-doped and Tb^{3+}/Yb^{3+} co-doped oxide and oxyfluoride glasses [4-6]. Their observation confirms that the local environment of Tb^{3+} ions in the present GeO_2–PbO–PbF_2 matrix preserves the typical electronic structure of this ion.

Among the observed excitation bands, the most intense excitation peak is located at approximately 375 nm and is assigned to the $^7F_6 \rightarrow {}^5D_4$ transition of Tb^{3+} ions. The dominance of this band indicates that excitation at this wavelength efficiently promotes Tb^{3+} ions directly into the emitting $^5D_4$ level, which is responsible for the characteristic green luminescence. Owing to its high excitation efficiency, 375 nm was therefore selected as the excitation wavelength for recording the emission spectra, ensuring optimal population of the emitting state.

It is also observed that the Tb^{3+}/Yb^{3+} co-doped system exhibits a relatively broad excitation range and improved excitation efficiency compared to singly doped systems. This behavior can be attributed to the presence of Yb^{3+} ions, which modify the excitation dynamics of the system and contribute to enhanced excitation processes. Similar broadening of the excitation range and improvement in excitation efficiency have been reported in other Tb^{3+}/Yb^{3+} co-doped glass systems, further supporting the role of Yb^{3+} ions as effective sensitizers in such materials [4–6].Overall, the excitation spectroscopy results demonstrate that ultraviolet excitation in the vicinity of 375 nm provides an efficient pathway for populating the emitting levels of Tb^{3+} ions in the GeO_2–PbO–PbF_2 oxyfluoride glass. These findings establish a clear basis for the interpretation of the emission spectra and the luminescence properties discussed in the following section.

IV-6. Up-Conversion Emission of Tb^{3+}/Yb^{3+} Co-doped GeO_2–PbO–PbF_2 Oxyfluoride Glass

IV-6-1. Up-conversion emission spectra under NIR excitation

Figure IV-5 presents the room-temperature emission spectra of the GeO_2–PbO–PbF_2 glass co-doped with 1% Tb^{3+} and 4% Yb^{3+}, recorded under two different excitation wavelengths at 375 nm and 976 nm. Under ultraviolet excitation at 375 nm, the emission spectrum exhibits two groups of spectral lines arising from radiative transitions from the excited $^5D_3$ and $^5D_4$ levels to the ^7F_j levels of Tb^{3+} ions.

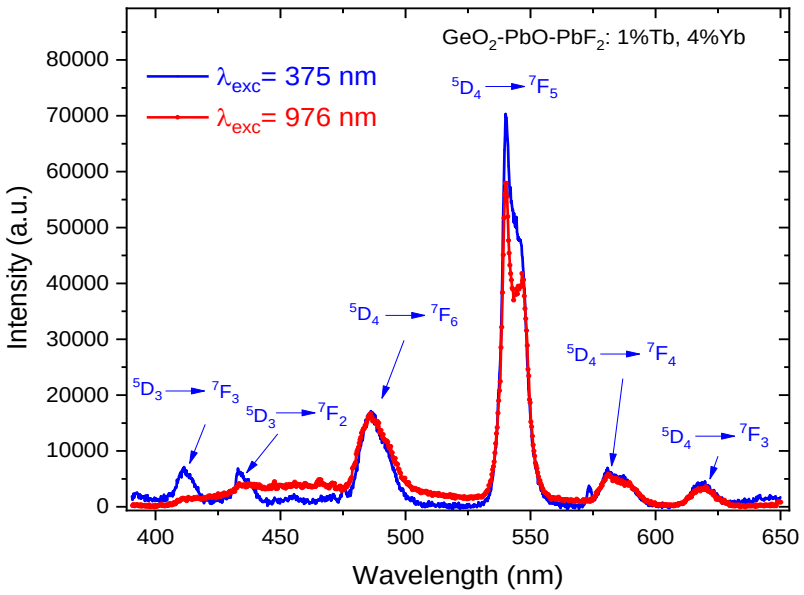


Figure IV-5: Emission spectra of Tb^{3+}–Yb^{3+} co-doped GeO_2–PbO–PbF_2 oxyfluoride glass under 375 nm and 976 nm excitation wavelengths

The first group includes the $^5D_3 \rightarrow {}^7F_3$ and $^5D_3 \rightarrow {}^7F_2$ transitions, located at approximately 412 and 434 nm, respectively, while the second group consists of the $^5D_4 \rightarrow {}^7F_6$, $^5D_4 \rightarrow {}^7F_5$, $^5D_4 \rightarrow {}^7F_4$, and $^5D_4 \rightarrow {}^7F_3$ transitions, located at about 486, 545, 586, and 620 nm, respectively. The distribution of the emission intensities shows good agreement with previously reported results for similar Tb^{3+}-doped systems [13].

Under near-infrared excitation at 976 nm, the emission behavior changes markedly, as the transitions originating from the $^5D_3$ level completely disappear, while emissions associated with the $^5D_4$ level become dominant. In particular, the $^5D_4 \rightarrow {}^7F_6$ (blue) and $^5D_4 \rightarrow {}^7F_5$ (green) transitions prevail, with a clear dominance of the green emission centered at 545 nm [14, 15]. This behavior indicates that the emitting $^5D_4$ level is efficiently populated under NIR excitation.

Since Tb^{3+} ions do not exhibit significant absorption in the near-infrared region, the observation of intense Tb^{3+}-related visible emissions under 976 nm excitation confirms the occurrence of an up-conversion process sensitized by Yb^{3+} ions. In this mechanism, Yb^{3+} ions absorb NIR photons through the $^2F_{7/2} \rightarrow {}^2F_{5/2}$ transition and subsequently transfer the excitation energy to neighboring Tb^{3+} ions, leading to the population of the

emitting $^5D_4$ level and the emission of higher-energy photons in the visible region [16, 17]. A similar spectral distribution dominated by the $^5D_4 \rightarrow {}^7F_5$ transition has been widely reported for Tb^{3+}/Yb^{3+} co-doped germanate and oxyfluoride glass systems, where Yb^{3+} ions act as efficient sensitizers for Tb^{3+} up-conversion emission [18-20].

It is also observed that the absence of emissions originating from the $^5D_3$ level under NIR excitation is a common feature of Tb^{3+}/Yb^{3+} co-doped systems. This behavior is generally attributed to the fact that the up-conversion mechanism preferentially populates the lower-energy $^5D_4$ level through energy transfer processes involving Yb^{3+} ions, in contrast to ultraviolet excitation, where both the $^5D_3$ and $^5D_4$ levels are directly populated.

IV-6-2. Power dependence of the up-conversion emission

To further elucidate the physical origin of the up-conversion (UC) luminescence observed in the Tb^{3+}/Yb^{3+} co-doped GeO_2–PbO–PbF_2 oxyfluoride glass, the evolution of the emission intensity as a function of the incident pump power was systematically investigated. Figure IV-6 presents the diode-laser pump power dependence of the UC emission spectra recorded under near-infrared excitation at 940 nm, with the excitation power varied from 300 to 600 mW.

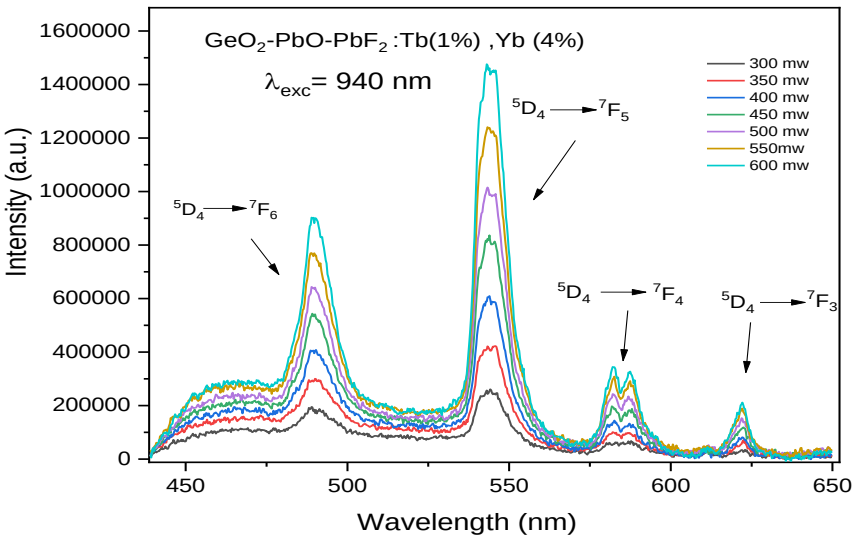


Figure IV-6: Diode laser pump power evolution of the emission spectrum of Tb^{3+}–Yb^{3+} co-doped GeO_2–PbO–PbF_2 oxyfluoride glass over the range 300-600 mW ($\lambda_{exc} = 940nm$).

As the pump power increases, a pronounced and continuous enhancement of the UC emission intensity is observed for all characteristic Tb^{3+} emission bands located at approximately 486 nm ($^5D_4 \rightarrow {}^7F_6$), 545 nm ($^5D_4 \rightarrow {}^7F_5$), 580 nm ($^5D_4 \rightarrow {}^7F_4$), and 620 nm ($^5D_4 \rightarrow {}^7F_3$). Importantly, the spectral positions of these emission peaks remain unchanged over the entire investigated power range, indicating that the luminescence originates from intrinsic electronic transitions of Tb^{3+} ions rather than from thermally activated processes or defect-related emissions.

Although the power-dependent measurements were performed at 940 nm instead of the commonly used 976 nm excitation wavelength, this choice does not affect the interpretation of the UC mechanism. Indeed, Yb^{3+} ions exhibit a broad absorption band extending from approximately 900 to 980 nm associated with the $^2F_{7/2} \rightarrow {}^2F_{5/2}$ transition, and therefore similar sensitization and energy transfer processes are expected to operate under both excitation wavelengths [16-17].

To quantitatively analyze the UC process, the dependence of the emission intensity (I) on the pump power (P) was examined using the empirical relation $I \propto P^n$, where *n* represents the number of photons involved in populating the emitting level. The corresponding log–log plots of emission intensity versus pump power (Figure IV-7) yield slopes of approximately $n \approx 2$ for the main Tb^{3+} emission bands. Such values clearly indicate that the UC emission is governed by a two-photon process.

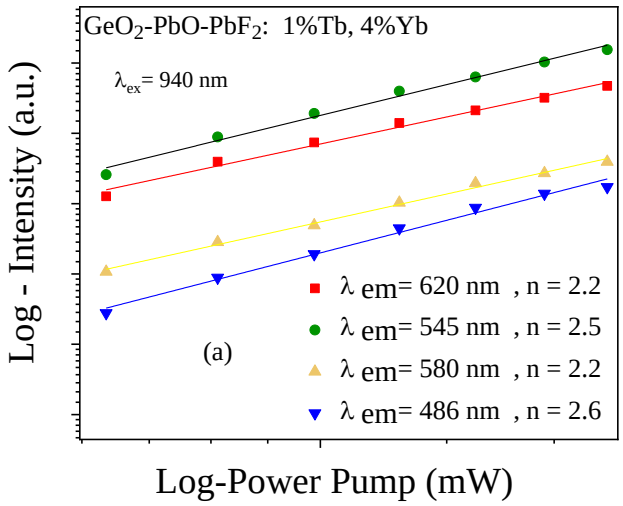


Figure IV-7: Log–log plot of emission intensities as a function of incident power Tb^{3+}–Yb^{3+} co-doped GeO_2–PbO–PbF_2 oxyfluoride glass.

This two-photon behavior is characteristic of cooperative energy-transfer up-conversion mechanisms in Tb^{3+}/Yb^{3+} co-doped systems, where two excited Yb^{3+} ions simultaneously transfer their energy to a neighboring Tb^{3+} ion, promoting it to the $^5D_4$ emitting level. Similar two-photon UC processes and comparable slope values have been widely reported in Tb^{3+}/Yb^{3+}-based glass and crystalline hosts, confirming the validity of the proposed mechanism [13, 21-22].

IV-6-3. Energy transfer mechanism $Yb^{3+} \rightarrow Tb^{3+}$

Based on the spectroscopic investigations and the pump power dependence analysis discussed in the previous section, the up-conversion (UC) luminescence observed in the Tb^{3+}/Yb^{3+} co-doped GeO_2–PbO–PbF_2 oxyfluoride glass can be attributed to an efficient cooperative energy transfer mechanism from Yb^{3+} sensitizers to Tb^{3+} activator ions, as illustrated by the schematic energy level diagram shown in Figure IV-8. Under near-infrared excitation at 940 nm, Yb^{3+} ions are resonantly excited from the $^2F_{7/2}$ ground state to the $^2F_{5/2}$ excited state, owing to their large absorption cross section in the 900–980 nm spectral region.

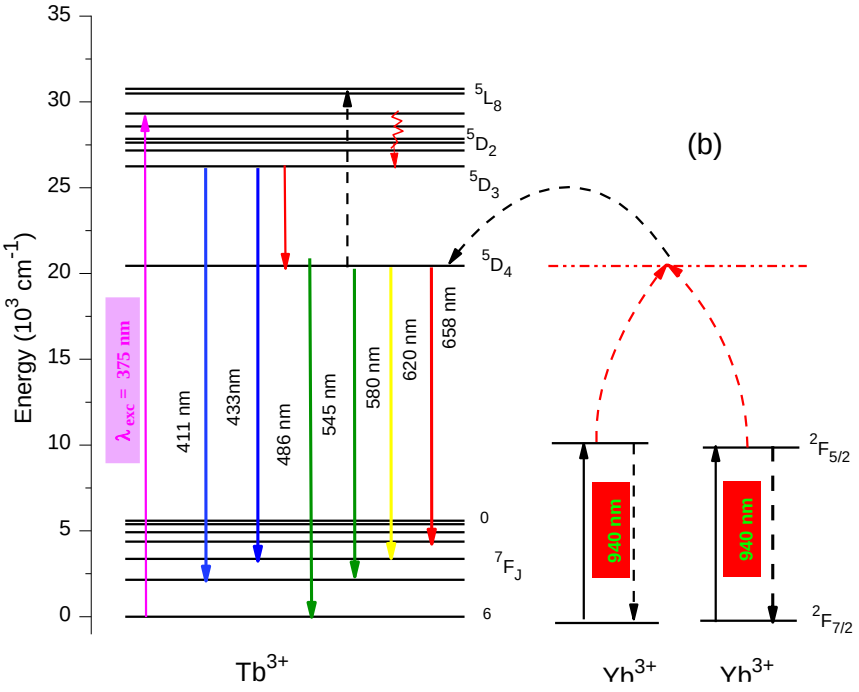


Figure IV-8: Partial energy level diagram of Tb^{3+} illustrating the $Yb^{3+} \rightarrow Tb^{3+}$ energy transfer mechanism under 940 nm excitation.

When two neighboring Yb^{3+} ions are simultaneously excited to the $^2F_{5/2}$ level, their combined excitation energy can be transferred cooperatively to a nearby Tb^{3+} ion. This cooperative sensitization promotes Tb^{3+} from its $^7F_6$ ground state directly to the $^5D_4$ emitting level, which can be described by the following process:

$$2Yb^{3+}(^2F_{5/2}) + Tb^{3+}(^7F_6) \rightarrow 2Yb^{3+}(^2F_{7/2}) + Tb^{3+}(^5D_4)$$

Once the $^5D_4$ level is populated, Tb^{3+} undergoes radiative transitions $^5D_4 \rightarrow {}^7F_J$ (J = 0–6), giving rise to the characteristic visible (blue–green–red) UC emission lines commonly reported in Tb^{3+}-based up-conversion spectra [2, 3, 23]. The proposed cooperative mechanism is strongly supported by the experimentally observed two-photon-type behavior (slope values close to $n \approx 2$) derived from the log–log analysis of the pump power dependence, confirming that two excitation quanta are involved in populating the emitting $^5D_4$ state.

This cooperative energy-transfer pathway is favored in Tb^{3+}/Yb^{3+} co-doped systems because the energy gap between the Tb^{3+} $^7F_6$ ground state and the $^5D_4$ excited level cannot be efficiently bridged by a single Yb^{3+} excitation. Consequently, a two-photon cooperative interaction between two excited Yb^{3+} ions is required to populate the emitting level of Tb^{3+}. Alternative mechanisms such as excited-state absorption (ESA) are therefore unlikely to dominate in the present glass system, in agreement with the extracted slope values and the absence of intermediate Tb^{3+} absorption levels in the near-infrared region.

Similar cooperative $Yb^{3+} \rightarrow Tb^{3+}$ energy transfer mechanisms have been extensively reported in Tb^{3+}/Yb^{3+} co-doped glassy and crystalline hosts, including germanate and oxyfluoride matrices, where efficient green up-conversion emission has been attributed to the same sensitization pathway [12-13, 15, 20]. In addition, the UC efficiency is known to depend on several factors such as dopant concentrations, the nature of the host matrix, and interionic distances, which collectively govern the energy transfer dynamics [3, 24]. Overall, the good agreement between the present results and previous studies confirms that cooperative energy transfer from Yb^{3+} ions is the dominant mechanism responsible for the observed UC luminescence in the investigated GeO_2–PbO–PbF_2 glass system.

IV-6-4. Time-resolved luminescence and decay analysis

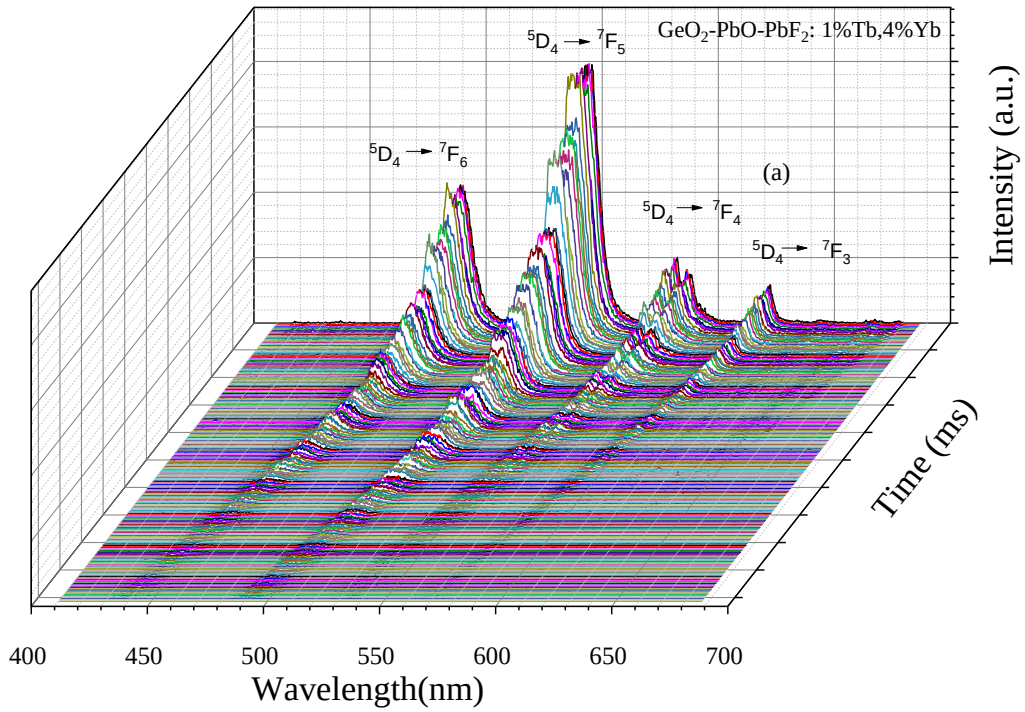
To gain deeper insight into the dynamical processes governing the up-conversion emission in the Tb^{3+}/Yb^{3+} co-doped GeO_2–PbO–PbF_2 oxyfluoride glass, time-resolved photoluminescence measurements were performed under near-infrared excitation at 976 nm. Figure IV-9a presents the three-dimensional time-resolved emission spectrum, which provides a global representation of the temporal evolution of the emission intensity as a function of wavelength. This time–wavelength–intensity map clearly shows that all visible emission bands evolve synchronously with time and originate exclusively from Tb^{3+} ions, thereby confirming that the up-conversion luminescence is associated with radiative transitions from the $^5D_4$ emitting level.

The time-resolved map further reveals that the spectral distribution of the emission remains unchanged during the decay process, indicating that no additional intermediate emitting states are involved and that the relaxation dynamics are governed by a single dominant emitting level. This behavior is consistent with the steady-state emission results and supports the assignment of the up-conversion emission to Tb^{3+} ions sensitized by Yb^{3+} under NIR excitation.

To quantitatively analyze the relaxation dynamics, decay curves were extracted at selected emission wavelengths corresponding to the main Tb^{3+} transitions, namely λ_{em} = 490 nm ($^5D_4 \rightarrow {}^7F_6$), 545 nm ($^5D_4 \rightarrow {}^7F_5$), and 621 nm ($^5D_4 \rightarrow {}^7F_3$), as shown in figure IV-9b. The decay profiles exhibit nearly single-exponential behavior, indicating that the population and depopulation of the $^5D_4$ level are dominated by a single relaxation pathway without significant contributions from competing non-radiative or back-transfer processes.

The experimentally extracted decay times are approximately $\tau_{exp} \approx 2.11$ ms at 490 nm, 2.15 ms at 545 nm, and 1.94 ms at 621 nm. The similarity of the decay times at 490 and 545 nm confirms that these emissions originate from the same $^5D_4$ excited state and experience comparable local environments within the glassy matrix. The slightly shorter lifetime observed at 621 nm may be attributed to differences in branching ratios and transition probabilities associated with the $^5D_4 \rightarrow {}^7F_3$ channel.

These lifetime values are in good agreement with those reported for Tb^{3+}/Yb^{3+} co-doped germanate and oxyfluoride glass systems, where millisecond-scale decay times of the $^5D_4$ level are typically observed under Yb^{3+}-sensitized excitation [13, 24]. The consistency of the decay behavior across different emission wavelengths further indicates the absence of significant concentration quenching or energy back-transfer effects in the investigated composition, confirming the efficiency of the $Yb^{3+} \rightarrow Tb^{3+}$ up-conversion energy transfer mechanism.



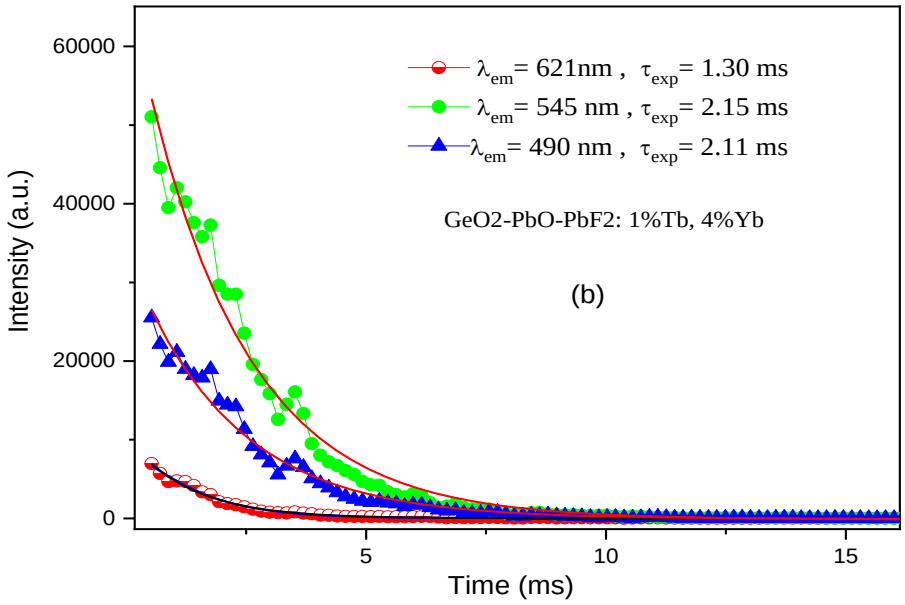


Figure IV-9: Time-resolved luminescence of Tb^{3+}–Yb^{3+} co-doped GeO_2–PbO–PbF_2 oxyfluoride glass under 976 nm excitation.(a) Three-dimensional time-resolved emission spectrum.(b) Decay curves recorded for the $^5D_4 \rightarrow {}^7F_6$ (490 nm), $^5D_4 \rightarrow {}^7F_5$ (545 nm), and $^5D_4 \rightarrow {}^7F_4$ (621 nm) transitions of Tb^{3+}

IV-7. Chromaticity analysis and multicolor emission

The chromaticity properties of the Tb^{3+}/Yb^{3+} co-doped GeO_2–PbO–PbF_2 oxyfluoride glass were investigated using the CIE 1931 colorimetric system. The chromaticity coordinates were calculated from the experimental emission spectra recorded under different excitation wavelengths, allowing a quantitative evaluation of the emission color and its dependence on the excitation mechanism.

Figure IV-10 illustrates the CIE chromaticity diagram corresponding to the emission of the investigated glass under ultraviolet and near-infrared excitation. Under UV excitation at 375 nm, the chromaticity coordinates are located in the green region of the CIE diagram, with values of (x = 0.274, y = 0.569). This emission color originates from the dominant contribution of the $^5D_4 \rightarrow {}^7F_5$ transition of Tb^{3+} ions, which is responsible for the intense green luminescence observed in the steady-state emission spectra.

When the excitation wavelength is shifted to the near-infrared region at 976 nm, the chromaticity coordinates slightly change to (x = 0.277, y = 0.550). This displacement

reflects a modification in the relative contributions of the blue ($^5D_4 \rightarrow {}^7F_6$), green ($^5D_4 \rightarrow {}^7F_5$), and red ($^5D_4 \rightarrow {}^7F_3$) emission components of Tb^{3+} ions. Such behavior can be attributed to the different excitation pathways involved under UV and NIR excitation, namely direct excitation of Tb^{3+} ions in the former case and Yb^{3+}-sensitized up-conversion processes in the latter.

Despite this excitation-dependent shift, the emission color remains predominantly green in both cases, indicating a high degree of chromatic stability of the material.

The ability to modulate the chromaticity coordinates through the choice of excitation wavelength highlights the multicolor emission potential of the Tb^{3+}/Yb^{3+} co-doped GeO_2–PbO–PbF_2 glass. This feature, combined with the efficient up-conversion luminescence demonstrated in the previous sections, makes the investigated glass system a promising candidate for photonic applications requiring excitation-dependent color control, such as display technologies, solid-state lighting, and optical signaling devices.

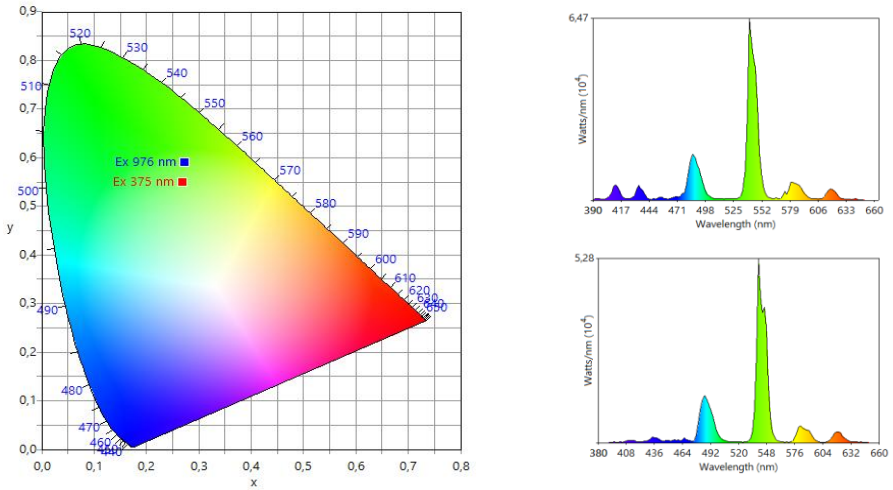


Figure IV-10: CIE chromaticity diagram of Tb^{3+}–Yb^{3+} co-doped GeO_2–PbO–PbF_2 oxyfluoride glass under 375 nm and 976 nm excitation wavelengths

IV-8. Judd–Ofelt Analysis of Er^{3+} in GeO_2–PbO–PbF_2–CdF_2 Oxyfluoride Glass

The Judd–Ofelt (J–O) analysis performed on the Er^{3+}-doped GeO_2–PbO–PbF_2–CdF_2 oxyfluoride glass reveals a clear predominance of electric dipole transitions over magnetic dipole transitions. This behavior markedly differs from that reported for

crystalline CdF_2, highlighting the strong influence of the amorphous oxyfluoride environment. Such dominance of electric dipole transitions indicates a highly asymmetric local site around Er^{3+} ions and reflects the partially covalent nature of the Er^{3+}–ligand interactions within the glass matrix.

IV-8-1. Relation ship between Radiative Transition Probabilities and Emission Cross Sections

The emission cross section $\sigma_e(\lambda)$ is directly correlated with the spontaneous radiative transition probability $A_{JJ'}$. An increase in $A_{JJ'}$ values leads to larger emission cross sections, thereby enhancing the efficiency of stimulated emission processes. In the present glass system, relatively high $A_{JJ'}$ values are observed for the transitions $^2H_{11/2} \rightarrow {}^4I_{15/2}$ and $^4F_{7/2} \rightarrow {}^4I_{15/2}$, indicating strong emission capabilities in the ultraviolet and visible spectral regions. These results underline the potential of this oxyfluoride glass for applications requiring efficient visible emission.

IV-8-2. Absorption Spectroscopic Characterization

The absorption spectra of trivalent erbium ions (Er^{3+}) doped into the GeO_2–PbO–PbF_2–CdF_2 oxyfluoride Glasses**,** were recorded at room temperature in the near-infrared (NIR), visible, and ultraviolet (UV) regions. The Er^{3+} ion has an electronic configuration of [Xe] $4f^{11}$, and the observed bands arise from intra-configurational 4f→4f transitions. The ground state of the erbium ion is the $^4I_{15/2}$ multiplet, from which all the transitions observed at room temperature originate.

IV-8-3. Absorption Spectrum in the Near-Infrared Region (700–1700 nm)

The near-infrared region is particularly important for applications in optical telecommunications and laser amplification. As shown in figure IV-11, the NIR spectrum is dominated by a strong absorption band centered around 1530 nm, attributed to the $^4I_{15/2} \rightarrow {}^4I_{13/2}$ transition. This transition corresponds to the C-band of optical fibers and represents the most widely exploited transition in erbium-doped amplifiers.
Another pronounced band appears around 980 nm and is assigned to the $^4I_{15/2} \rightarrow {}^4I_{11/2}$ transition. This transition is widely used for optical pumping of Er^{3+} ions using

commercial laser diodes. A weaker absorption band is also observed near 800 nm, corresponding to the $^4I_{15/2} \rightarrow {}^4I_{9/2}$ transition.

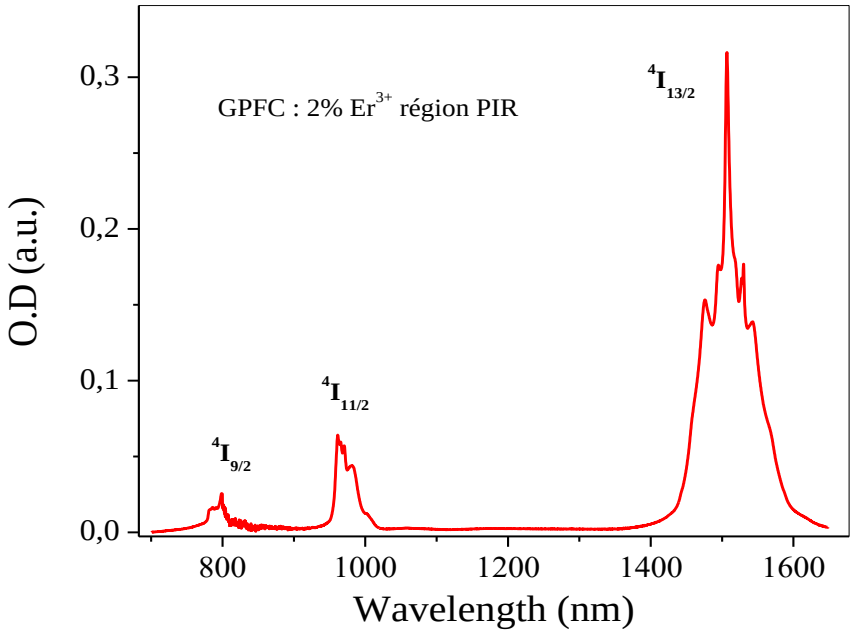


Figure IV-11: Room-Temperature IR-absorption Spectrum of GeO_2–PbO–PbF_2–CdF_2: Er^{3+} oxyfluoride Glasses

IV-8-4. Absorption Spectrum in the Visible Region (400–700 nm)

The absorption spectrum in the visible region, presented in figure IV-12, reveals several bands associated with transitions to higher-energy excited multiplets. The band located around 650 nm is attributed to the $^4I_{15/2} \rightarrow {}^4F_{9/2}$ transition, which is involved in red emission processes through upconversion. The bands observed near 540 nm and 520 nm correspond to the $^4I_{15/2} \rightarrow {}^4S_{3/2}$ and $^4I_{15/2} \rightarrow {}^2H_{11/2}$ transitions, respectively. The latter is known for its hypersensitive character to the local environment of the ion, in accordance with the intensity rules described by the Judd–Ofelt theory.

The band observed around 485 nm is attributed to the $^4I_{15/2} \rightarrow {}^4F_{7/2}$ transition, corresponding to a transition in the blue region of the visible spectrum. The bands located between 440 and 450 nm are associated with the $^4I_{15/2} \rightarrow {}^4F_{5/2}$ and $^4F_{3/2}$ transitions, which correspond to higher-energy transitions in the visible region, often referred to as the cold visible. Although these transitions are less intense than those observed in the green and red regions, they indicate access to higher excited electronic

levels and confirm the richness of the energy level structure of Er^{3+} ions [25] in the GeO_2–PbO–PbF_2–CdF_2: Er^{3+} oxyfluoride Glasses.

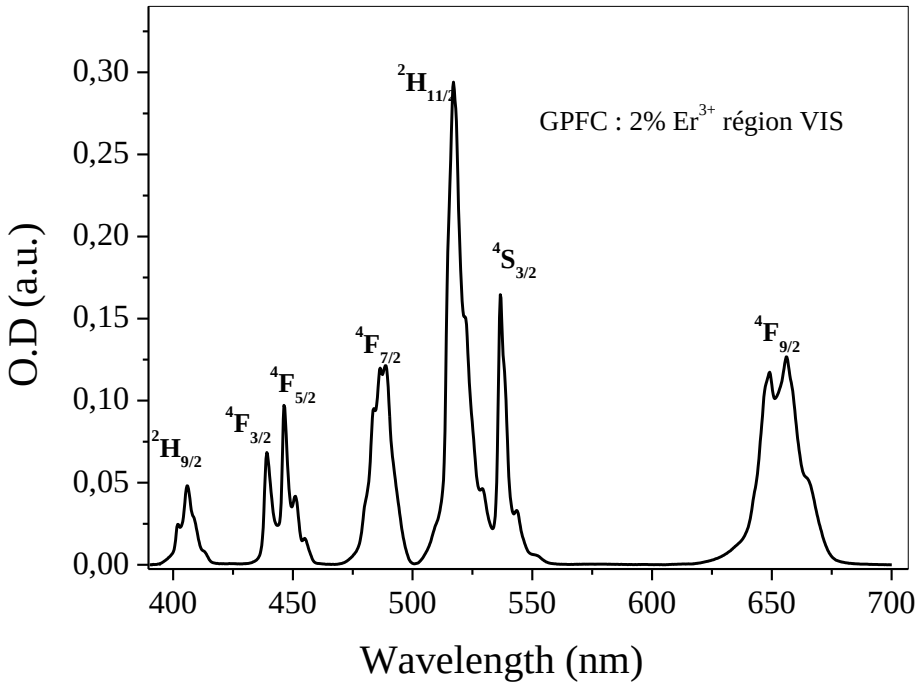


Figure IV-12: Room-Temperature UV–Visible absorption spectrum of GeO_2–PbO–PbF_2–CdF_2: Er^{3+} oxyfluoride Glasses

IV-8-5. Absorption Spectrum in the Ultraviolet Region (200–400 nm)

The absorption spectrum in the ultraviolet region, illustrated in Figure 3, is characterized by transitions to higher-energy electronic levels. A pronounced band appears around 380 nm and is attributed to the $^4I_{15/2} \rightarrow {}^4G_{11/2}$ transition. The most intense band in the UV region is observed near 255 nm, corresponding to the $^4I_{15/2} \rightarrow {}^4D_{7/2}$ transition, indicating a high absorption cross-section at higher energies [25].

IV-9. Influence of the GeO_2–PbO–PbF_2–CdF_2: Er^{3+} Matrix and Nature of the Transitions

The 4f–4f transitions of the Er^{3+} ion are, in principle, forbidden by the Laporte parity selection rule for electric dipole transitions. However, in the GeO_2–PbO–PbF_2–CdF_2: Er^{3+} oxyfluoride Glasses, these transitions become observable due to several mechanisms.

The contribution of forced electric dipole (ED) transitions results from the mixing of 4f states with opposite-parity configurations (such as $4f^{10}$, 5d), induced by the crystal field and by local perturbations related to the incorporation of Er^{3+} ions into the glass network. Furthermore, certain transitions, particularly $^4I_{15/2} \rightarrow {}^4I_{13/2}$, exhibit a significant magnetic dipole (MD) contribution, which explains their weak dependence on the local symmetry of the host matrix.

IV-10. Selection and Properties of GeO_2–PbO–PbF2–CdF2: Er^{3+} oxyfluoride Glasses

The oxyfluoride matrix GeO_2–PbO–PbF_2–CdF_2 doped with Er^{3+} ions exhibit characteristics that are particularly favorable for the incorporation of rare-earth ions and for the study of their spectroscopic properties:

➤ **Low phonon energy:** The Er–F bonds in this matrix generate lattice vibrations (phonons) with low energy. This low phonon energy significantly limits multiphonon non-radiative relaxation processes, thereby enhancing the radiative efficiency of Er^{3+} ions and contributing to the good spectral resolution of the observed absorption lines.

IV-11. Formalism of the Judd–Ofelt Theory

The Judd–Ofelt theory [26, 27], developed independently by Judd and Ofelt, is a semi-empirical approach widely used for the spectroscopic analysis of rare-earth ions. It allows the determination of radiative transition probabilities associated with intra-configurational 4f→4f transitions, as well as fundamental spectroscopic parameters such as radiative lifetimes (τ), branching ratios (β), and emission cross-sections (σ_{emis}). The application of the Judd–Ofelt theory in the present study is based on the following assumptions:

- Spectroscopic measurements are performed at room temperature.
- Only intra-configurational transitions involving the $4f^n$ shell of the investigated rare-earth ion are considered.
- The absorption spectra used for the analysis are recorded at room temperature.
- The Stark sublevels of the ground level are assumed to be equally populated.
- The excited multiplets of the rare-earth ion are considered to be completely degenerate.

IV-12. Exploitation of the Judd–Ofelt Analysis

The Judd–Ofelt (JO) [26, 27] theory is used to determine the spectroscopic properties and laser parameters of trivalent erbium ions (Er^{3+}) incorporated into the GeO_2–PbO–PbF2–CdF2: Er^{3+} oxyfluoride Glasses. From the experimental absorption spectra, this approach allows the extraction of the intensity parameters Ω_2, Ω_4, and Ω_6, which are required for the evaluation of oscillator strengths and radiative transition probabilities. The Judd–Ofelt parameters Ω_t allow the prediction of spontaneous emission band intensities and provide insight into the covalent nature of the bonding between the ions forming the glass matrix [28].

a) Mean Wavelength and absorption cross-section

Before calculating the mean wavelength $\bar{\lambda}$ associated with each absorption band, the continuous background is first subtracted in order to isolate the intrinsic contribution of the considered transition. The mean wavelength is then determined using the following expression [29].

$$\bar{\lambda} = \frac{\int \lambda.\sigma_{abs}(\lambda).d\lambda}{\int \sigma_{abs}(\lambda).d\lambda} \qquad \text{(Eq. IV-7)}$$

Where $\sigma_{abs}(\lambda)$ represents the spectral absorption cross-section.

The absorption cross-section $\sigma_{abs}(\lambda)$ calculated from an absorption spectrum obtained at room temperature using the formula:

$$\sigma_{abc}(\lambda) = \frac{\ln 10.D.O(\lambda)}{L.N} \qquad \text{(Eq. IV-8)}$$

Where L is the sample thickness, $DO(\lambda)$ and N are the optical density and the concentration of dopant ions ($9.6x10^{20}$ ions/cm^3).

The numerical processing was performed using Origin software, allowing the determination, for each transition originating from the $^4I_{15/2}$ ground level of the Er^{3+} ion, of the mean wavelength $\bar{\lambda}$ as well as the measured absorption cross-section σ_{mes}. The results obtained for Er^{3+}-doped GeO_2–PbO–PbF_2 glass, summarized in Table IV-1, show that the absorption spectrum exhibits intense bands associated with the $^4I_{13/2}$ multiplet at 1527.6 nm, with an integrated intensity of 14.13×10^{-20} cm^2·nm and a peak cross section of 42.22×10^{-20} cm^2. These features are well suited for amplification in the 1.5 μm region, as well as for pumping at 980 nm or 1480 nm. Additionally, a

prominent band corresponding to the $^{2}H_{11}/_{2}$ level is observed at 519.4 nm, with an integrated intensity of 4.76 × 10^{-20} cm²·nm and a peak cross section of 14.22 × 10^{-20} cm², enabling efficient green up-conversion processes. Moderately intense bands include $^{4}F_{9}/_{2}$ at 653.7 nm (2.88 × 10^{-20} cm²·nm, peak ~8–9 × 10^{-20} cm²) and $^{4}S_{3}/_{2}$ at 538.9 nm (1.47 × 10^{-20} cm²·nm, similar peak cross-section), useful for red and green excitation, as well as the $^{4}I_{11}/_{2}$ band at 976 nm (1.25 × 10^{-20} cm²·nm, 3.73 × 10^{-20} cm²), which is adequate for standard 980 nm pumping of Er^{3+} amplifiers. Weak absorption is observed for $^{4}I_{9}/_{2}$ (810.6 nm), $^{4}F_{7}/_{2}$ (486.7 nm), the combined $^{4}F_{3}/_{2}$+$^{4}F_{5}/_{2}$ (445.3 nm), and especially $^{2}H_{9}/_{2}$ (406.8 nm) with integrated intensities ≤1.35 × 10^{-20} cm²·nm and peak cross-sections ≤4.04 × 10^{-20} cm², reflecting the small line strengths typical for high-lying Er^{3+} transitions

Table IV-1: Integrated Absorption Cross-Sections σ_{int} and Mean Wavelengths $\bar{\lambda}$ of the Different Transitions of Er^{3+} Ions in GeO_2–PbO–PbF_2–CdF_2 oxyfluoride Glasses

Multiplet	$\bar{\lambda}$ (nm)	$\int_{j}^{j'} Do.d\lambda$	$\sigma_{mes}(\lambda)$ $(10^{-20}cm^2.nm)$
$^{2}I_{13/2}$	1527.58	14.13	42.22
$^{2}I_{11/2}$	975.96	1.25	3.73
$^{2}I_{9/2}$	810.59	0.85	2.54
$^{4}F_{9/2}$	653.67	2.88	8.60
$^{4}S_{3/2}$	538.94	1.47	4.40
$^{2}H_{11/2}$	519.4	4.76	14.22
$^{4}F_{7/2}$	486.74	1.35	4.04
$^{4}F_{3/2}$ +$^{4}F_{5/2}$	445.3	0.8	2.4
$^{2}H_{9/2}$	406.78	0.36	1.7

b) Transition Strengths

The optical transitions observed between the energy levels of trivalent erbium ions (Er^{3+}) may be of electric dipole, magnetic dipole, or, more rarely, electric quadrupole nature. Within the framework of the Judd–Ofelt theory, the analysis of the intensities of 4f→4f transitions mainly relies on the contributions of forced electric dipole and magnetic dipole transitions.

c) Calculated Forced Electric Dipole Transition Strengths

Transitions between energy levels follow selection rules that depend on the nature of the involved dipoles. In the present case, the forced electric dipole transitions obey the following selection rule:

$\Delta J \leq 2l$ that is $J \leq 6$ here (l=3) J=0 ↔J odd transitions are forbidden.

The formula used to determine the transition strength values is given by:

$$S_{JJ'}^{DE\ cal} = \sum_{t=2,4,6} \Omega_t \left| < 4F^N \alpha[S,L]J \right| \left| U^{(t)} \right| \left| 4F^N \alpha'[S',L']J' > \right|^2 \qquad \text{(Eq. IV-9)}$$

Where Ω_t (t = 2, 4, 6) represent the Judd–Ofelt (JO) intensity parameters, and

$\left| < 4F^N \alpha[S,L]J \right| \left| U^{(t)} \right| \left| 4F^N \alpha'[S',L']J' > \right|^2$ They represent the reduced matrix elements of the unit irreducible tensor operator of rank (t = 2, 4, 6). The values of these matrix elements depend on the rare-earth ion and on the transition under consideration.

d) Calculated Magnetic Dipole Transition Strengths

Magnetic dipole transitions are allowed only under specific conditions. It can be noted that the selection rules for ions incorporated into host matrices remain essentially the same as those for free ions (see table IV -1): $\Delta J \leq 1$ with $\Delta J = 0, \pm 1$ However, transitions between J = 0 ↔ 0 are forbidden. The magnetic dipole transition strength is then given by the following expression:

$$(S_{JJ'}^{dm})^{cal} = \left(\frac{h}{4\pi mc}\right)^2 \sum_{MM'} \left| < JM \left| \vec{L} + 2\vec{S} \right| JM' > \right|^2 \qquad \text{(Eq. IV-10)}$$

Where h is Planck's constant, and m and c are respectively the electron mass and the speed of light in vacuum. The term $\left| < JM \left| \vec{L} + 2\vec{S} \right| JM' > \right|^2$ represents the matrix elements of the operator $(\vec{L} + 2\vec{S})$, whose values are given in tableau IV-2.

Table IV-2: Squared Reduced Matrix Elements of $U^{(t)}$ (t =2,4, 6) Obtained Between the Ground Level $^4I_{15/2}$ and the Excited Levels $^{2S'+1}L'_{J'}$ [30].

$^{2S+1}L_J$	$^{2S'+1}L'_{J'}$	$\lvert\langle\lVert U^{(2)}\rVert\rangle\rvert^2$	$\lvert\langle\lVert U^{(2)}\rVert\rangle\rvert^2$	$\lvert\langle\lVert U^{(2)}\rVert\rangle\rvert^2$	$\lvert\langle\lVert \vec{L} + 2\vec{S}\rVert\rangle\rvert^2$

$^4I_{15/2}$	$^4I_{13/2}$	0.01956	0.11734	1.43164	18.91644
	$^4I_{11/2}$	0.02536	0.00012	0.39961	0
	$^4I_{9/2}$	0	0.15664	0.00662	0
	$^4F_{9/2}$	0	0.55336	0.46835	0
	$^4S_{3/2}$	0	0	0.22780	0
	$^2H_{11/2}$	0.71182	0.40974	0.0868	0
	$^4F_{7/2}$	0	0.14729	0.628778	0
	$^4F_{5/2} + {}^4F_{3/2}$	0	0	0.34553	0
	$^2H_{9/2}$	0	0.01869	0.22025	0

e) Measured Electric and Magnetic Dipole Transition Strengths

These transition strengths are referred to as measured because they are determined using the integrated absorption cross-sections obtained from calibrated absorption spectra.

The measured electric dipole transition strengths are obtained by applying the following expression [29]:

$$S_{JJ'}^{mes} = \left(\frac{9n}{(n^2+2)^2}\right)\left(\frac{3hc\varepsilon_0}{2\pi^2 e^2}\right)\frac{1}{\bar{\lambda}}(2J+1)\int \sigma_{asb}(\lambda)d\lambda \qquad \text{(Eq. IV-11)}$$

Using the previous formula, the measured electric dipole transition strengths can be obtained through the following expression [29]:

$$S_{JJ'}^{DEmes} = S_{JJ'}^{mes} - \left(\frac{9n^2}{(n^2+2)^2}\right)S_{JJ'}^{DM} \qquad \text{(Eq. IV-12)}$$

where n is the refractive index of the host material, and e is the elementary charge of the electron.

Table 3 summarizes the measured and calculated electric dipole transition strengths for the five transitions from the $^4I_{15/2}$ ground level to the excited levels of Er^{3+} ions. A least-squares fitting procedure was used to adjust the measured electric dipole transition strengths to the calculated ones in order to extract the Judd–Ofelt parameters, using the Mathcad calculation software.

Table IV-3: Measured and Calculated Electric Dipole Transition Strengths

Transition $^4I_{15/2} \rightarrow$	λ (nm)	E (cm^{-1})	S_{cal} (10^{-20} cm^2)	S_{mes} (10^{-20} cm^2)
$^4I_{13/2}$	1527.56	6620.06	2.063	2.143
$^4I_{11/2}$	975.96	10246.29	0.593	0.358
$^4I_{9/2}$	810.59	12336.73	0.188	0.295
$^4F_{9/2}$	653.67	15298.30	1.227	1.235
$^4S_{3/2}$	538.94	18554.78	0.292	0.755
$^4H_{11/2}$	519.40	19253.04	2.548	2.554
$^4F_{7/2}$	486.74	20544.65	0.989	0.775
$^4F_{5/2}$ +$^4F_{3/2}$	445.30	22456.96	0.453	0.502
$^4F_{9/2}$	406.78	24583.29	0.305	0.251
Ω_t (10^{+20} cm^2)			Ω_2= 2.76, Ω_4 = 1.14, Ω_6 = 1.31	

The experimental line strengths (*Smes*) and the calculated ones (Scal) show good agreement for most transitions, confirming the reliability of these parameters.

After determining the measured and calculated electric dipole transition strengths for each absorption band (Table 3), the Judd–Ofelt intensity parameters Ω_2, Ω_4, and Ω_6 were obtained by a least-squares fit minimizing the deviation between experimental and calculated line strengths. The best-fit values are $\Omega_2 = 2.76 \times 10^{-20}$ cm², $\Omega_4 = 1.14 \times 10^{-20}$ cm², and $\Omega_6 = 1.31 \times 10^{-20}$ cm². The quality of the fit was evaluated using the root-mean-square (RMS) deviation defined by Eq. (IV-13);

$$\delta = \sqrt{\sum_{i=1}^{q} \frac{((S_{JJ'}^{DEcal})_i - ((S_{JJ'}^{DEmes})_i)^2}{q-p}} \qquad \text{(Eq. IV-13)}$$

the obtained RMS value $\delta = 0.239 \times 10^{-20}$ cm² indicates a good agreement between calculated and experimental strengths. The Ω_2 parameter is particularly sensitive to the local environment of rare-earth ions, reflecting the asymmetry of the coordination structure, the polarizability of the surrounding ligands, and the nature of the chemical bonds. Compared with Er^{3+} in crystalline CdF_2, where Ω_2 is extremely low [31, 32], the much larger Ω_2 in the present glass reveals a highly asymmetric and partially covalent local environment arising from the mixed O^{2-}/F^- coordination. The Ω_4 and Ω_6 values are moderate, consistent with the polarizability of the lead-based glass network, and

they favor enhanced radiative transitions, particularly in the near-infrared region. The spectroscopic quality factor $\chi = \Omega_4/\Omega_6 = 0.87$ confirms that this oxyfluoride glass maintains good laser potential while exhibiting the typical structural disorder of glassy materials.

Matrice	Ω_2 (10^{-20} cm²)	Ω_4 (10^{-20} cm²)	Ω_6 (10^{-20} cm²)	$\chi = \Omega_4/\Omega_6$	Ref
GPFC: Er^{3+}	2.76	1.14	1.31	0.87	This work
Cristal CdF_2	1.284	0.413	1.272	0.32	[33]
Verre silice	4.23	1.04	0.61	1.70	[34]
Verre ZBLAN	2.20	1.40	0.91	1.54	[35]

f) Spontaneous Transition Probability

Once the Ω_t parameters are determined and the reduced matrix elements of the tensor operator are available, the probabilities of electric and magnetic dipole transitions for spontaneous emission can be evaluated using the following expressions [29]:

$$A_{JJ'}^{Tot} = A_{JJ'}^{DE} + A_{JJ'}^{DM} = \frac{16\pi^3 e^2}{3h(2J+1)\varepsilon_0 \overline{\lambda^3}} \left(\frac{n(n^2+1)^2}{9} S_{JJ'}^{DE} + n^3 S_{JJ'}^{DM}\right) \quad \text{(Eq. IV-14)}$$

$$\tau_{R,J} = \frac{1}{\sum_{J'} A_{JJ'}} = \frac{1}{\sum_{J'} A_{JJ'}^{DE} + A_{JJ'}^{DM}} \quad \text{(Eq. IV-15)}$$

$$\beta_{JJ'=\tau_R \cdot A_{JJ'}} \quad \text{(Eq. IV-16)}$$

g) Radiative Lifetime of an Emitting Level and Branching Ratio

The calculation of JO parameters also allows the determination of others parameters fundamental and importance in laser spectroscopy.

The tabulated results present the calculated radiative properties for Er^{3+} ions embedded in the oxyfluoride glass matrix, derived from Judd–Ofelt (JO) analysis. The parameters include transition wavelength (λ), energy gap (ΔE), electric dipole ($A_{JJ'}^{ed}$) and magnetic dipole ($A_{JJ'}^{md}$) transition probabilities, branching ratios ($\beta_{JJ'}$), and radiative lifetimes (τ_{rad}).

The obtained results for all excited levels are summarized in table IV-4.

Table IV-4: Radiative parameters for Er^{3+} ions in GPFC glass: Mean wavelengths (λ), electric (A_{ed}) and magnetic (A_{md}) dipole transition probabilities, branching ratios (β), and radiative lifetimes (τ_{rad})

Transitions and spontaneous emmission	*λ (nm)*	*ΔE (cm^{-1})*	$A_{JJ'}^{ed}$ *(s^{-1})*	$A_{JJ'}^{md}$ *(s^{-1})*	$\beta_{JJ'}$ *(%)*	τ_{rad} *(ms)*
$^4I_{13/2}$ → $^4I_{15/2}$	1527.58	6611.24	191.53	40.64	*1.000*	*4.310*
0	0.00		0.00	0.00	*0.000*	*0.000*
$^4I_{11/2}$ → $^4I_{13/2}$	2739.00	3650.97	30.93	15.85	*0.162*	*3.450*
$^4I_{15/2}$	975.96	10246.29	243.1	0.00	*0.838*	
$^4I_{9/2}$ → $^4I_{11/2}$	- 4452.00	2246.18	1.34	3.70	*0.019*	*00* *3.765*
$^4I_{13/2}$	1696.00	5896.23	86.72	0.00	*0.326*	
$^4I_{15/2}$	810.59	12336.73	173.80	0.00	*0.655*	
$^4F_{9/2}$ → $^4I_{9/2}$	3543.00	2822.47	3.87	6.33	*0.005*	*0.460*
$^4I_{11/2}$	1947.00	5136.11	108.89	8.52	*0.054*	
$^4I_{13/2}$	1147.00	8718.40	90.36	0.00	*0.042*	
$^4I_{15/2}$	653.67	15298.30	1956.96	0.00	*0.900*	
$^4S_{3/2}$ → $^4F_{9/2}$	3176.00	3148.61	1.64	0.00	*0.001*	*0.334*
$^4I_{9/2}$	1675.00	5970.15	99.27	0.00	*0.056*	
$^4I_{11/2}$	1217.00	8216.93	66.80	0.00	*0.028*	
$^4I_{13/2}$	843.00	11862.40	828.25	0.00	*0.286*	
$^4I_{15/2}$	538.94	18554.78	2001.83	0.00	*0.629*	
$^2H_{11/2}$ → $^4S_{3/2}$	13262.60	754.00	0.038	0.00	*0.000*	*0.140*
$^4F_{9/2}$	2562.00	3903.20	23.06	0.25	*0.003*	
$^4I_{9/2}$	1487.00	6724.95	113.55	0.68	*0.016*	
$^4I_{11/2}$	1115.00	8968.61	81.64	6.22	*0.012*	
$^4I_{13/2}$	792.00	12626.26	150.48	34.28	*0.026*	
$^4I_{15/2}$	519.40	19253.04	6706.80	0.00	*0.943*	
$^4F_{7/2}$ → $^2H_{11/2}$	7521.00	1329.61	1.16	0.00	*0.000*	*0.170*
$^4S_{3/2}$	4800.00	2083.33	0.03	0.00	*0.000*	
$^4F_{9/2}$	1911.00	5232.86	7.29	15.07	*0.004*	
$^4I_{9/2}$	1242.00	8051.53	208.26	10.02	*0.037*	
$^4I_{11/2}$	971.00	10298.66	313.45	0.00	*0.053*	
$^4I_{13/2}$	717.00	13947.00	584.67	0.00	*0.099*	
$^4I_{15/2}$	486.74	20544.65	4752.09	0.00	*0.81*	

These spectroscopic parameters provide a comprehensive understanding of the luminescence efficiency and radiative decay dynamics of each excited state of Er^{3+} in the GeO_2–PbO–PbF_2 glass matrix.

- **The $^4I_{13}/_2 \rightarrow {}^4I_{15}/_2$ Transition (1.5 µm Band)**

This transition is of paramount importance for telecommunication applications in the C-band region. The results indicate a branching ratio (β) equal to unity, confirming that the $^4I_{13}/_2$ metastable level relaxes exclusively toward the ground state ($^4I_{15}/_2$) through a single radiative channel. Such behavior is highly favorable for achieving population inversion in optical amplifiers.

The radiative lifetime ($\tau_{rad} \approx 4.31$ ms) is relatively long, which is characteristic of this level due to the moderate energy gap with the ground state that limits multiphonon relaxation. The total transition probability ($A \approx 232\ s^{-1}$) arises from both electric dipole and magnetic dipole contributions, with the electric dipole component being dominant. This reflects the hypersensitive nature of the transition and confirms the strong influence of the local environment on the Er^{3+} ions.

- **The $^4I_{11}/_2 \rightarrow {}^4I_{15}/_2$ and $^4I_{13}/_2$ Transitions**

The $^4I_{11}/_2$ level exhibits two competing radiative decay channels:

- The $^4I_{11}/_2 \rightarrow {}^4I_{13}/_2$ transition (~2.7 μm) has a relatively low transition probability and a modest branching ratio (~16%).
- The $^4I_{11}/_2 \rightarrow {}^4I_{15}/_2$ transition (~976 nm) dominates, with a branching ratio of ~84% and a significantly higher transition probability.

This dominance indicates that the $^4I_{11}/_2$ level is particularly efficient for near-infrared emission around 980 nm. The radiative lifetime ($\tau_{rad} \approx 3.45$ ms) remains relatively long; however, in practical systems, it is often reduced due to non-radiative multiphonon relaxation toward the $^4I_{13}/_2$ level.

- **Higher Excited Levels ($^4I_9/_2$, $^4F_9/_2$, $^4S_3/_2$, $^2H_{11}/_2$, $^4F_7/_2$)**

For higher-lying excited states, a clear trend emerges: radiative lifetimes decrease significantly, while branching ratios become strongly concentrated toward transitions terminating at the ground state.

- **$^4I_9/_2$ level:** Exhibits multiple decay channels, with the dominant transition toward $^4I_{15}/_2$ ($\beta \approx 0.65$), followed by $^4I_{13}/_2$. This indicates efficient cascading relaxation.

- **$^4F_{9/2}$ level (red emission):** Characterized by a high total transition probability and a short lifetime (~0.46 ms), with a dominant branching ratio (~90%) toward $^4I_{15/2}$. This confirms its suitability for strong red emission.
- **$^4S_{3/2}$ level (green emission):** Shows a dominant transition to the ground state ($\beta \approx 0.67$), along with a notable branch toward $^4I_{13/2}$ (~28%). This secondary channel may contribute to feeding infrared emission.
- **$^2H_{11/2}$ level (green emission):** Displays the highest transition probability among all levels, leading to a very short lifetime (~0.14 ms) and a dominant branching ratio (~94%) toward $^4I_{15/2}$. This makes it a key contributor to intense green upconversion luminescence.
- **$^4F_{7/2}$ level:** Exhibits multiple decay pathways, with a dominant transition toward $^4I_{15/2}$ (~81%). This level primarily acts as a feeding state for lower excited levels through cascade relaxation processes.

➢ **Correlation with Judd–Ofelt Parameters**

The observed radiative behavior is consistent with the Judd–Ofelt intensity parameters:

- A relatively high Ω_2 parameter enhances hypersensitive electric dipole transitions, particularly those terminating at the ground state, such as $^4I_{13/2} \rightarrow {}^4I_{15/2}$ and $^2H_{11/2} \rightarrow {}^4I_{15/2}$. This indicates that Er^{3+} ions occupy asymmetric and covalent local environments within the glass matrix.
- The balanced contributions of Ω_4 and Ω_6 are reflected in the consistent transition probabilities and branching ratios of higher excited states. This balance supports efficient radiative emission while limiting non-radiative losses.

➢ **Implications for Photonic Applications**

- **Optical amplifiers (1.5 µm):** The $^4I_{13/2}$ level exhibits ideal characteristics, including a long lifetime, a unity branching ratio, and efficient radiative decay, making it highly suitable for C-band amplification.
- **Upconversion devices:** The short lifetimes and high branching ratios of the $^2H_{11/2}$ and $^4F_{9/2}$ levels enable strong and efficient green and red emissions, respectively.

- **Mid-infrared emission:** Although the $^4I_{11}/_2 \rightarrow {}^4I_{13}/_2$ transition has a lower branching ratio, it remains a viable channel for mid-IR applications under appropriate population management conditions.

Overall, the agreement between transition probabilities, branching ratios, and Judd–Ofelt parameters demonstrates that the GeO_2–PbO–PbF_2 oxyfluoride glass provides an optimized local environment for Er^{3+} ions. The combination of high asymmetry and favorable radiative dynamics enables efficient luminescence spanning from the visible to the infrared, making this material highly promising for advanced photonic applications.

Bibliographic References

[1] LnF_3 system, *J. Alloys Compd.*, 382 (2004) 292–299. https://doi.org/10.1016/j.jallcom.2004.06.002

[2] B. Klimesz, G. Dominiak-Dzik, M. Żelechower & W. Ryba-Romanowski, Optical study of GeO_2–PbO–PbF_2 oxyfluoride glass single doped with lanthanide ions, *Opt. Mater.*, 30 (2008) 1587–1594. https://doi.org/10.1016/j.optmat.2007.09.011

[3] H. Boubekri, M. Diaf, K. Labbaci, L. Guerbous, T. Duvaut & J. P. Jouart, Synthesis and optical properties of Tb^{3+} doped CdF_2 single crystals, *J. Alloys Compd.*, 575 (2013) 339–343. https://doi.org/10.1016/j.jallcom.2013.05.189

[4] E. V. Vilejshikova, P. A. Loiko, G. E. Rachkovskaya, G. B. Zakharevich & K. V. Yumashev, Spectral and luminescent properties of oxyfluoride glasses codoped with (Yb^{3+}, Eu^{3+}) and (Yb^{3+}, Tb^{3+}), *J. Appl. Spectrosc.*, 83 (2016) 548–554. https://doi.org/10.1007/s10812-016-0326-x

[5] T. Grzyb, R. J. Wiglusz, A. Gruszeczka & S. Lis, Down- and up-converting dual-mode YPO_4:Yb^{3+},Tb^{3+} nanocrystals: synthesis and spectroscopic properties, *Dalton Trans.*, 43 (2014) 17255. https://doi.org/10.1039/c4dt02234c

[6] H. Boubekri, R. Fartas, M. Diaf, S. Rahmouni, N. Louati, S. Boulekrouche, S. Alleg & A. Bitam, Optical properties investigation and multicolor behavior of Nd^{3+}-doped SiO_2–PbO–PbF_2 oxyfluoride glasses, *Luminescence*, 39 (2024) e4832. https://doi.org/10.1002/bio.4832

[7] E. A. Davis & N. F. Mott, Conduction in non-crystalline systems V, *Philos. Mag.*, 22 (1970) 903. https://doi.org/10.1080/14786437008221061

[8] H. Mamine, H. Bendjeffal, T. Metidji, A. Djebli, N. Rebbani & Y. Bouhedja, Structural, optical and electrical properties of Ni(II)-2,2-bipyridine complexes thin films, *J. Sci. Adv. Mater. Dev.*, 4 (2019) 459. https://doi.org/10.1016/j.jsamd.2019.07.002

[9] M. S. Gadalla, R. Abd El-Sadek & R. Hamood, Synthesis, structural and optical characterization of CdS and ZnS quantum dots, *Chalcogenide Lett.*, 15(5) (2018) 281–291.

[10] W.-L. Liu, W.-J. Chen, S.-H. Hsieh & J.-H. Yu, Growth behavior of nanocrystalline ZnS thin films for solar cells, *Procedia Eng.*, 36 (2012) 46–53. https://doi.org/10.1016/j.proeng.2012.03.009

[11] L. Oulmaati, S. E. Amrani, K. Bouziane, A. Bouajaj, M. R. Britel, F. Enrichi & M.

Ferrari, Improving solar cell performance with Tb^{3+}–Yb^{3+} codoped glasses, *Appl. Sci.*, 13 (2023) 9390. https://doi.org/10.3390/app13169390

[12] J. L. Adam, N. Duhamel-Henry & J. Y. Allain, Blue and green upconversion in (Yb^{3+}, Tb^{3+}) codoped glasses, *J. Non-Cryst. Solids*, 213–214 (1997) 245–250. https://doi.org/10.1016/S0022-3093(96)00667-9

[13] A. Cheddadi, H. Boubekri, K. Labbaci, M. Diaf, L. Guerbous, T. Duvaut & J. P. Jouart, Luminescence of Tb^{3+}–Yb^{3+} codoped CdF_2 crystals, *Phys. B*, 436 (2014) 22. https://doi.org/10.1016/j.physb.2013.12.001

[14] H. Boubekri, M. Diaf, T. Pauporté, B. Viana & J. P. Jouart, Upconversion emission in Tb^{3+}/Yb^{3+} codoped CdF_2 crystals, *Proc. SPIE*, 10528 (2018) 105281Y. https://doi.org/10.1117/12.2294940

[15] F. Auzel, Upconversion and anti-Stokes processes with f and d ions in solids, *Chem. Rev.*, 104 (2004) 139–174. https://doi.org/10.1021/cr020357g

[16] F. Wang & X. Liu, Chemistry of lanthanide-doped upconversion nanocrystals, *Chem. Soc. Rev.*, 38 (2009) 976–989. https://doi.org/10.1039/b809132n

[17] M. Kochanowicz *et al.*, Upconversion luminescence of Tb^{3+} in germanate glasses, *Opt. Mater. Express*, 4 (2014) 1050–1056. https://doi.org/10.1364/OME.4.001050

[18] Z. Smara *et al.*, Energy transfer and luminescent properties of doped $NaYF_4$ nanophosphors, *Opt. Mater.*, 104 (2020) 109932. https://doi.org/10.1016/j.optmat.2020.109932

[19] H. Huang *et al.*, Luminescence and energy transfer of Yb^{3+}/Tb^{3+} codoped $LaNbO_2$, *J. Alloys Compd.*, 702 (2017) 209–215. https://doi.org/10.1016/j.jallcom.2017.01.246

[20] R. Martin-Rodriguez *et al.*, Upconversion luminescence in doped nanocrystals, *J. Phys. Chem. C*, 113 (2009) 12195. https://doi.org/10.1021/jp901711g

[21] A. Braud *et al.*, Properties of laser emissions in Tm-doped fluoride crystals, *OSA Proc.*, 26 (1999). https://doi.org/10.1364/ASSL.1999.MB9

[22] G. H. Dieke & H. M. Crosswhite, Spectra of rare-earth ions, *Appl. Opt.*, 2(7) (1963) 675.

[23] B. R. Judd, Optical absorption intensities of rare-earth ions, *Phys. Rev.*, 127 (1962) 750.

[24] G. S. Ofelt, Intensities of crystal spectra of rare-earth ions, *J. Chem. Phys.*, 37 (1962) 511.

[25] R. Reisfeld & C. K. Jørgensen, in *Handbook on the Physics and Chemistry of Rare*

Earths, North-Holland (1987).

[26] R. Fartas, M. Diaf, H. Boubekri, L. Guerbous & J. P. Jouart, *J. Alloys Compd.* (incomplete).

[27] W. T. Carnall, P. R. Fields & K. Rajnak, Energy levels of trivalent lanthanides, U.S. Dept. of Commerce (1968).

[28] H. Ebendorff-Heidepriem & P. Goldner, Tb^{3+} f–d absorption and Ω_2 parameter, *J. Non-Cryst. Solids*, 248 (1999) 247–254. https://doi.org/10.1016/S0022-3093(99)00095-1

[29] M. P. Hehlen, M. G. Brik & K. W. Krämer, 50th anniversary of the Judd–Ofelt theory, *J. Lumin.*, 136 (2013) 221–239. https://doi.org/10.1016/j.jlumin.2012.10.035

[30] S. Djellab, M. Diaf, K. Labbaci & L. Guerbous, Spectroscopic properties of Er^{3+} in CdF_2 crystals, *Phys. Scr.*, 89 (2014) 045101. https://doi.org/10.1088/0031-8949/89/04/045101

[31] M. P. Hehlen, M. G. Jani, R. C. Powell & S. A. Payne, Spectroscopic properties of Er^{3+} in SiO_2 glass, *Phys. Rev. B*, 54 (1996) 3073. https://doi.org/10.1103/PhysRevB.54.3073

[32] X. Zou & T. Izumitani, Spectroscopic properties and upconversion mechanisms of Er^{3+}-doped glasses, *J. Non-Cryst. Solids*, 162 (1993) 68–80. https://doi.org/10.1016/0022-3093(93)90742-G

General Conclusion

General Conclusion

This thesis was devoted to the synthesis and in-depth investigation of the structural and spectroscopic properties of two lead germanate-based oxyfluoride glass systems: the ternary GPF matrix (GeO_2–PbO–PbF_2) co-doped with Tb^{3+}/Yb^{3+} and the quaternary GPFC matrix (GeO_2–PbO–PbF_2–CdF_2) doped with Er^{3+}. The primary objective was to evaluate their potential for advanced photonic applications, such as frequency conversion and optical amplification.

The first phase of this work consisted of a comprehensive literature review, recalling the fundamental concepts of the glassy state and the spectroscopic properties of rare-earth ions. Particular emphasis was placed on oxyfluoride glasses, which emerge as host matrices of choice by combining the thermal stability of oxides with the low phonon energy of fluorides—a *sine qua non* condition for minimizing non-radiative relaxations.

On the experimental level, both glass systems were successfully synthesized using the conventional melt-quenching technique, followed by thermal annealing. X-ray diffraction (XRD) systematically confirmed the purely amorphous nature of the samples, proving that the incorporation of lanthanide ions (Tb^{3+}, Yb^{3+}, and Er^{3+}) does not disrupt the matrix stability nor induce phase separation.

The study of the Tb^{3+}/Yb^{3+} co-doped GPF system highlighted the crucial role of the Yb^{3+} ion as a sensitizer, exhibiting intense absorption at 976 nm. Photoluminescence measurements revealed an efficient up-conversion mechanism. Power dependence analysis yielded a slope near two, confirming a two-photon process governed by cooperative energy transfer (CET) between two excited Yb^{3+} ions and one Tb^{3+} ion. The millisecond-scale lifetimes of the $^5D_4$ level evidence high radiative efficiency and excellent optical quality of the medium.

A major contribution of the final part of this work lies in the rigorous analysis of the Er^{3+}-doped GPFC system via the Judd-Ofelt formalism. The results obtained are particularly compelling:

- The intensity parameter $\Omega_2 = 2{,}76 \times 10^{-20}$ cm² reflects a pronounced local asymmetry around the Er^{3+} ion and a covalent character of the Er-O/F bonds.
- The spectroscopic quality factor ($\chi = 0.87$) and the radiative lifetime ($\tau = 4.31$ ms) for the $^4I_{13/2}$ level position this material as a prime candidate for C-band optical amplification (telecommunications).

In conclusion, the results of this thesis demonstrate that **GPF** and **GPFC** oxyfluoride glasses constitute promising technological platforms for photonics. They offer a viable solution for developing new light sources and spectral conversion devices.

Future Perspectives

A promising extension of this work would be to explore the potential of the Er3+-doped GPFC system for non-invasive optical thermometry. By exploiting transitions from the thermally coupled energy levels (TCEL) of the Erbium ion, high-precision temperature sensors can be designed. Specifically, we envision:

- Targeted NIR excitations: Excitation around 980 nm ($^4I_{15/2} \rightarrow {}^4I_{11/2}$) for efficient pumping to higher levels, or around 1500 nm (corresponding to the resonant $^4I_{15/2} \rightarrow {}^4I_{13/2}$ transition) to study the thermal response of the material.
- Fluorescence Intensity Ratio (FIR) measurements: This protocol allows for measurements independent of excitation source power fluctuations, thereby providing a self-referenced temperature sensing capability.
- Optimization of thermal sensitivity: The ultimate goal would be to leverage the low phonon energy of the GPFC matrix to maximize luminescence yield, achieving highly precise spatial and thermal resolution. This would make this glass an ideal candidate for temperature sensors operating in harsh environments or at the micrometric scale.